MXene Materials for CO_2 Capture and Transformation

Anabel Jurado Mañas

Memòria presentada per

Anabel Jurado Mañas

Per a optar al grau de Doctor per la

Universitat de Barcelona

Programa de Doctorat en Química Teòrica i Computacional

MXene Materials for CO_2 Capture and Transformation

Dirigida per:

Dr. Ángel Morales-García — Universitat de Barcelona

Prof. Francesc Illas i Riera — Universitat de Barcelona

Tutor:

Dr. Francesc Viñes Solana

Universitat de Barcelona

Barcelona, 2023

“Nothing in life is to be feared, it is only to be understood. Now is the time to understand more, so that we may fear less.”

Marie Curie

Acknowledgements

Em sembla la part més difícil de la tesi fer aquesta pàgina d'agraïments i per por d'oblidar-me algú de tots els que m'han donat suport durant aquests últims anys.

Primerament, vull agrair als meus directors de tesi, el Dr. Ángel Morales i el Prof. Francesc Illas, sense oblidar al meu tutor, en Dr. Francesc Viñes, que em van donar aquesta oportunitat. Qui hauria imaginat que faria el TFG de morros totes les setmanes i acabaria fent la tesi?

També agrair als meus companys del 425, Raúl, Juanjo, Joan, Martí i Piqué. Companys de despatx que, encara que no va ser molt de temps per culpa de la pandèmia, van fer d'una de les millors èpoques a la Universitat. A més, agrair a Piqué i Lorena, que van ajudar-me des del TFG i durant el màster abans de la tesi, sempre ho recordaré. També m'agradaria afegir als companys que encara que no estan presents en el dia a dia, m'han ajudat en alguna cosa o un altre durant aquests anys, com la Hellensita.

Afegir un agraïment a totes les persones que he conegut al llarg d'aquests anys i que han influït directa o indirectament en la tesi. Els companys del màster de professorat, en Dani, Jorge i Jose, la Georgina... companys que han fet que l'escriptura de la tesi fos més amena i divertida, amb les converses sobre aquesta ("converses" o com els hi he donat la xapa). Als docents que he retrobat aquest any com la Pili o la Montse, que m'han tornat a fer veure per què vaig escollir la ciència com a camí de vida.

Agrair a la meva família, que han estat sempre darrera meu per donar-me suport, encara que a dia d'avui no els hi hagi explicat molt bé de que

va la tesi. Als meus pares, per donar-me la oportunitat d'estudiar sense maldecaps i estar sempre, la meva germana i els meus nebots (Oriol, Pau i Jan) , presents en el meu dia a dia i sense els quals tot seria molt més avorrit i al meu germà. No oblidar a la meva cosina Sara, que va estar durant el grau, el màster i la tesi fent de suport i encara present avui.

Ara si, a la meva persona preferida de l'Univers, l'Óscar, ha estat un pilar a la tesi i és un pilar a la meva vida. Un suport incommensurable diari des de que vaig començar fins a finalitzar. Mai podré tornar-te el que m'has donat durant aquests anys.

PD: Un agraïment a qui pràcticament podria ser coautor de la tesi, la Piña, que literalment ha estat present a tota la tesi: totes les reunions online, tota l'escriptura del document, la recerca... Inclús ara mateix, escrivint els agraïments ella està a la taula.

Abstract

Low-dimensional transition metal carbides known as MXene are suitable catalysts with implications in heterogeneous catalysis given their similar properties with the transition metal carbides (TMCs) with the advantage of high surface area. In particular, MXenes active easily carbon dioxide (CO_2) emerging as solutions to fight against the climate change. This motives the study of using MXenes as heterogeneous catalysis in processes where CO_2 is transformed into valuable chemical products.

In this Doctoral Thesis, the abatement of CO_2 by MXene nitrides is discussed through the novel kinetic phase diagrams. This allows one identifying pressure-temperature conditions at which the MXene capture CO_2. To distinguish different the atomic stacking of MXene, the vibrational modes of CO_2 molecule are used. The Reverse Water Gas Shift (RWGS) reaction is investigated considering the Mo_2C MXene as catalyst. The analysis of the thermodynamic, kinetic, and microkinetic aspects confirm the feasibility of MXenes to transform CO_2 into CO.

Resum en Català

Els carburs metàl·lics de baixa dimensionalitat, MXene, han emergit com a candidats per a catàlisi heterogènia donades les propietats similars amb els seus homòlegs tridimensionals, però amb l’avantatge de tenir una superfície superior. Això, És una motivació clara a l’estudi de l’ús de MXenes com a catalitzador heterogeni en processos on el CO_2 es transforma en productes químics de valor afegit.

En aquesta tesi doctoral, la reducció de CO2 per part de nitrurs de MXene es discuteix a través dels nous diagrames de fase cinètica. Això permet identificar condicions de temperatura i pressió en què el MXene captura CO_2. Per distingir els diferents apilaments atòmics del MXene, s'utilitzen els modes vibracionals de la molècula de CO_2. La reacció Inversa de Desplaçament d’Aigua en Gas (RWGS) s'investiga considerant el MXene Mo_2C com a catalitzador. L'anàlisi dels aspectes termodinàmics, cinètics i microcinètics confirmen la viabilitat de MXenes per transformar CO_2 en CO.

Abbreviations

TMC	**T**ransition **M**etal **C**arbides
RWGS	**R**everse **W**ater **G**as **S**hift reaction
TRL	**T**echnology **R**eadiness **L**evel scale
CCS	**C**arbon **C**apture and **S**torage
CCU	**C**arbon **C**apture and **U**sage
EOR	**E**nhanced **O**il **R**ecovery
EGR	**E**nhanced **G**as **R**ecovery
scCO_2	**s**uper**c**ritical **CO_2**
TM	**T**ransition **M**etals
DRM	**D**ry **R**eforming of **M**ethane
HF	**H**artree-**F**ock
DFT	**D**ensity **F**unctional **T**heory
TST	**T**ransition **S**tate **T**heory
BOA	**B**orn-**O**ppenheimer **A**pproximation
CI	**C**onfiguration **I**nteraction
LDA	**L**ocal **D**ensity **A**pproximation
VWN	**V**olko-**W**ilk-**N**usair
CA	**C**eperly and **A**dler

GGA	**G**eneralized **G**radient **A**pproximation
PBE	**P**erdew-**B**urke-**E**rzenhof
meta-GGA	**M**eta-**G**eneralized **G**radient **A**pproximation
TPSS	**T**ao-**P**erdew-**St**aroverov-**S**cuseria
PKZB	**P**erdew-**K**urth-**Z**upan-**B**laha
PW	**P**lane-**W**aves
VASP	**V**ienna **A**b Initio **S**imulation **P**rogram
PAW	**P**rojected **A**ugmented **W**ave
bcc	**b**ody-**c**entered **c**ubic
fcc	**f**ace-**c**entered **c**ubic
hcp	**h**exagonal **c**losed **p**acked
PES	**P**otential **E**nergy **S**urface
CI-NEB	**C**limbing **I**mage **N**udged **E**lastic **B**and method
$\boldsymbol{E_{ads}}$	**A**dsorption **E**nergy
ZPE	**Z**ero-**P**oint **E**nergy
TS	**T**ransition **S**tate
TOF	**T**urn **O**ver **F**requency
ODEs	**O**rdinary **D**ifferential **E**quations

List of Figures

Abbreviations

List of Figures

CHAPTER ONE

Introduction

Chapter 1

1.1 Motivation and Outline

The current climate emergency calls for realistic and suitable solutions to fight against the climate change. Several strategies have been proposed including catalytic solutions. Indeed, the transition metal carbides (TMCs) have been proposed as plausible heterogeneous catalyst to activate and capture CO_2, the main contributor to the greenhouse effect and, consequently, the main actor of global warming, ocean acidification and melting of the poles.

Recently, low-dimensional carbides/nitrides have been synthetized. These bidimensional materials are known as MXenes. These materials can be seen as the bidimensional counterpart of TMCs, thus one wonder about the suitability of MXenes as heterogeneous catalysts for activating CO_2 and contribute to the minimization of the impact in the greenhouse effect. Therefore, the goal of this Doctoral Thesis is focused on the study of the performance of MXenes on the conversion of CO_2. To achieve this goal, three main applications will be described through, (i) the abatement of CO_2 by MXene nitrides, (ii) the effect of the MXene stacking on the activation of probe molecules with interest in heterogeneous catalysis, and (iii) the catalytic performance of MXenes in the reverse water gas shift (RWGS) reaction.

The present Doctoral Thesis starts with a brief introduction of the current carbon capture methods, main features of MXenes structure and

CO_2 transformation methods. In Chapter 2, the background theory and the computational methods are described, together structures and, subsequent analysis. Further computational concerns are explained in Chapter 3 within multiscale approaches, the newly developed kinetic phase diagrams, and the microkinetic modelling. Chapters 4, 5 and 6 contain the main results of this Doctoral Thesis within discussion. Chapter 4 is focused on nitride MXenes, specifically in the adsorption and activation of CO_2 on bare nitride MXenes with different thickness and compositions. Chapter 5 discusses the effect of stacking on carbide MXenes, and, finally, Chapter 6 contains a full description of the RWGS reaction on carbide MXenes, specifically on bare Mo_2C. This Doctoral thesis finishes with Chapter 7, where the main conclusions are given. Chapters 8 correspond to contributions to the published papers and finally, the appendix of the published papers.

1.2 The climate change: problems and challenges

The anthropogenic emissions coming from the use of fossil fuels and deforestation[1,2] has led to a progress increasing of the concentration of CO_2, H_2O, CH_4 and NO_x gases among others in the atmosphere. These gases have the capacity of absorbing the heat emitted by the Earth avoiding its emission to the external space. Such a heat is returned to the Earth promoting a global warming process. These gases are thus known as greenhouse gases and, in particular, the high CO_2 concentration also induces the acidification of the oceans. Among mentioned gases, CO_2 is not the one mostly contributing to the greenhouse effect; however, its concentration in the atmosphere is the largest one, therefore becoming the main contributor.

The current atmospheric concentration of CO_2 is 421 ppm with an annual growth of 2.7% in the last decade or 60% since 1990.[3] These concentrations have direct consequences in the environment such as the increasing of global temperature by 1.18 ºC and sea levels due to the melting of poles. However, not only environmental changes will occur, social and economic consequences derived from the alterations on weather like harvest declining, shorts on the production chain and the consequence lack of food and water.[4]

There are no doubts that overcoming this global issue is on the table of scientific agenda of countries. Thus, the last treaty on climate change, Paris Agreements,[5] brings an ambitious series of goals to reduce global CO_2 atmospheric concentration above the pre-industrial values, around 280 ppm.[6] To reach this goal, we have to reduce to half the CO_2 emissions by 2030 and reach zero emissions by 2050. This great challenge must be coupled with the development of eco-friendly energy sources (*e.g.*, solar and wind energy) and waste-to-product strategies (*e.g.*, carbon capture technologies).[7] Eco-friendly energy sources provide an alternative way to obtain clean energy at relative low cost. However, this transition energy has to be coupled with the reduction of the current concentration of greenhouse gases. For this reason, technologies for a selective separation and capture of CO_2 have arisen interest.

Nevertheless, it is needed to know whether or not these technologies are prepared to fulfil the requirements of Paris. For this reason, the Technology Readiness Level scale was created (TRL). First described by Mankins,[8] this scale describes the technological maturity of technology and is used as a tool to administrate the progress of research and development activity of technological issues, being thus how advanced is a technology in the process of creation and utilization. For instance, the first six levels describe technologies at laboratory scale whereas the three remaining show systems with prototypes, complete or operational. Methods that currently reach 6 or more could fulfil the requirements of Paris by 2030 and 1 or more by 2050, see Figure 1.1.

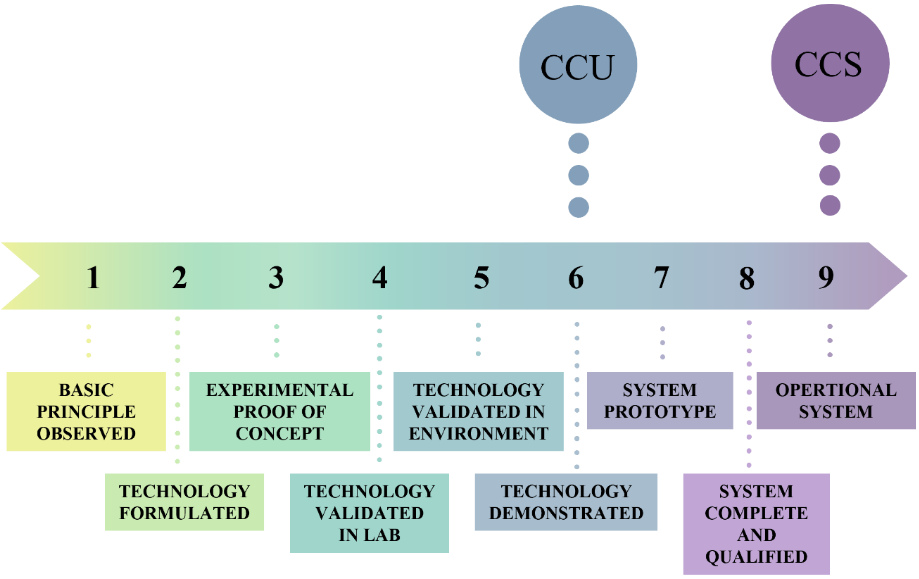

Figure 1.1. Scale of Technology Readiness Level. Lower values correspond to immature technologies while higher values correspond finished technologies. CCU and CCS present high values of TRL levels.

Thereby, the list of technologies capable to perform these demands is quite diverse. Nevertheless, materials capable to capture

CO_2, store and use it are in high tiers of TRL. For this reason and more that will be presented in section 1.3, these materials have arisen interest.

1.3 Carbon Capture: Storage and Utilisation

Carbon Capture and Storage (CCS) is an emerging technology that uses active solid substrates for trapping CO_2, allowing its storage.[9] These types of technologies can be employed to reduce the CO_2 concentration in the atmosphere meanwhile reducing emissions. More interesting is the Carbon Capture and Usage (CCU) technology because it goes a step further transforming CO_2 into more valuable chemical products. The combinations of both strategies could provide an eco-friendly strategy in a long-term.

Currently CCS technologies includes a large group of technologies that involves different processes for CO_2, including capture, separation, transport and storage. However, processes based on Enhanced Oil Recovery (EOR) and Enhanced Gas Recovery (EGR) are the upmost representative technologies.[10] Indeed, EOR captures supercritical CO_2 ($scCO_2$) by injecting the gas because in such a state the microscopic displacement efficiency improves significantly. Here residual oil and gases are extracted, and the CO_2 remains stored approx. 139-320 GT of CO_2.[11] Gas reservoirs show even a larger capacity to store CO_2 i.e., 390-750 GT.[12] However, EGR based technology presents a more complex process due to several factors—adsorption of gases on the surface of the rocks, the CO_2 break possibility and, the miscibility of natural gas and CO_2—among other.

Up to here, technologies based on the storage have been briefly described. However, one wants to move forward the usage and transformation of CO_2 as implemented in CCU strategies. Thus, the use of CO_2 can be chemical, technological and even biological, being the main effort the improvement of traditional processes while reducing CO_2 emissions. Starting with these technologies, CO_2 as a solvent is the first step. Liquid CO_2 and $scCO_2$ act as solvent in numerous processes such as the decaffeination of coffee and tea[13] or the extraction of flavours and essential oils,[14] reporting multiples advantages such as lower amounts of needed solvent and energy savings. Another process successful is the hydrogenation reaction in $scCO_2$ atmosphere at industrial scale. For example, the hydrogenation of nitrile to primary amines or the hydrogenation of oleic acid catalysed by platinum, where the $scCO_2$ improves the yield from 95% to 97%.[15,16] Hereunder, one can consider CO_2 as a direct feedstock, where this molecule is employed to produce chemicals. Here, one can distinguish between CO_2 as a precursor for organic compounds and as a precursor for fuels. Thus, carboxylation of substrates,[17] formation of carbamic acids[18] and the formation of linear and cyclic carbonates[19] are some examples of the first group. Regarding the formation of fuels, in section 1.6 some extended explanation is detailed.

However, even though CCU materials present minor drawbacks as the conventional methods, the development of suitable catalysts capable to favour the activation and transformation of CO_2 are in demand, promoted by the urge of improvement.

1.4 The Need of Catalysis in CCU

The high stability of CO_2 represents a huge challenge for its possible utilization as in CCU technologies. To overcome this obstacle, efficient, active, and selective catalysts are needed. The term catalyst was first used by Berzelius in 1835 on the definition: "*Catalyst are substances that by their mere presence evoke chemical reactions that would not otherwise take place".* Hereinafter, Wilhelm Ostwald reformulated it defining *"a catalyst is a substance that changes the velocity of a chemical reaction without itself appearing in the end products".* IUPAC catalysis definition is a *substance that increases the rate of a reaction without modifying the overall standard Gibbs energy change in the reaction.*[20] This substance, called catalyst, is both reactant and product and provides a new reaction mechanism with new transition states, displaying lower energy requirements. To understand the impact of catalysis in our society, one has to think that over 90% of industrial chemicals are obtained using catalysts.[21]

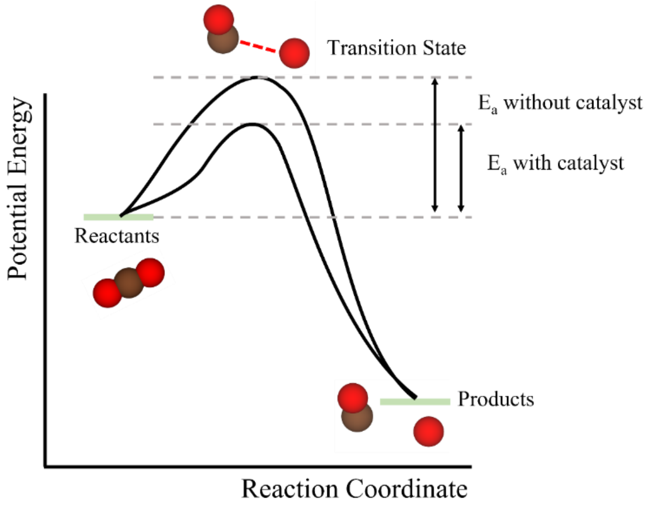

Figure 1.2. Scheme of a catalysis reaction coordinate path including reactant, transition state, and product.

Catalysis can be classified in homogeneous and heterogeneous. The first one only involves one phase. This means that both reactants and catalyst are in solution. On the other hand, the heterogeneous catalysis reaction occurs at the interface or near, involving two phases. These catalysts are mostly solid-state surfaces or nanostructures, which have more freedom degrees than molecules in the gas. Hence, gas molecules trend to diffuse and interact with the surface of the catalyst forming bonds. Further recombination can take place in multiple steps, followed by the desorption of final products and diffusion.

Heterogeneous catalysis is one of the pillars of industry given that not only allows some reactions to work but also improves the cost-efficiency of them. Haber-Bosch process, used to synthetize ammonia from nitrogen and hydrogen gases using Osmium as catalyst, is probably the most famous example of heterogeneous catalysis owing to it allowed a practically unlimited production of ammonia for fertilizers, and therefore, the growth on population of the Century 20th.[22,23] Indeed, transition metals (TM) are considered the classical heterogeneous catalyst triggered by their intrinsic properties. These encompasses a large variety of oxidation states, an electronic structure with an incomplete *d*-shell, being able to share or withdraw electrons from reactants. However, pristine metals are not the only with these properties: transition metal carbides and nitrides share these properties and are abundant and cheaper, being more affordable for industrial purposes. For these reasons, transition metal carbides and nitrides are being increasingly considered for CCU and CCS utilization[24] and this is further considered in the present thesis.

1.5 Transition Metal Carbides as catalyst

Transition metal carbides and nitrides are widely known for their interesting and versatile features such as high melting points or superconductivity. These materials, which combine the physical properties of ionic crystals, covalent solids, and transition metal, show high melting temperatures and hardness. Presented by Levy and Boudart[25] in 1973, these materials are comparable with the noble or Pt-group metals. However, whereas transition metal carbides and nitrides present comparable catalytic properties, this group of materials are more abundant and cheaper, being thus, more affordable for industrial purposes.

Recently, a newly family of low-dimensional carbides and nitrides have been synthetized. The so-called MXenes,[26,27] discovered by Michael Barsoum and Yury Gogotsi, present a two-dimensional structural framework, similar to graphene[28] or boron nitride.[29] MXenes show a versatile composition with the general formula $M_{n+1}X_nT_x$ where n ranges from 1 to 3; M to an early transition metal; X carbon or nitrogen and T_x stands for the surface termination. Thus, these materials can display a large diversity of thickness and composition according to the used precursor: the MAX phase. Currently, there are more than 150 of these phases.[30]

MAX phases are polycrystalline nanolaminates of ternary carbides and nitrides with $M_{n+1}AX_n$ formula, where M and X are the same as MXenes and A belongs to an element of the group 13 and 14. Here, the $M_{n+1}X_n$ layers are stable but the M-A bonds are more chemically active. Hence, this layer can be removed with a selective etching and exfoliation, being the most common method the wet etching. On this top-down procedure, the etching agents are HF, LiF/HCl, or NH_4HF_2, and promotes the functionalization of MXenes with a mixture of -OH, -O and -F.[31-33] Nevertheless, recent studies reported new alkali-halides routes for the MXene synthesis. Here, termination is a halide (T_x= -Cl, -Br)[32,33] and the bond M-T is weaker than the MXenes with -OH, -O and -F terminations. Thus, these materials are suitable for the recently described post-processing strategy to obtain clean or bare MXenes, where the hydrogenation reaction is combined with high temperature to remove all terminations on the structure.[33,34]

Thereby, MXene materials have shown a large variety of properties, including electronic, optical, mechanical, and chemical. Some application examples are electromagnetic interference shielding, energy storage and harvesting, biomedicine, sensors and catalysis. In fact, these materials are promising candidates for capturing CO_2 and its subsequent conversion.[35,36]

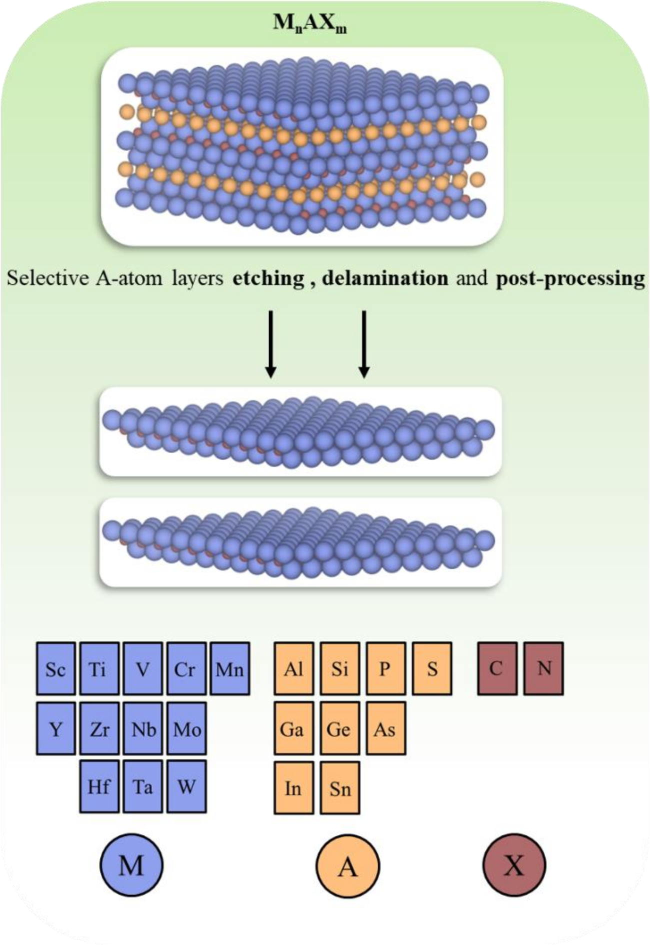

Figure 1.3. Scheme of formation of MXenes through the selective etching of the A layer.

1.6 The CO_2 conversion challenge

As mentioned on section 1.3, CO_2 is a feasible feedstock for many reactions of interest. For example, dry reforming of methane (DRM)[37] produces syngas at high temperature and low pressures using a specific heterogeneous catalyst (cat.)

$$CO_2 + CH_4 \xrightarrow{cat.} CO + H_2O \ \Delta\mathrm{H} = 247 \text{ kJ mol}^{-1},$$

and dry reforming of ethanol (DRE)[38] uses agricultural raw materials,

$$CO_2 + C_2H_5OH \xrightarrow{cat.} 3CO + 3H_2 \ \Delta\mathrm{H} = 297 \text{ kJ mol}^{-1}$$

or glycerol

$$CO_2 + C_3H_8O_3 \xrightarrow{cat.} 4CO + 3H_2 + H_2O \Delta\mathrm{H} = 292 \text{ kJ mol}^{-1}.$$

However, there are some reactions that take advantage of this molecule as a first step to a larger process. Fischer-Tropsch process[39] for example, hydrogenates the CO obtained from the RWGS reaction.

The RWGS reaction is one of the most known examples to convert CO_2 into more value-added chemicals, such as CO. Here, a catalytic process reduces CO_2 into CO, a C-1 building block used for feedstock and fuels and the base of the so-called syngas mixture ($CO:H_2$).

$$CO_2 + H_2 \rightarrow CO + H_2O \ \Delta\mathrm{H} = 42.1 \text{ kj mol}^{-1}$$

However, the RWGS is not that simple, the mechanism presents three different competitive ways according to the formation of the first intermediate. Thus, the paths are via redox, via associative formate (HCOO) and via associative carboxyl (COOH), see Figure 1.4. Moreover, it is important to note that the RWGS is an endergonic process, even though this can be modulated with high temperatures and H_2:CO_2 ratios.[40]

Among the actual catalysts, thanks to this thermal stability and high oxygen mobility, iron-based catalysts are considered one of the most suitable catalysts for the reaction on high temperatures, whereas copper is the appropriate for the lower ones.[41,42] However, transition metals such as Pt, Ni or Co have shown suitable performances towards the reaction[43-45] and transition metal carbides and nitrides such as α- and β-Mo_2C[46,47] have exhibit similar features. Nevertheless, the aforementioned MXenes show properties compatible with the reaction and may be interesting material to explore the RWGS mechanism.

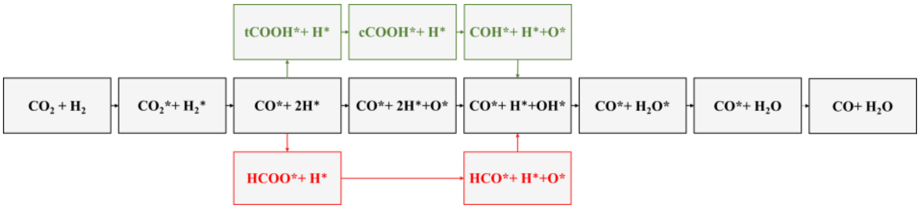

Figure 1.4. Reverse Water Gas Shift scheme process including the three reaction sequences. Black refers to redox, red to associative formate path (HCOO) and green, to associative carboxyl path (COOH).

1.7 References

1. van der Werf, G.; Morton, D.; DeFries, R.; CO_2 Emissions from Forest Loss. *Nature Geosci*, **2009**, 2, 737–738.
2. D'Alessandro, D. M.; Smith, B.; Long, J. R. Carbon Dioxide Capture: Prospects for New Materials, *Angew. Chem. Int. Ed.*, **2010**, 49, 6058–6082.
3. *"Carbon dioxide now more than 50% higher than pre-industrial levels | National Oceanic and Atmospheric Administration"*. www.noaa.gov. *Retrieved 14 June 2022.*
4. Arnell, N.W.; Lloyd-Hughes, B. The Global-Scale Impacts of Climate Change on Water Resources and Flooding Under New Climate and Socio-Economic Scenarios. *Climatic Change*, **2014**, 122, 127–140.
5. Horowitz, C. A. Paris Agreement. *International Legal Materials*, **2016**, 55, 7 ,40 – 755.
6. Wigley, T.M.L. The Pre-industrial Carbon Dioxide Level. *Climatic Change*, **1983**, 5, 315–320.
7. Wilberforce, T.; Olabi, A.G.; Sayed, E. T.; Elsaid, K.; Abdelkareem. M. A. Progress in Carbon Capture Technologies. *Sci. Total Environ.*, **2021**, 761, 143203.
8. Mankins, J. C. Technology readiness levels. *White Paper*,**1995**, 6, 1995.
9. MacDowell, N.; Florin, N.; Buchard, A.; Hallett, J.; Galindo, A.; Jackson, G.; Adjiman, C. S.; Williams, C. K.; Shah, N. ; Fennell, P. An overview of CO_2 Capture Technologies, *Energy Environ. Sci.*, **2010**, 3, 1645–1669.

10. Thomas, S. Enhanced Oil Recovery – An Overview. *Oil Gas Sci. Technol.*, **2008**, 63, 9-19.
11. Godec, M.; Kuuskraa, V.; Van Leeuwen, T.; Melzer, L. S.; Wildgust, N. CO_2 Storage in Depleted Oil Fields: The Worldwide Potential for Carbon Dioxide Enhanced Oil Recovery. *Energy Procedia*, **2011**, 4, 2162-2169.
12. Cuéllar-Franca, R. M. ; Azapagic, A. Carbon Capture, Storage and Utilisation Technologies: A Critical Analysis and Comparison of their Life Cycle Environmental Impacts, *J. CO_2 Util.*, **2015**, 9, 82–102.
13. De Marco, I.; Riemma, S.; Iannone, R. Supercritical Carbon Dioxide Decaffeination Process: A Life Cycle Assessment Study. *Chemical Engineering Transactions*, **2017**, *57,* 1699-1704.
14. Revercheron, E.; Porta, G. D.; Gorgoglione, D. Supercritical CO_2 Extraction of Volatile Oil from Rose Concrete. *Flavour Fragr J.,* **1998**, 12, 37-41.
15. Chatterjee, M.; Kawanami, H.; Sato, M.; Ishizaka, T.; Yokoyama, T.; Suzuki, T. Hydrogenation of Nitrile in Supercritical Carbon Dioxide: a Tunable Approach to Amine Selectivity. *Green Chem.*, **2010,** 12**,** 87-93.
16. Zhao, F.; Ikushima, Y.; Arai, M. Hydrogenation of Nitrobenzene with Supported Platinum Catalysts in Supercritical Carbon Dioxide: Effects of Pressure, Solvent, and Metal Particle Size. *J. Catal.*, **2004**, 224, 479-483.

17. Yahn, S.S.; Fu, Q.; Liao, L. L.; Sun, G. Q.; Ye, J. H.; Bo-Xue Y. Z.; Yu, D.G. Transition Metal-Catalyzed Carboxylation of Unsaturated Substrates with CO_2. *Coord. Chem. Rev.,* **2018**, 374, 439-463.

18. Dijkstra, Z. J.; Doornbos, A. R.; Weyten, H.; Ernsting, J. M.; Elsevier, C. J.; Keurentjes. J. T. F. Formation of Carbamic Acid in Organic Solvents and in Supercritical Carbon Dioxide. *J. Supercrit. Fluids*. **2007**, 41, 109-114.

19. Lopes, E. J. C.; Ribeiro, A. P. C; Martins, L. M. D. R. S. New Trends in the Conversion of CO_2 to Cyclic Carbonates. *Catalysts*. **2020**, 10, 479-493.

20. *IUPAC. Compendium of Chemical Terminology, 2nd ed. (the "Gold Book"). Compiled by A. D. McNaught and A. Wilkinson. Blackwell Scientific Publications, Oxford (1997). Online version (2019-) created by S. J. Chalk. ISBN 0-9678550-9-8.*

21. de Vries, J. G.; Jackson, S. D. Homogeneous and Heterogeneous Catalysis in Industry. *Catal. Sci. Technol*., **2012**, 2, 2009-2009.
22. Smil, V. Detonator of the Population Explosion. *Nature,* **1999**, 400, 415.
23. Erisman, J. W.; Sutton, M. A.; Galloway, J.; Klimont, Z.; Winiwarter, W. How a Century of Ammonia Synthesis Changed the World. *Nat. Geosci.,* **2008**, 1,636-639.
24. Ranjan, P.; Saptal, V. B.; Bera, K. Recent Advances in Carbon Dioxide Adsorption, Activation and Hydrogenation to Methanol using Transition Metal Carbides. *ChemSusChem*., **2022**, 15, 202201183.

25. Levy, R.B.; Boudart, M. Platinum-Like Behaviour of Tungsten Carbide in Surface Catalysis, *Science*, **1973**, 181, 4099, 547-549.
26. Presser, M. V.; Lu, J.; Niu, J.; Heon, M.; Hultman, L.; Gogotsi, Y.; Barsoum, M. W. Two-Dimensional Nanoscrystals Produced by Exfoliation of Ti_3AlC_2. *Adv. Mater.*, **2011**, 23, 4248−4253.
27. Naguib, M.; Gogotsi, Y.; Barsoum, M. W. Ten Years of Progress in the Synthesis and Development of MXenes. *Adv. Mater.*, **2021**, 33, 2103393.
28. Yan, Y.; Shin, W.I.; Chen, H. *et al.* A Recent Trend: Application of Graphene in Catalysis. *Carbon Lett.*, **2021**, 31, 177–199.
29. Dong, J.; Gao, L.; Fu, Q. Hexagonal Boron Nitride Meeting Metal: A New Opportunity and Territory in Heterogeneous Catalysis *J. Phys. Chem. Lett.*, **2021**, 12, 39, 9608–9619.
30. Gonzalez-Julian, J. Processing of MAX phases: From Synthesis to Applications. *J. Am. Ceram. Soc.*, **2021,** 104, 659-690.
31. Anasori, B.; Lukatskaya, M. R.; Gogotsi, Y. 2D Metal Carbides and Nitrides (MXenes) for Energy Storage. *Nat. Rev. Mater.*, **2017**, 2, 16098.
32. Alhabeb, M.; Maleski, K.; Anasori, B.; Lelyukh, P.; Clark, L.; Sin, S.; Gogotsi, Y. Guidelines for Synthesis and Processing of Two-Dimensional Titanium Carbide ($Ti_3C_2T_x$ MXene). *Chem. Mater.*, **2017,** 29, 7633−7644
33. Kamysbayev, V.; Filatov, A. S.; Hu, H.; Rui, X.; Lagunas, F.; Wang, D.; Klie, R. F.; Talapin, D. V. Covalent Surface Modifications and Superconductivity of Two-Dimensional Metal Carbide MXenes. *Science***, 2020**, 369, 979−983.

34. Seredych, M.; Shuck, C. E.; Pinto, D.; Alhabeb, M.; Precetti, E.; Deysher, G.; Anasori, B.; Kurra, N.; Gogotsi, Y. High-Temperature Behavior and Surface Chemistry of Carbide MXenes Studied by Thermal Analysis. *Chem. Mater.*, **2019**, 31, 3324−3332.
35. Persson, I.; Halim, J.; Lind, H.; Hansen, T. W.; Wagner, J. B.; Näslund, L. Å.; Darakchieva, V.; Palisaitis, J.; Rosen, J.; Persson, P. O. Å. 2D Transition Metal Carbides (MXenes) for Carbon Capture. *Adv. Mater*., **2019**, 31, 1805472.
36. Morales-García, Á.; Calle-Vallejo, F.; Viñes, F. MXenes: New Horizon in Catalysis. *ACS Catal.*, **2020,** 10, 22, 13487–13503.
37. Usman, M.; Wan Daud, W. M. A.; Abbas, H. F. Dry Reforming of Methane: Influence of Process Parameters**—**A Review. *Renewable Sustainable Energy Rev.*, **2015**, 45, 710-744.
38. Yu, J.; Odriozoloa, J. A.; Reina, T. M. Dry Reforming of Ethanol and Glycerol: Mini-Review. *Catalyst*, **2019**, 9, 1015.
39. Van Santen, R. A.; Markvoort, A. J.; Fillot, I. A. W; Ghouri, M. M.; Hensen, E. J. M. Mechanism and Microkinetics of the Fischer-Tropsch Reaction. *Phys. Chem. Chem. Phys*., **2013**, 15, 17038-17063.
40. Whitlow, J. E.; Parrish, F. Operation, Modeling and Analysis of the Reverse Water Gas Shift Process, *AIP. Conf. Proc.*, **2003**, 654, 1116.
41. Pastor-Pérez, L.; Baibars, F.; Le Sache, E.; Arellano-García, H.; Gu, S.; Reina, T.R. CO_2 Valorisation via Reverse Water-Gas Shift Reaction Using Advanced Cs Doped Fe-Cu/Al_2O_3 Catalysts, *J. CO_2 Util.*, **2017**, 21, 423-428.

42. Chen, C.S.; Cheng, W.H.; Lin, S.S. Mechanism of CO Formation in Reverse Water-Gas Shift Reaction Over Cu/Al_2O_3 Catalyst. *Catal. Lett.,* **2000**, 68, 45-48.
43. Kim, S. S.; Lee, H. H.; Hong, S. C. A Study on the Effect of Support's Reducibility on the Reverse Water-Gas Shift Reaction over Pt Catalysts. *Appl. Catal. A*, **2012**, 423–424, 100–107.
44. Wang, L.; Liu, H.; Liu, Y.; Chen, Y.; Yang, S. Influence of Preparation Method on Performance of Ni-CeO2 Catalysts for Reverse Water-Gas Shift Reaction. *J. Rare Earths*, **2013**, 31, 559–564.
45. Sengupta, S.; Jha, A.; Shende, P.; Maskara, R.; Das, A. K. Catalytic performance of Co and Ni doped Fe-based Catalysts for the Hydrogenation of CO_2 to CO via Reverse Water-Gas Shift Reaction. *J. Environ. Chem. Eng.,* **2019**, 7, 102911.
46. Liu, X.; Kunkel, C.; Ramírez De La Piscina, P.; Homs, N.; Viñes, F.; Illas, F. Effective and Highly Selective CO Generation from CO_2 Using a Polycrystalline α-Mo_2C Catalyst. *ACS Catal.,* **2017**, 7, 4323–4335.
47. Ma, Y.; Guo, Z.; Jiang, Q.; Wu, K. H.; Gong, H.; Liu, Y. Molybdenum Carbide Clusters for Thermal Conversion of CO_2 to CO via Reverse Water-Gas Shift Reaction. *J. Energy Chem.,* **2020**, 50, 37–43.

CHAPTER TWO

Theoretical Background

Chapter 2

The present chapter describes the theoretical background used in this Doctoral Thesis. This Chapter starts with a brief description of the Hartree-Fock (HF) and Density Functional Theory (DFT) methods, followed by the description of computational models considering extended crystalline structure and surfaces. Finally, Transition State Theory (TST) that encompasses the methodology used to find transition state is described.

2.1 Schrödinger equation and the Hartee-Fock method

The goal of quantum methods is to describe the electronic structure of matter with the resolution of the non-relativistic time-independent Schrodinger equation.

$$\hat{H}\psi = E\psi \tag{2.1}$$

Herein, $\hat{H}$ is the Hamiltonian of the system, which is a lineal differential operator that depends on the coordinates of electron – **r** –, the coordinates of nuclei –**R**– and the interaction between them. Thus, the Hamiltonian for **N** electrons and **M** nuclei can be expressed as

$$\hat{H} = -\frac{1}{2}\sum_{i=1}^{N}\nabla_i^2 - \frac{1}{2}\sum_{j=1}^{M}\frac{1}{M_j}\nabla_j^2 - \sum_{i=1}^{N}\sum_{j=1}^{M}\frac{Z_j}{r_{i,j}}$$

$$+\sum_{i=1}^{N\text{-}1}\sum_{k>i}^{N}\frac{1}{r_{i,k}} + \sum_{j=1}^{M\text{-}1}\sum_{l>j}^{M}\frac{Z_j Z_l}{R_{j,l}} \qquad (2.2)$$

where the first two terms belong to the kinetic energy of electrons and nuclei, the third term is the Coulomb interaction (*i.e.*, interaction of the electrons with the nuclei), the last two terms stand for the repulsion between electrons and nuclei, respectively. Here, $\mathbf{M_j}$ is the ratio of the mass of nucleus **j** to the mass of an electron, and $\mathbf{Z_j}$ the atomic number of nucleus **j**.

To approach a solution of the time-independent Schrodinger equation it is customary to rely on the Born-Oppenheimer approximation (BOA).[1] This is based on the fact that nuclei are much heavier than electrons (the electron mass is 1836 times smaller than the proton). Therefore, in a first step, the kinetic energy of the nuclei (second term) of the nuclei is neglected, the repulsion between nuclei becomes a constant (fifth term) and, for a given position of the nuclei, the resulting equation depends on the electron coordinates only. Thereby, the electronic Hamiltonian can be decomposed in kinetic energy of electrons, potential repulsion between electrons and between nuclei and electrons Eq. (2.3)

$$\hat{H}_{el} = \sum_{i=1}^{N} \nabla_i^2 - \sum_{i=1}^{N} \sum_{j=1}^{M} \frac{Z_j}{r_{i,j}} + \sum_{i=1}^{N\text{-}1} \sum_{k>i}^{N} \frac{1}{r_{i,k}} \tag{2.3}$$

.

The solution of electronic Hamiltonian in Eq. (2.3) leads to an N-electron wave function depending parametrically on the position of the nuclei and to an electronic energy. Inserting the solutions of Eq. (2.3) in Eq. (2.1) shows that the electronic energy plus the nuclei repulsion correspond to the potential under nuclei motion takes place and leads to the important concept of potential energy surface. The solution of Eq. (2.3) is not a simple task as the motion of the electrons is correlated leading to a many-body problem. However, it is possible to find approximate solutions by assuming that electrons interacting with an average potential provided by the rest of electrons. This is the basis for the well-known Hartree-Fock (HF) method.[2]

Hartree-Fock is a variational method which makes use of an approximate form of the N-electron wave function. In particular, the ground state wave function is approximated by a single Slater determinant built of spinorbitals, to ensure fulfilling the antisymmetry principle. The spinorbitals are one-electron wave functions and its form is obtained such it minimizes the expectation value of the electronic energy of the system.

$$\left(\hat{H}_{HF} - E_{HF}\right)\varphi_{HF} = 0 \tag{2.4}$$

In practice, spinorbitals are chosen as a variational linear combination of known functions that are considered a basis set. Thanks to the antisymmetry, the Hartree-Fock methods accounts for electron correlation between two electrons with the same spin, i.e., it includes the so-called Fermi hole but neglects the Coulomb hole. Thus, the energy found by the Hartree-Fock method, E_{HF}, is higher than the exact energy of the ground state, E_0 and the difference between them is the *correlation* energy of the system Eq. (2.5).

$$E_{corr} = E_0 - E_{HF} \tag{2.5}$$

A significant number of methods exist that aim at including electron correlation in a more or less accurate way. Configuration Interaction (CI)[3] uses a variationally derived lineal combination of Slater determinants build from the Hartree-Fock spinorbitals. Møller-Plesset[4] uses the perturbation theory to approach the CI coefficients while Couple-Cluster uses the linked cluster theorem. All post-Hartree-Fock -methods provide accurate results of the electronic structure but at high computational costs, being expensive to current computational technology. Note also that, in general, Hartree-Fock and post-Hartree-Fock methods neglects relativistic effects as they aim at solving the non-relativistic Schrödinger equation.

2.2 Density Functional Theory

Density functional theory (DFT)[5] is an alternative, broadly used, methods of termed *ab initio* even if it contains some parameters external to the theory and is best described as a *first principles* approach. DFT does not require the knowledge of the N-electron wave function and allows one to carry out electronic structure calculations and to approach the ground state energy of molecules, surfaces, and solids from the one electron density–$\rho(\vec{r})$–only. This feature permits to treat larger systems than the Hartree-Fock and other wave function-based methods. In DFT, the ground state energy is determined by the ground state electron density $\rho(\vec{r})$ implying that the ground state energy is a functional of the density as expressed by Eq. (2.6)

$$E = f(\rho\overrightarrow{(r)}) \tag{2.6}$$

with the constraint that the integral of $\rho(\vec{r})$ over the total space must be the equal to the total number of electrons of the system and also that it must vanish when ρ tends to infinite. This is:

$$\int \rho(\vec{r})\mathrm{d}\vec{r} = N \tag{2.7}$$

$$\rho(\vec{r} \rightarrow \infty) = 0 \tag{2.8}$$

Historically, DFT arises from the Thomas-Fermi model,[6,7] which was the first to employ to calculate the kinetic energy as a functional of the density. However, modern DFT starts with the famed Hohenberg and Kohn theorems.[8]

2.2.1 Hohenberg-Kohn theorems

First reported in 1964, the Hohenberg and Kohn theorems provide the foundations of modern Density Functional Theory. The introduced two theorems states that:

- **First theorem:** “The external potential $V_{ext}(\vec{r})$ is (to within a constant) a unique functional of $\rho(\vec{r})$. Since, in turn $V_{ext}(\vec{r})$ fixes the Hamiltonian we see that, in principle, the full many particles ground state is a unique functional of $\rho(\vec{r})$”.
- **Second theorem:** “The ground state energy can be obtained variationally. This is the density that minimizes the total energy is the exact ground state density”.

The first theorem stablishes that the ground state electronic density cannot be derived from two different external potentials $V_{ext}(\vec{r})$, only differing in a constant. Thus, for a given external potential, the total energy is determined by the ground state electron density the $\rho_o(\vec{r})$ as

$$E[\rho] = T[\rho] + V_{ee}[\rho] + T_{Ne}[\rho] \tag{2.9}$$

$$E[\rho] = \int \rho(\vec{r}) V_{ext}(\vec{r}) dr + F_{HK}[\rho] \tag{2.10}$$

$$F_{HK} = T[\rho] + V_{ee}[\rho] \tag{2.11}$$

where $F_{HK}[\rho]$ is the Hohenberg-Kohn functional, a universal functional involving an electron-electron interaction term $V_{ee}[\rho]$ and a kinetic energy $T[\rho]$, the remaining nuclei-electron interaction term $T_{Ne}[\rho]$ is directly obtained from the external potential as shown in Eq. (2.9). The problem for practical applications is that $F_{HK}[\rho]$ is unknow, an issue that was solved elegantly, not without approximation, by Kohn and Sham as described below.

2.2.2 Kohn-Sham method

Almost a year after the two main DFT theorems were proven, Walter Kohn and Lu Sham proposed a practical formalism to approach $F_{HK}[\rho]$.[9] This consists of introducing an auxiliar fictious system of non-interacting electrons with the same $\rho(\vec{r})$ density of the real system. This allows to write the density from a set of independent one electron functions called the Kohn-Sham orbitals,

$$\rho_{KS}(r) = \sum_{i=1}^{N} |\psi_i(r)|^2 \qquad (2.12).$$

.

From the Kohn-Sham orbitals the kinetic energy term can be obtained as

$$T_S[\rho] = -\frac{1}{2}\sum_{i=1}^{N}\langle\psi_i(r)|\nabla^2|\psi_i(r)\rangle \qquad (2.13).$$

Hence, Eq. (2.14) can be rewritten as

$$F_{HK} = T_s[\rho] + +V_{ee}[\rho] = T_s[\rho] + J[\rho] + E_{xc}[\rho] \qquad (2.14)$$

where $T_s[\rho]$ is the kinetic term of the non-interacting systems and, by analogy to the Hartree-Fock formalism, the $V_{ee}[\rho]$ terms has been splitted into a $J[\rho]$ term corresponding to the classical Coulomb repulsion between the ρ densities and the $E_{xc}[\rho]$ term known as the exchange-correlation energy functional accounting for all missing interactions including exchange as electrons are fermions and no reference to the Pauli principle is made, correlation to correct the classical Coulomb interaction and, the difference between the real system and the non-interacting system kinetic energies. Note that this last functional exact form is unknown, but can be expressed as

$$E_{xc}[\rho(r)] = T[\rho] - T_s[\rho] + V_{ee}[\rho] - J[\rho] \qquad (2.15),$$

where $T[\rho] - T_s[\rho]$ is the difference between the kinetic energy of the interacting and non-interacting system and $V_{ee}[\rho] - J[\rho]$ term, is the exchange-correlation distribution.

2.2.3 Exchange-correlation functionals

As stated in section 2.2.2, the exact form of $E_{xc}[\rho]$ is unknown, but several approaches have been proposed to describe an approximation of it. These functionals are classified by the relation accuracy/computational cost and are gathered in the so-called Jacob's Ladder of functional improvements,[10] being the last step the "divine" or universal functional.

The first step on the Jacob's Ladder and the simplest to calculate the $E_{xc}[\rho]$ is the Local Density Approximation (LDA), where is assumed that the density can be treated locally as that of a homogeneous electron gas of uniform density. This functional have shown suitable performance for some properties of metallic systems such as bond lengths and lattice parameters. Nevertheless, the lack of accuracy of non-homogeneous systems and the overestimation of bond energies have some disadvantages. Vosko-Wilk-Nusair (VWN)[11] and Ceperly and Adler (CA)[12] are some forms of this functional.

The Generalized Gradient Approximation (GGA) was developed as an improvement to the LDA functionals, being thus, the next level in the Jacobs Ladder. This level of approximation adds the gradient of the density, $\nabla\rho$, to the density itself, accounting the non-homogeneity of the real electron density and allowing a semilocal approximation. Perdew-Wang 91[13] and its successor, Perdew-Burke-Erzenhof (PBE)[14] are some of the most common functionals of this group, free of parameters fitted

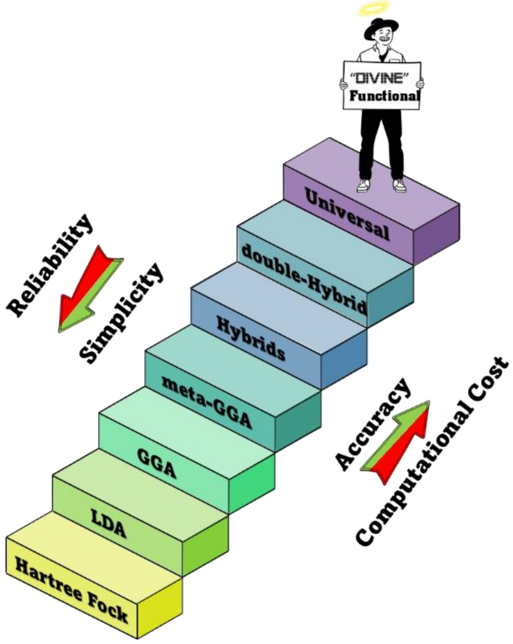

Figure 2.1. Jacob's ladder of functional improvements. Climbing up the ladder accuracy and computational costs increases.

to experiment but containing parameters derived from mathematical constraints. The PBE functional has been modified several times in order to improve its performance for some systems (*e.g.*, PBEsol[15] for solids or RPBE[16] for adsorption of small molecules on metallic surfaces).

The next step of the ladder belongs to the Meta-Generalized Gradient Approximation (meta-GGA), an extension of GGA, introducing the Laplacian of the density in addition to the density and its gradient. However, these functionals do not improve to a large extent the accuracy with respect the description of extended transition metal systems. Some proposed forms are the Tao-Perdew-Staroverov-Scuseria (TPSS)[17] or the Perdew-Kurth-Zupan-Blaha (PKZB).[18]

Finally, hybrid functionals are on the last step and are based on a mix of the explicit form of non-local HF and DFT exchange. Usually, these hybrid functionals have been parametrized with experimental properties data and, in general, the description of molecular systems is improved but that of delocalised systems such as metals[19,20] are less accurate.

The calculations reported in this Thesis have been carried out using a GGA approach based on the PBE exchange correlation functional. This functional has been proven to be suitable to describe the properties of bulk, surface transition metals,[21-23] and more importantly MXenes.[24-26] All these calculations have been carried out using as non-polarized configurations.

2.2.4 Plane-wave basis

In all electronic structure methods, the electron density is described by a basis set that is used to represents the one electron wave functions or orbitals. One type of basis sets, especially well-suited for the treatment of periodic systems, is the one employing plane-waves (PW). These are implemented in the code employed on this Doctoral Thesis, Vienna Ab Initio Simulation Program (VASP).[27-29]

As said, plane wave functions are commonly used in calculation of periodic systems and their general form is

$$PW = e^{i\boldsymbol{kr}} \tag{2.16}$$

where ***k*** is the plane wave vector and ***r*** the position one. Even though their use is advantageous, both for their periodicity properties and affordable computational cost, a large number of plane waves is needed to describe all the system electrons accurately. To solve this inconvenience, the number of electrons selected to be represented by the plane waves may reduce, thus decreasing the computational cost but without losing accuracy thanks to the use of pseudopotentials. This is possible because electron in a given atom can be separated into core electrons, those not involved in processes of breaking/making bonds, and valence electrons responsible for the chemistry. Thus, the core electrons can freeze at their atomic form during calculations or the effect of the corresponding density into the valence density of a systems represented by pseudopotentials or effective core potentials.

There are different types of pseudopotentials, being the ultrasoft potentials,[30] norm-conserving pseudopotentials[31] and, the projected augmented wave (PAW) potentials,[32] those mostly employed in calculations for periodic systems. The calculations reported in this Thesis have been carried out with the PAW pseudopotentials which are proven to provide accurate results for a broad range of systems.

2.3 Periodic solids

Crystalline solids are described as an ordered periodic structure of atoms. The periodic symmetry allows to reproduce the totality of the solid from a translational repetition of a given motif, known as unit cell, in the three-dimensional space. The unit cell is forming the atomic base containing a certain number of atoms and the periodic symmetry depends on how this is replicated in space. As a consequence, to approximately solve the Schrödinger equation for the atoms in the unit cell, the electron density or wavefunction must remain invariant when applying a translational operator ($\hat{T}$) defined by the three orthogonal vectors of the crystalline lattice

$$\hat{T} = n_1 a + n_2 b + n_3 c \tag{2.17},$$

describing an infinite array of discrete points called the Bravais lattice. The irreducible unit cell that can describe a periodic solid is the primitive cell.

The most common unit cells encountered in many materials are body-centered cubic (*bcc*), face-centered cubic (*fcc*) and, hexagonal closed packed (*hcp*). *fcc and hcp* have the same packing efficiency, being the highest of all possible structures, although these structures differ in the stacking (ABA for *fcc* and ABC for *hcp*). The most used structure in this Thesis is the *hcp*, a feature of the MXene structure.[33]

2.3.1 Reciprocal space

To properly describe the atomic and electronic structure of periodic systems, it is necessary to introduce and make use of the reciprocal space. This, is a mathematical construction related to the real space, defined by the unit cell vectors of Eq. (2.17), $\boldsymbol{a}$, $\boldsymbol{b}$ and $\boldsymbol{c}$, in their translated form, $\boldsymbol{a'}$, $\boldsymbol{b'}$ and $\boldsymbol{c'}$ that satisfies:

$$\boldsymbol{a}' = 2\pi \frac{\boldsymbol{b} \times \boldsymbol{c}}{\boldsymbol{a} \cdot (\boldsymbol{b} \times \boldsymbol{c})};\ \boldsymbol{b}' = 2\pi \frac{\boldsymbol{a} \times \boldsymbol{c}}{\boldsymbol{b} \cdot (\boldsymbol{a} \times \boldsymbol{c})};\boldsymbol{c}' = 2\pi \frac{\boldsymbol{a} \times \boldsymbol{b}}{\boldsymbol{c} \cdot (\boldsymbol{a} \times \boldsymbol{b})} \quad (2.18).$$

Hence, the vectors on the reciprocal space can be presented as

$$\boldsymbol{D} = m_1\boldsymbol{a}' + m_2\boldsymbol{b}' + m_3\boldsymbol{c}' \quad (2.19)$$

being m_i integers. Further, the description of the real unit cell can be done with the corresponding unit cell in the reciprocal space. This is called Wigner Seitz cell or first Brillouin zone which volume is equal to $(2\pi)^3/V_c$, being V_c the volume of the real space. Therefore, the volumes of direct and reciprocal unit cells are inversely proportional, meaning that the larger the real unit cell, the smaller in the reciprocal lattice.

Thus, in a periodic system where the one electron wavefunctions can be described as a combination of plane waves with vectors which are reciprocal to those of the direct lattice, the use of the reciprocal lattice has advantages as discussed in 2.3.2.

2.3.2 Bloch's theorem

Bloch's theorem[34] shows that it is possible to use the reciprocal space and plane waves to describe the periodic system. This theorem states that the values of all observables of the unit cell are equal for the Bravais lattice equivalent positions. Therefore, the potential in a given position of the unit cell, *r*, remains equal in an equivalent position in a replicated cell, *r* + R, obtained by the translational operator in Eq. (2.17)

$$V(\vec{r}) = V(\vec{r} + \vec{R}) \tag{2.20}$$

Satisfying Eq. (2.20) for a periodic system, the electronic wave functions can be expressed as

$$\Psi_i(\vec{r}) = e^{i\boldsymbol{kr}} \upsilon_i(\vec{r}) \tag{2.21}$$

where $e^{i\boldsymbol{kr}}$ is a plane wave and $\upsilon_i(\vec{r})$ a periodic function for the Bravais lattice that can be expressed as

$$\upsilon_i(\vec{r}) = \sum_{\boldsymbol{D}} C_{i,\boldsymbol{D}} e^{i\boldsymbol{Dr}} \tag{2.22}$$

where ***D*** is the reciprocal vector of Eq. (2.19). Combining Eq. (2.21) and Eq. (2.22)

$$\Psi_i(\vec{r}) = \sum_D C_{i,k+\boldsymbol{D}} e^{i(k+\boldsymbol{D})\boldsymbol{r}} \qquad (2.23).$$

Each plane wave of this linear combination is characterized by a kinetic energy, $\frac{|k+D|^2 h}{2m}$. Therefore, the plane wave set can be defined by the kinetic energy, varying thus the number of plane waves and with this, the description of the observables of the system.

2.4 Extended Surfaces

A given periodic system can be represented as a packing of atomic planes and cleaving the material at one of these planes leads to well defined surface. Crystal planes and the corresponding surfaces can be described by Miller indices as described below.

2.4.1 Miller indices

Miller indices are used to name the combination of three non-colinear points of the Bravais lattice or planes. These indices are defined by the inverse of three points, *x*, *y* and *z*, which are the intersection between this defined plane and the coordinate axis. Then these indices are multiplied by the least common multiple.

$$h = \frac{1}{x}\ ; k = \frac{1}{y} ; l = \frac{1}{z} \tag{2.24}$$

For example, for $x = 3$, $y = 1$, and $z = 2$, h is 1/3, k is 1 and l is ½ and therefore, when multiplying by the least common multiple, the Miller indices are (263). It is important to note that if there is no intersection between the plane and the coordinate axis, the value of the Miller indices is 0. Figure 2.2 display the most common planes of the cubic Bravais lattice, (100), (110) and (111) as an example.

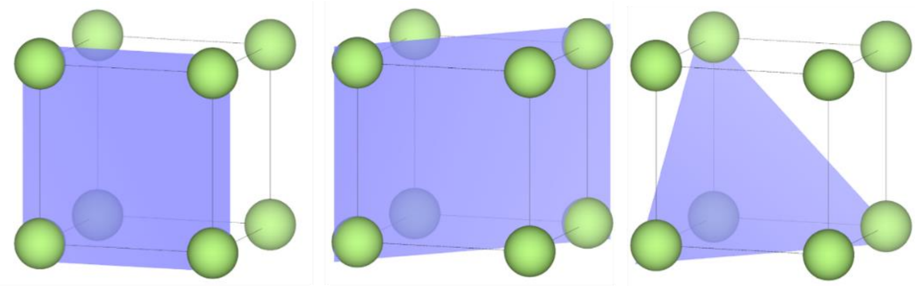

Figure 2.2. Miller indices planes of the Bravais lattice. From left to right, (100), (110), and (111).

2.4.2 Surface models

To theoretically study a solid surface, a model is needed. In the present Doctoral Thesis, we make use of the periodic slab model is used. Here, a slab is built from the bulk unit increasing the dimension of the plane of interest and adding a vacuum zone (≤10 Å), to avoid interactions between periodically repeated replicas. These slabs contain a large number of atomic layers to correctly describe the bulk material and surface properties. Usually, to carry out adsorption calculations, the bottom layers of the slab are fixed while the remain layers are allowed to relax. Thus, the bulk environment and the surface atoms are simulated. Figure 2.3 shows an example of slab cell.

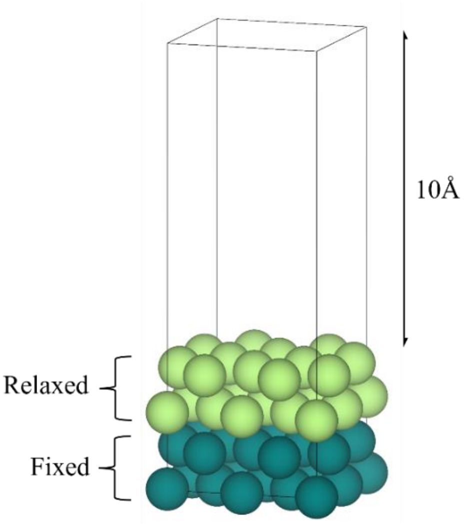

Figure 2.3. Representation of a four-layered face- centered cubic (100) slab cell with 10 Å of vacuum Dark spheres correspond to fixed layers.

2.5 Transition State Theory

In the study of the mechanisms of chemical reactions, the structures of reactants and products correspond to the optimized minima of the Potential Energy Surface (PES). However, the reactions proceed through an intermediate structure called the transition state, an activated complex formed from reactants which corresponds to a saddle point of the PES. Thus, for a reaction coordinate, their energy is maximum whilst for the rest, are minima. Additionally, this transition state must satisfy two conditions. First, the gradient of the energy with respect the coordinates of all atoms must be zero and second, the Hessian matrix must have one negative eigenvalue along the reaction coordinate which corresponds to the path between reactants to products. Both methods have been simultaneously used in the present Thesis to identify the transitions states of the Reverse Water Gas Shift (RWGS) catalysed by Mo_2C MXene as described in Chapter 6.

2.5.1 Climbing-Image Nudged elastic band method

Climbing-Image Nudged elastic band method (CI-NEB) is one of the proposed algorithms to find transition states.[35] Here, using the structures of reactants and products, I_0 and I_N, a set of images, (I_0, I_1, I_2, …, I_N), is generated. This set, connected by spring forces, is constrained by the same chain of springs linking them (Figure 2.4). Hence, the structures do not evolve towards a minimum and the structure with the highest energy shifts until finding the correct transition state. However, it is important to note this method requires a doble check regarding the path selected, due to the possibility of not being the lowest energy path.

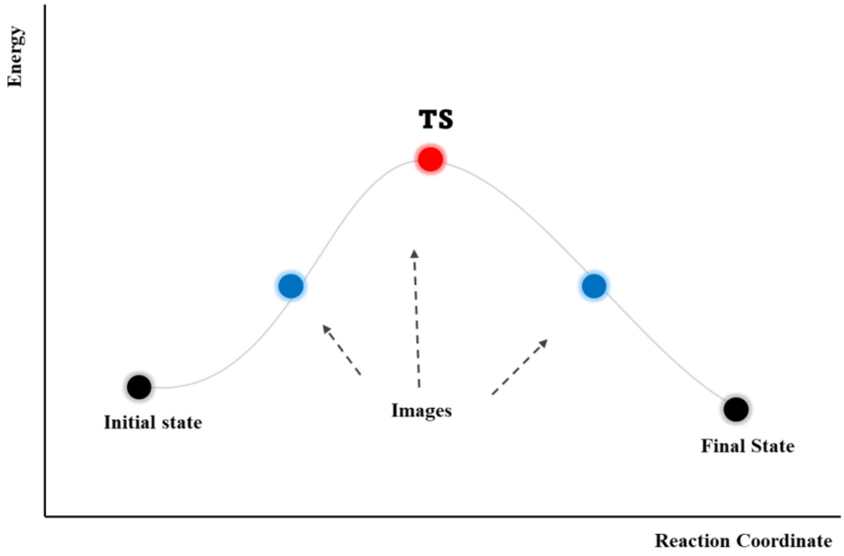

Figure 2.4. CI-NEB schematic representation. Black spheres represent the initial and final state, blue spheres the intermediate images and, red sphere, the found transition state.

2.5.2 The Dimer method

The Dimer method is the other algorithm proposed to find transition states.[36,37] Unlike the CI-NEB method, this methodology recalls to two images of the same system, practically the same, but displaced a fixed distance. From the initial state to the saddle point, the dimer moves through the PES rotating. This is to find the potential energy lowest curvature mode, which once found, the dimer follows its direction. In comparison with the CI-NEB, the Dimer methods requires less previous information and computational effort, given that is not needed the pathway of the reaction.

2.6 References

1. Born, M.; Oppenheimer, R. Zur Quanterntheorie Der Molekeln. *Ann. Phys*., **1927**, 84, 457-484.
2. Szabo, A.; Ostlund, N. S. *Modern Quantum Chemistry: Introduction to Advanced Electronic Structure Theory*; Courier Dover Publications, **1996**.
3. Foster, J. M.; Boys, S. F. Canonical Configurational Interaction Procedure. *Rev. Mod. Phys*. **1960** 32, 300.
4. Møller, C.; Plesset, M. S. Note on an Approximation Treatment for Many-Electron Systems. *Phys. Rev*., **1934**, 46, 618–622.
5. Parr, R. G. Density Functional Theory. *Annu. Rev. Phys. Chem*., **1983**, 34, 631.
6. Fermi, E. Statistical Method to Determine Some Properties of Atoms. *Rend. Accad. Naz. Lincei.*, **1927**, 6, 602.
7. Thomas, L. H. The Calculation of Atomic Fields. *Proc. Cambridge Phil. Soc.*, **1927**, 23, 542.
8. Hohenberg, P. C.; Kohn, W. Inhomogeneous Electron Gas. *Phys. Rev.*, **1964**, 136, 864-871.
9. Kohn, W.; Sham, L. J. Self-Consistent Equations Including Exchange and Correlation Effects. *Phys. Rev.*, **1965,** 140, A1133-A1136.
10. Perdew, J. P.; Schmidt, K. Jacob’s Ladder of Density Functional Approximations for the Exchange-Correlation Energy. *AIP Con. Proc.*, **2001**, 577, 1–20.
11. Vosko, S. H.; Wilk, L.; Nusair, M. Accurate Spin-Dependent Electron Liquid Correlation Energies for Local Spin Density

Calculations: A Critical Analysis. *Can. J. Phys.*, **1980,** 58, 1200–1211.

12. Ceperley, D. M.; Alder, B. J. Ground State of the Electron Gas by a Stochastic Method. *Phys. Rev. Lett.*, **1980,** 45, 566–569.
13. Perdew, J. P.; Wang, Y. Accurate and Simple Analytic Representation of The Electron-Gas Correlation Energy. *Phys. Rev. B.* **1992**, 45, 13244–13249.
14. Perdew, J. P.; Burke, K.; Ernzerhof, M. Generalized Gradient Approximation Made Simple. *Phys. Rev. Lett.*, **1996**, 77, 3865–3868.
15. Perdew, J. P. et al. Restoring the Density-Gradient Expansion for Exchange in Solids and Surfaces. *Phys. Rev. Lett.*, **2008**, 100, 136406.
16. Hammer, B.; Hansen, L. B.; Nørskov, J. K. Improved Adsorption Energetics Within Density-Functional Theory Using Revised Perdew-Burke-Ernzerhof functionals. *Phys. Rev. B*, **1999**, 59, 7413–7421.
17. Tao, J.; Perdew, J. P.; Staroverov, V. N.; Scuseria, G. E. Climbing the Density Functional Ladder: Nonempirical Meta–Generalized Gradient Approximation Designed for Molecules and Solids. *Phys.Rev. Lett.*, **2003**, 91, 14640.
18. Perdew, J.; Kurth, S.; Zupan, A.; Blaha, P. Accurate Density Functional with Correct Formal Properties: A Step Beyond the Generalized Gradient Approximation. *Phys. Rev. Let*. **1999**, 82, 2544–2547.
19. Janthon, P.; Luo, S. A.; Koslov, S.; Viñes, F.; Limtrakul, J.; Truhlar, D. G.; Illas, F. Bulk Properties of Transition Metals: A Challenge for

the Design of Universal Density Functionals. *J. Chem. Theory Comput.,* **2014**, 10, 3832–3839.

20. Perdew, J. P., Ernzerhof, M.; Burke, K. Rationale for mixing exact exchange with density functional approximations. *Chem. Phys*. **1996**, 105, 9982–9985.
21. Janthon, P.; Kozlov, S. M.; Viñes, F.; Limtrakul, J.; Illas, F. Establishing the Accuracy of Broadly Used Density Functionals in Describing Bulk Properties of Transition Metals. *J. Chem. Theory Comput*. **2013**, 9, 1631– 1640.
22. Vega, L.; Ruvireta, J.; Viñes, F.; Illas, F. Jacob’s Ladder as Sketched by Escher: Assessing the Performance of Broadly Used Density Functionals on Transition Metal Surface Properties. *J. Chem. Theory Comput*. **2018**, 14, 395– 403.
23. Vega, L.; Viñes, F. Generalized Gradient Approximation Adjusted to Transition Metals Properties: Key Roles of Exchange and Local Spin Density. *J. Comput. Chem.* **2020**, 41, 2598– 2603.
24. Morales-García, Á.; Fernández-Fernández, A.; Viñes, F.; Illas, F. CO2 Abatement Using Two-Dimensional MXenes Carbides. *J. Mater. Chem. A* **2018**, 6, 3381– 3385.
25. Morales-Salvador, R.; Morales-García, Á.; Viñes, F.; Illas, F. Two-Dimensional Nitrides as Highly Potential Candidates for CO2 Capture and Activation. *Phys. Chem. Chem. Phys*. **2018**, 20, 17117–17124.
26. Morales-García, Á.; Mayans, M.; Viñes, F.; Illas, F. Thickness Biased Capture of CO2 on Carbide MXenes. *Phys. Chem. Chem. Phys*. **2019**, 21, 23136– 23142.

27. Kresse, G.; Furthmüller, J. Efficiency of Ab-Initio Total Energy Calculations for Metals and Semiconductors Using a Plane-Wave Basis Set. *Comput. Mater. Sci*. **1996,** 6, 15–50.
28. Kresse, G. Efficient Iterative Schemes for Ab Initio Total-Energy Calculations Using a Plane-Wave Basis Set. *Phys. Rev. B.*, **1996**, 54, 11169–11186.
29. Kresse, G.; Hafner, J. Ab Initio Molecular Dynamics for Liquid Metals. *Phys. Rev. B.,* **1993**, 47, 558–561.
30. Vanderbilt, D. Soft Self-Consistent Pseudopotentials in a Generalized Eigenvalue Formalism. *Phys. Rev. B.,* **1990**, 41, 7892–7895.
31. Hamann, D. R.; Schlüter, M.; Chiang, C. Norm-Conserving Pseudopotentials. *Phys. Rev. Lett*., **1979**, 43, 1494–1497.
32. Blöchl, P. E. Projector Augmented-Wave Method. *Phys. Rev. B*., **1994**, 50, 17953–17979.
33. Anasori, B.; Lukatskaya, M.; Gogotsi, Y. 2D Metal Carbides and Nitrides (MXenes) For Energy Storage. *Nat Rev Mater,* **2017**, 2, 16098.
34. Bloch, F. Bemerkung Zur Elektronentheorie Des Ferromagnetismus Und Der Elektrischen Leitfähigkeit. *Z. Phys*., **1929**, 57, 545-555.
35. Henkelman, G.; Uberuaga, B. P.; Jónsson, H. A. Climbing Image Nudged Elastic Band Method for Finding Saddle Points and Minimum Energy Paths. *J. Chem. Phys*., **2000**, 113, 9901.
36. Henkelman, G.; Jónsson, H. A Dimer Method for Finding Saddle Points on High Dimensional Potential Surfaces Using Only First Derivatives. *J. Chem. Phys*., **1999**, 111, 7010.

37. Olsen, R. A.; Kroes, G. J.; Henkelman, G.; Arnaldsson, A.; Jónsson, H. Comparison of Methods for Finding Saddle Points Without Knowledge of the Final States. *J. Chem. Phys.*, **2004**, 121, 9776–9792.

CHAPTER THREE

Multiscale Approaches

Chapter 3

The present chapter is focused on the multiscale approaches carried out on this Doctoral Thesis. Firstly, a description of the Kinetic Phase Diagrams is presented, followed by the Microkinetic Modelling employed to describe the Reverse Water Gas Shift reaction as shown on Chapter 6. These methods represent a practical approach to estimate the performance of a reaction promoting reliable results from computational inputs.

3.1 Kinetic Phase Diagrams

The framework of the transition state theory (TST)[1,2] is employed to build the kinetic phase diagrams through the analysis of adsorption and desorption rates. This allows us to access to temperature and pressure conditions when both rates are equal, stablishing regions of activation and deactivation of those molecules susceptible to interact with substrates. The construction of these phase diagrams requires the analysis of the potential energy surface exploring the activation of CO_2 where the adsorption energy is the main descriptor.

3.1.1 Adsorption energy and Zero Point Energy

The adsorption energy (E_{ads}) is defined as the delivered energy when molecules or single atoms are chemically adsorbed on one particular surface,[3] as the MXene surfaces. This energy is achieved as follows,

$$E_{ads} = E_{system} - (E_{substrate} + E_{adsorbate}) \tag{3.1}$$

In Eq. (3.1), E_{system} corresponds to the total energy of the system containing the slab model representing the surface and the specie (molecule or single atom) anchored; the $E_{substrate}$ term stands for the energy of the pristine surface model and, $E_{adsorbate}$ is the energy of molecule or single atom in its gas phase configuration. According to this definition the adsorption is exothermic or energetically favorable when $E_{ads} < 0$. Precise E_{ads} requires the inclusion of the contribution of the zero-point energy (ZPE) term. This term considers the contribution of the vibrations at 0 K of the molecule in its adsorbed and isolated configurations. The ZPE energy is described as follows:

$$ZPE = \frac{1}{2}\sum_i h\nu_i \tag{3.2}$$

where h is the Planck constants and ν_i stands for the vibrational frequencies of species. Based on Eq. (3.2), one can define the ΔZPE term as the difference between the ZPE contribution of an adsorbed and gas phase species.

$$\Delta ZPE = ZPE_{ads} - ZPE_{gas\,phase} \tag{3.3}$$

We note that all energies of the present document are systematically corrected with the ΔZPE term as defined in Eq. (3.3).

3.1.2 Kinetic rate constant

To obtain the kinetic rates, the TST approach is used. The Eyring, Evans and, Polanyi equation[4,5] defines the rate for a unimolecular elementary reaction described as

$$r = \frac{k_B \cdot T}{h}\frac{Q^{TS}}{Q}e^{-E_a/k_B \cdot T} \tag{3.4}$$

here, Q^{TS} and Q are the partition functions of the transition state (TS) and the initial state, respectively. The E_a term corresponds to the activation energy, h and k_B are the Planck and Boltzmann constants and, T is the temperature. The kinetic rate of adsorption, r_{ads}, is defined by the Hertz-Knudsen[6,7] equation as follows,

$$r_{ads} = \frac{S_0 \cdot\ p_X \cdot A}{\sqrt{2 \cdot \pi \cdot m \cdot k_B \cdot T}} \tag{3.5}$$

where S_0 is the sticking coefficient, p_X stands for the partial pressure of the molecule *x* adsorbed on the surface, A corresponds to the area of an active adsorption site, *m* relates to the mass of the molecule adsorbed on the studied surface, k_B is the Boltzmann constant and finally, T recalls for the temperature.

On the other hand, the desorption rate r_{des}, also estimated from the TST, assumes the transition state for the desorption process close enough to the final state and thus, with the desorption energy, the energy barrier can be estimated as

$$r_{des} = \nu_{des} \cdot exp\left(\frac{E_{ads}}{k_B.T}\right) \quad ; \quad \nu_{des} = \frac{k_B.T \cdot q^{gas}_{trans,2D} \cdot q^{gas}_{rot} \cdot q^{gas}_{vib}}{q^{ads}_{vib}} \tag{3.6}$$

where ν_{des} englobes the partition function of the molecule in a 2D transition state, E_{ads} is the adsorption energy presented in Eq. (3.1) and k_B is the Boltzmann constant and T is the temperature.

Thus, the rotational, translational, and vibrational partition function are needed. Rotational partition function can be calculated as

$$q_{rot} = \frac{8\pi^2 I k_B T}{h^2} \tag{3.7}$$

where I is the rotational moment of inertia in the three directions, k_B is the Boltzmann constant, T is the temperature and h, the Planck constant. Regarding the translational moment of inertia, it can be calculated as

$$q_{trans} = \frac{L\sqrt{2\pi m k_B T}}{h} \tag{3.8}$$

where L is the length of the translation and m, the mass of the particle. Last, the vibrational partition function can be calculated using the frequencies of the vibration modes, ω, with the following equation

$$q_{vib} = \frac{1}{1 - \exp\left(-\frac{h\omega}{k_B T}\right)} \tag{3.9}$$.

Combining Eqs. (3.6), (3.7), (3.8) and (3.9), the desorption rate results in

$$r_{des} = \frac{k_B \cdot T^3}{h^3} \frac{A2\pi m k_B T}{\sigma \Theta_{rot}} e^{-\Delta E_{des}/_{k_B \cdot T}} \tag{3.10}$$

where σ is the symmetry number of the molecule and Θ_{rot} the characteristic temperature of rotation.

To analyse the crossover between the adsorption and desorption of the system anchored on the substrate, the rates have to be equal at a certain condition of pressure and temperature,

$$r_{ads} = r_{des} \tag{3.11}$$

as a dynamic equilibrium defined by a partial pressure of the molecule (p_X) and temperature. As it, a set of pressure and temperature are obtained, the needed inputs to build the kinetic phase diagram, as shown in Figure 3.1. Selecting a grid of temperatures and pressures allows one plotting the kinetic phase diagrams shown Figure 3.2.

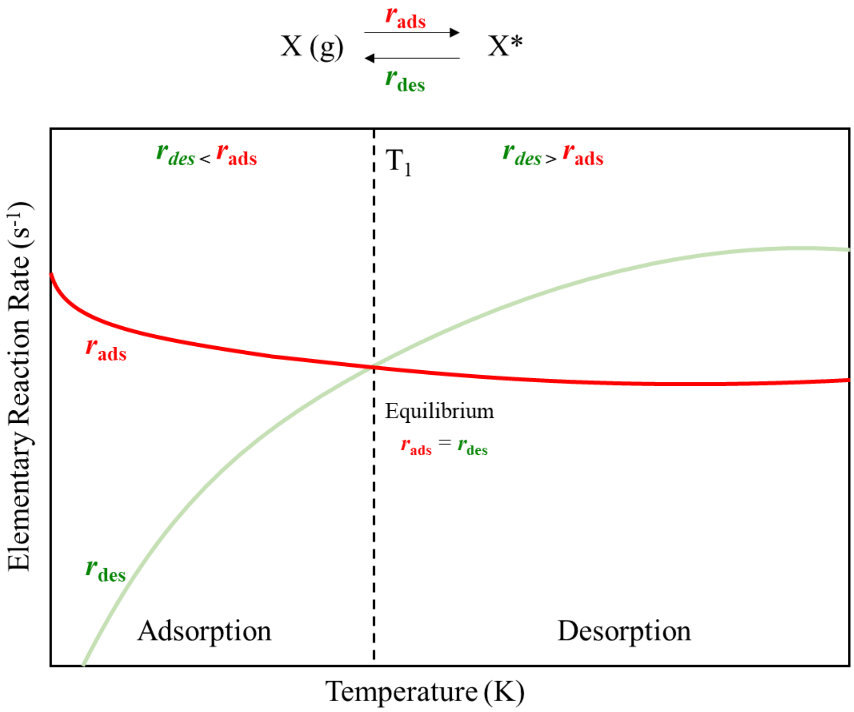

Figure 3.1. Illustration of the evolution of adsorption and desorption rates with the temperature. The temperature at which r_{ads}=r_{des} corresponds to a certain pressure.

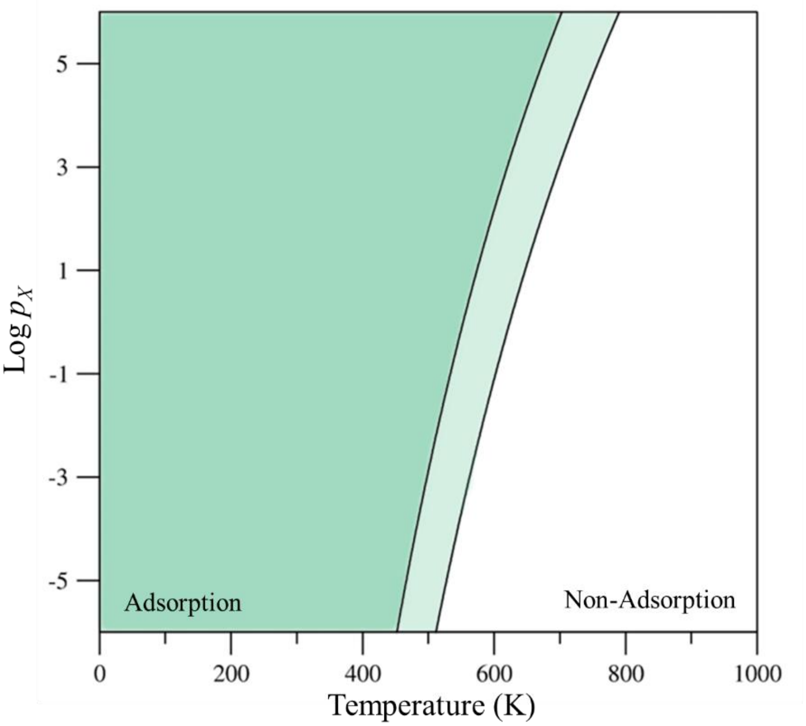

Figure 3.2. Example for Kinetic Phase Diagram for adsorption/desorption of a certain molecule on a surface. The color scheme denotes the three possible scenarios present: Adsorption of the molecule in dark green, an intermediate situation in light green and, non-adsorption in white.

3.2 Microkinetic modelling

The microkinetic analysis of a reaction is a technique used to predict the result of complex chemical reactions under different conditions and is performed on a multi-step model, encompassing the different routes available for the reaction. Thus, these simulations allow the identification of critical properties for catalyst design[8] such as reaction kinetic data for reactor design from a computational viewpoint. Exploiting DFT calculations and through the TST formalism described earlier, these results can be used to compute several parameters required to perform the microkinetic analysis. These include the initial energy of the system, the energy of the transition states of the elementary reaction steps explored, the final state energy of these elementary steps, electronic activation energies (E_a) in both backward and forward directions and kinetic constants. Note that the E_a is obtained as follows

$$E_a = E^{TS} - E^{Initial/Final\ State} \qquad (3.12).$$

It is important to distinguish the type of the elementary reaction. For example, a bimolecular catalytic reaction composed by two reagents (A and B) and one product (C) performing the reaction, $2A + B_2 \rightarrow 2C$ present the following elementary reaction steps:

$\mathrm{A} + * \rightleftarrows \mathrm{A}^*$	Adsorption
$\mathrm{B_2} + 2^* \rightleftarrows \mathrm{B}^*$	Adsorption
$\mathrm{A}^* + \mathrm{B}^* \rightleftarrows \mathrm{C}^* + *$	Surface Reaction
$\mathrm{C}^* \rightleftarrows \mathrm{C} + *$	Desorption

Figure 3. Example for bimolecular reaction. A, B and C, denotes gas phase molecules.

To compute the rate constants, the Eyring Eq. (3.4) is used for the surface reaction. For adsorption and desorption elementary steps, the *Hertz-Knudsen* Eqs. (3.5) and (3.10) are employed, and thus, kinetic constants can be obtained. Note that the equations used (Eq. (3.4), Eq. (3.6) and, Eq. (3.10)) are the same as presented in section 3.1.

Using these parameters, and through the evaluation between two selected temperatures and a chosen time, a set of data is obtained regarding the performance of the evaluated reaction. Variation of the surface coverage, production rates, or turn over frequency (TOF), which is the measure of the instantaneous efficiency of a catalyst or their performance in catalysis, are some results of the simulation.

To obtain these parameters, a set of ordinary differential equations (ODEs) must be resolved. For every elementary reaction step, there are two elementary reaction equations (2E) present one forward and one backward. Thus, using the equation

$$\frac{\partial \theta_j}{\partial t} = \sum_{i}^{2E} \left(\nu_{i,j} k_i \prod_{q}^{N_j} \theta_{q,i}^{\nu_{q,i}} \right) \tag{3.13}$$

where θ_j is the superficial concentration of the species j, $\nu_{i,j}$ the stoichiometric coefficient for the elementary step reaction i, k_i belongs to the rate constant for the reaction i, and $\theta_{q,i}$ and $\nu_{q,i}$ are the concentration and the stoichiometric coefficient of q in the reaction i, how the concentration of the compound varies respect time is obtained. For the example presented in Figure 3.3, the equations are

$$\frac{\partial \theta_A}{\partial t} = k_{1,ads}\theta_* - k_{1,des}\theta_A - k_{3,f}\theta_A\theta_B + k_{3,b}\theta_C\theta_*$$

$$\frac{\partial \theta_B}{\partial t} = 2k_{2,ads}\theta_*^2 - 2k_{2,des}\theta_B^2 - k_{3,f}\theta_A\theta_B + k_{3,b}\theta_C\theta_* \tag{3.14}$$

$$\frac{\partial \theta_C}{\partial t} = k_{4,ads}\theta_* - k_{4,des}\theta_C + k_{3,f}\theta_A\theta_B - k_{3,b}\theta_C\theta_*$$

$$\frac{\partial \theta_*}{\partial t} = -k_{1,ads}\theta_* + k_{1,des}\theta_A - 2k_{2,ads}\theta_*^2 + 2k_{2,des}\theta_B^2 + k_{3,f}\theta_A\theta_B - k_{3,b}\theta_C\theta_* - k_{4,ads}\theta_* + k_{4,des}\theta_C$$

and when solved, the solution is presented by the steady state

$$\left\{\frac{\partial \theta_j}{\partial t} = 0\right\}, \text{for all } j \tag{3.15}$$

Here , k_b and k_f stands for backward and forward reaction rates.

It is important to note that to calculate the first derivatives with respect time some parameters must be added to settle the boundary conditions of the system. These include adsorption area, molecular mass, rotational temperature and adsorption energy, among others.

Thus, an example of variation of the surface coverage as a function of temperature is presented hereunder. Here, increasing the temperature, the coverage of A* decreases and B* increases, obtaining henceforth, C*. Heating the reaction. B* and C* decreases and *, the free sites, increases. This means that a low temperature the surface is full covered in A* and not enough of B* and therefore, the reaction cannot take place. With higher temperature, A* decreases the coverage and the reaction go forward. Finally, when the reaction is completed, C* desorbs, and the surface becomes pristine.

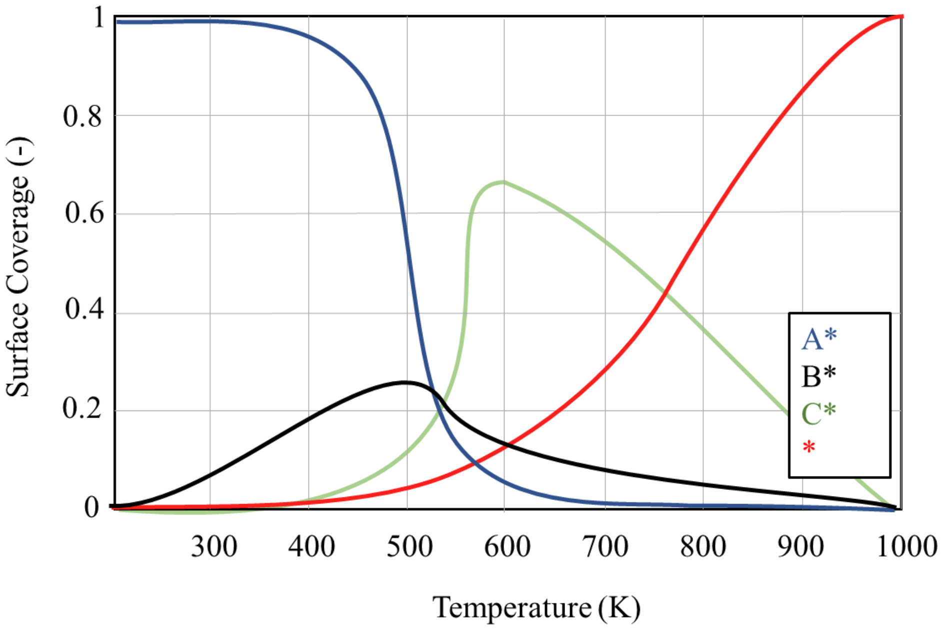

Figure 3.3. Example of surface coverage as a function of temperature. Increasing the temperature, the coverage of A*, in blue, decreases and the free sites, in red, increases. Coverage for B* and C* increases and decreases meaning that the reaction is done and C* has been desorbed.

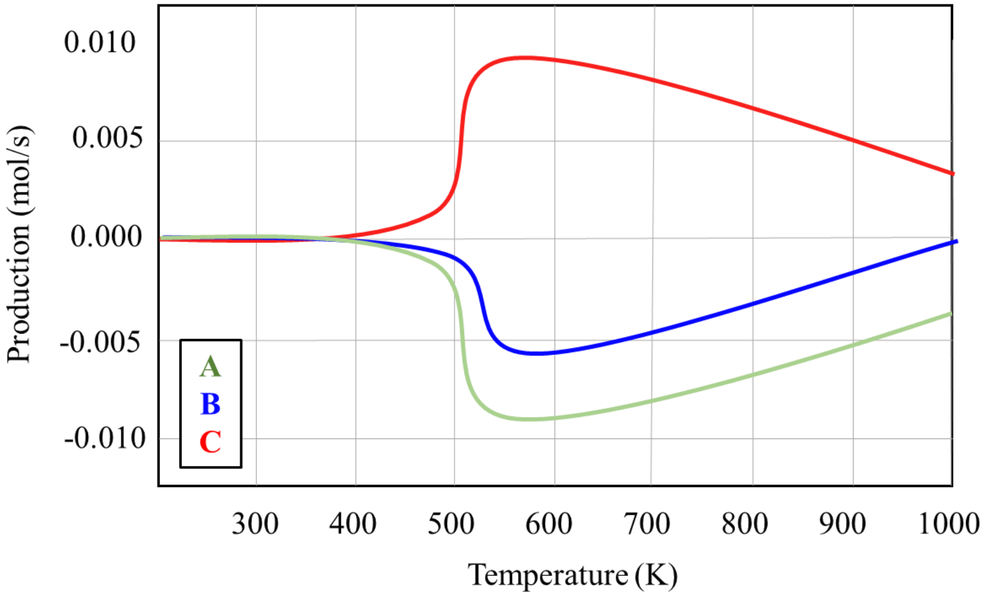

Figure 3.4. Example of production rate of C, red, as a function of temperature. Blue and green represents the consumption rates of A and B.

Figure 3.4 shows an example for the simulation of the reaction rates for the $2A + B_2 \rightarrow 2C$ reaction. Here, the production rate of C is the same as the rate of consumption of A and the rate of B, is approximately half of B, according to the stoichiometry of the reaction. It is important to note that the production and TOF on these simulations are equivalent.

However, a more complex analysis can be done. Exploiting the possibility of performing infinite microkinetic analysis, a three-variable plot called heating map, pressure vs. temperature vs. production or TOF presents an easy way to identify the optimal conditions of pressure and temperature where the reaction has the best production. Figure 3.5 shows an example of this heatmap. Green areas present lower TOFs than the yellow ones, meaning that to obtain the better production for the reaction, one has to increase the temperature and pressure conditions of the system.

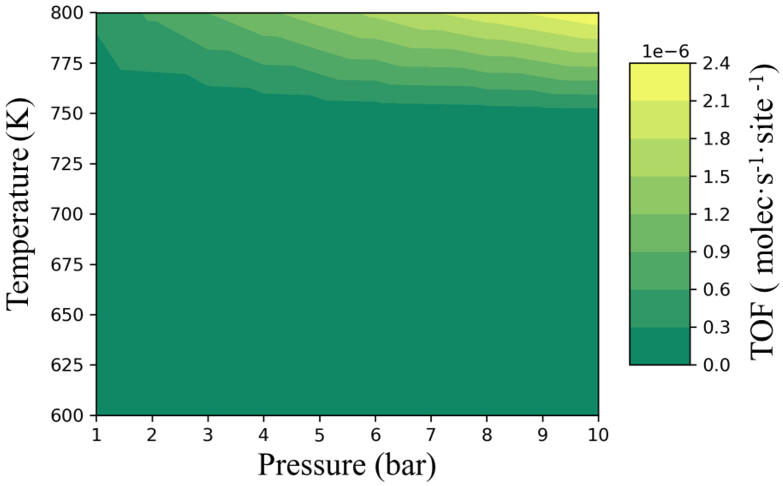

Figure 3.5. Example of a heatmap of TOF under different T and *p* conditions for the studied reaction. Units for pressure, temperature, and TOF are bar, K, and molecules·site^{-1}·s^{-1}.

3.3 References

1. Truhlar, D. G.; Garrett, B. C.; Klippenstein, S. J. Current Status of Transition-State Theory. *J. Phys. Chem.* **1996**, 100, 31, 12771-12800.
2. Barons, P. Transition State Theory in Reaction Rate Theory and Rare Events. Elseiver, 2017, pp.227-271. DOI:10.1016/B978-0-44-456349-1.00010-6.
3. Sorescu, D. C.; Thompson, D. L.; Hurley, M. M.; Chabalowski, C. F. First Principles Calculations of The Adsorption, Diffusion, and Dissociation of a CO Molecule on the Fe (100) Surface. *Phys. Rev. B,* **2002,** 66, 035416.
4. Evans, M.G.; Polanyi M. Some applications of the transition state method to the calculation of reaction velocities, especially in solution. *Trans. Faraday Soc*.**,** **1935**, 31, 875–894.
5. Eyring, H.; Polanyi, M. On Simple Gas Reactions. *Z Phys Chem*., **2013,** 227, 1221–1246.
6. Hertz, H. Ueber den Druck des gesättigten Quecksilberdämpfes. *Ann. Phys*., **1882**, 17.
7. Knudsen, M. Experimentelle Bestimmung des Druckes gesättigter Quecksilberdämpfe bei O und Höheren Temperaturen . *Ann. Phys*, **1909,** 29.
8. Motagamwala, A. H.; Dumesic, J. A. Microkinetic Modelling: A Tool for Rational Catalyst Design. *Chem. Rev.*, **2021**, 121, 1049-1076.

CHAPTER FOUR

Carbon Dioxide Adsorption and Activation on Nitride MXenes

Chapter 4

4.1 Introduction

MXenes are potential materials for CCU and CCS due to the exposed surface area, great stability and versatile composition and the fact that are able to capture and activate CO_2 under certain conditions through a charge transfer from the MXene surface towards the molecule. Thus, a large series of carbon-based MXene compounds, such as functionalized MXenes[1-3], MXene composites[4] and MXenes with vacancies,[5] have been investigated with promising results. Given that transition metal nitrides have been proven to share properties with their carbon homologous, the resemble showed by nitrogen based MXenes present an appealing alternative for these carbon capture purposes and thus, the motivation of this study is to investigate the CO_2 adsorption on bare nitride MXenes.[6]

The adsorption of CO_2 molecule is carried out through periodic density functional based calculations on the nine early transition metal nitrides, including different thickness (three, five, and seven layers). The adsorption and desorption rates labelled as r_{ads} and r_{des} are calculated through the Hertz-Knudsen equation and TST.[7,8] This allows us accessing to the kinetic phase diagrams to quantify the crossover between CCS and non-CCS.

4.2 Main Results

To study the adsorption trends of the CO_2 molecule on the nitride MXenes , the analysis of the variation of the CO_2 adsorption energy with respect to the composition and thickness is performed. First, the most favorable adsorption sites are found, being these similar to the conformations present on the M-terminated TMC (111). Regarding the TMC(001) surface, conformations that present the CO_2 molecule are different to the TMC(111).

Thus, results show that MXene, report highly exothermic adsorptions, being the d^2-(Ti, Zr and, Hf) the ones that exhibits the stronger adsorptions, followed by the d^3-(V, Nb and, Ta) and d^4-(Cr, Mo and, W), see Figure 4.1. Thus, MXene with M_3N_2 stoichiometry display larger values than their M_2N counterparts, being the most differentiable case the d^2-metals, being their values above -3.5 eV.

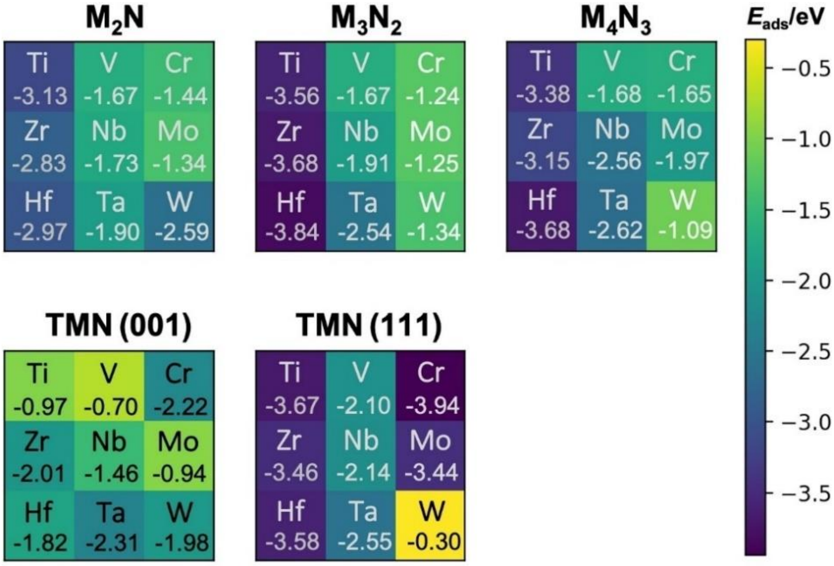

M_2N

Ti -3.13	V -1.67	Cr -1.44
Zr -2.83	Nb -1.73	Mo -1.34
Hf -2.97	Ta -1.90	W -2.59

M_3N_2

Ti -3.56	V -1.67	Cr -1.24
Zr -3.68	Nb -1.91	Mo -1.25
Hf -3.84	Ta -2.54	W -1.34

M_4N_3

Ti -3.38	V -1.68	Cr -1.65
Zr -3.15	Nb -2.56	Mo -1.97
Hf -3.68	Ta -2.62	W -1.09

TMN (001)

Ti -0.97	V -0.70	Cr -2.22
Zr -2.01	Nb -1.46	Mo -0.94
Hf -1.82	Ta -2.31	W -1.98

TMN (111)

Ti -3.67	V -2.10	Cr -3.94
Zr -3.46	Nb -2.14	Mo -3.44
Hf -3.58	Ta -2.55	W -0.30

Figure 4.1. CO_2 adsorption energies, Eads, on MXene and TMN surfaces. Colors indicates the interaction strength between CO_2 and the substrates, given in eV. Yellow corresponds to the weakest and dark blue the largest interaction. Values below the label of atoms correspond to the most favorable adsorption energies on the corresponding substrate.

However, analysing each metal individually, one can see that increasing the thickness of the MXene, the CO_2-philicity highly increases in the Nb- and Ti-MXenes, slightly Ti-, Zr-, Hf- and Mo-MXenes and W-nitride MXenes follows a totally opposite trend: increasing the thickness, the CO_2-philicity decreases.

Regarding the TMN (001) and TMC(111), results show that TMC (111) exhibits the expected values, being more active than the TMC(001) by far and behaving like their MXene counterparts. Note that the TMC CrN, MoN and WN present some superficial deformations on the presence of CO_2.

Being the adsorption energy of the MXene (0001) accompanied by an appreciable charge transfer from the surface to the CO_2 molecule, the topological Bader Charge is computed to explore whether this charge transfer is coupled to an adsorption energy with an activation of the CO_2. Here, the vast majority of substrates show values on the -2.5 to -1.0 eV and -1.75 to -0.9 eV range, performing observable trends without a quantitative relationship. Thus, TMC(111) show similar trends that the MXene (0001) surface given the structural resemblance. By contrast, TMC(001) show no clear trend except that small Q values are coupled with small $E_{ads,}$ being expected with the low reactivity of TMC(001).

Finalizing the adsorption trends block, the comparison between the E_{ads} of nitrides and carbides is performed. Results show that M_2N and M_4N_3 MXenes feature a lower CO_2-philicity than their carbide counterparts and M_3N_2 MXenes performs the opposite showing a larger affinity for the CO_2 molecule than their carbide counterpart M_3C_2.

Kinetic phase diagrams show the pressure/temperature regions where the CO_2 molecule adsorption or desorption prevails. Thus, these diagrams perform a zone dominated by adsorption and relevant to CCS located at low temperatures, a transition zone where exhibit the competition of adsorption and desorption and finally the desorption dominated zone where CO_2 does not adsorb at all. These zones are orange, light orange and, white, respectively.

Here, Cr, Mo, and W-derived MXenes exhibit the most suitable pressure/temperature ranges to act as CO_2 collector given the feasible mild conditions and the affordable release by heating below 500 K. MXenes with the higher adsorption energies, Ti- and Hf-, although, exhibits the most suitable pressure/temperature ranges to act as a trap for the CO_2, being suitable for CCS purposes.

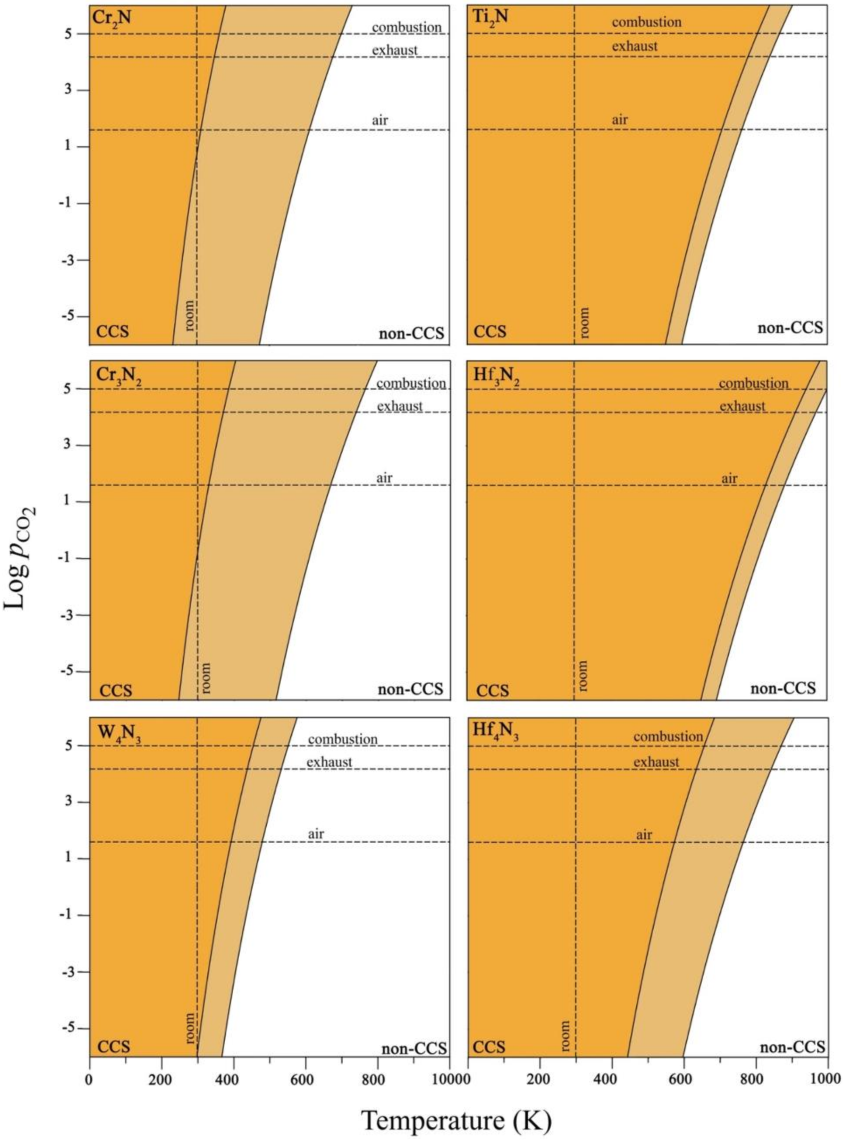

Figure 4.2. Kinetic phase diagrams for CO_2 adsorption/desorption on the (0001) MXene surfaces. The crossover among the dashed lines indicates the conditions of CO2 partial pressure (e. g. combustion:100 kPa, exhaust: 15 kPa, and air: 40 Pa,) and room temperature (300 K). Color defines three p scenarios CCS, non-CCS and an intermediate situation that are depicted with orange, white, and light orange, respectively.

4.3 Publication 1

Adsorption and Activation of CO_2 on Nitride MXenes: Composition, Temperature, and Pressure Effects

ChemPhysChem
Articles
doi.org/10.1002/cphc.202100600
Chemistry Europe
European Chemical Societies Publishing

Adsorption and Activation of CO_2 on Nitride MXenes: Composition, Temperature, and Pressure effects

Anabel Jurado,[a] Kevin Ibarra,[a] Ángel Morales-García,*[a] Francesc Viñes,[a] and Francesc Illas[a]

The interaction of CO_2 with nitride MXenes of different thickness is investigated using periodic density functional theory-based calculations and kinetic simulations carried out in the framework of transition state theory, the ultimate goal being predicting their possible use in Carbon Capture and Storage (CCS). We consider the basal (0001) surface plane of nitride MXenes with $M_{n+1}N_n$ ($n=1$–3; M=Ti, Zr, Hf, V, Nb, Ta, Cr, Mo, and W) stoichiometry and also compare to equivalent results for extended (001) and (111) surfaces of the bulk rock-salt transition metal nitride compounds. The present results show that the composition of MXenes has a marked influence on the CO_2-philicity of these substrates, whereas the thickness effect is, in general, small, but not negligible. The largest exothermic activation is predicted for Ti-, Hf-, and Zr-derived MXenes, making them feasible substrates for CO_2 trapping. From an applied point of view, Cr-, Mo-, and W-derived MXenes are especially well suited for CCS as the interaction with CO_2 is strong enough but molecular dissociation is not favored. Newly developed kinetic phase diagrams are introduced supporting that Cr-, Mo-, and W-derived MXenes are appropriate CCS substrates as they are predicted to exhibit easy capture at mild conditions and easy release by heating below 500 K.

1. Introduction

The increase of the carbon dioxide (CO_2) concentration in the Earth's atmosphere, mainly arising from burning fossil fuels for various applications,[1] is undoubtedly the responsible for the continuous global warming through the well-understood greenhouse effect.[2] This implies ocean acidification, polar ice caps and mountain glaciers melting, higher sea levels, and extreme weather events. These will all contribute to hamper the Earth's ability to support life and represents a serious challenge to the existing biodiversity.[3] Not surprisingly, the political agenda of many countries involve a roadmap to a low-carbon scenario that involves several strategies such as reducing emissions and eliminating emissions, among others as recently reviewed by Hepburn *et al.*[4] Regarding CO_2 sequestration, Carbon Capture and Storage (CCS) and the subsequent utilization (Carbon Capture and Usage – CCU) technologies are currently the focus of considerable research endeavors both from experiments[5] or tackled by computational modeling.[6] CCS is regarded as a necessary short-term bridge before CCU technologies mature, which needs to be improved for its efficiently implementation in a global scale. Apart from direct CO_2 sequestration through biomass or geological sinks,[4] considerable endeavors have been devoted at exploring novel materials for CO_2 abatement as well as to optimize the involved chemistry.[7] Amine-based solutions, ionic liquids, or solid adsorbents seem to be among the mature approaches, although with some environmental concerns due to their toxicity and other harmful issues. Other investigated materials include pure metals, metal oxides, graphene derived materials, zeolites, and Metal Organic Frameworks (MOFs).[8,9] In short, different strategies have been proposed for efficient CO_2 conversion.[6,10] However, the performance of many of these materials is far from optimum because of a low ability to adsorb, and eventually activate, CO_2, thus involving harsh conditions.

In the search for alternative substrates for CO_2 sequestration and activation, MXenes can step in because they have shown a sufficient strong way to adsorb CO_2.[11–16] This acronym, reminiscent of graphene, defines a new family of 2D materials that has rapidly grown since the isolation of $Ti_3C_2T_x$, the first member of the family, in 2011, *vide infra*.[17] This discovery generated a great expectation in several fields of applicability such as energy, catalysis, biomedics, electronics, and environmental applications, to name just a few.[18] All MXenes exhibit a $M_{n+1}X_nT_x$ general formula, where M is as early transition metal, X=C or N, n defines the MXene width (normally $n=1$–3), and T_x represents one of the common terminations, most often –O, –OH, –F, or –H,[19] that are inherent to their synthesis process. The synthesis of MXenes follows a top-down approach by a selective disassembly of the MAX phase precursors; see the recent review by Zhang *et al.*[20] In the MAX phase, A stands for Al, Si, or other elements in p-block. The removal of A from the MAX phase is achieved by using different chemical etchants. Initially, the hazardous hydrofluoric acid (HF) was selected as etchant agent,[17] but F-free and Lewis acid-based routes have been very recently reported.[21,22] The broad number of applications of these materials is associated to the composition

---

[a] *A. Jurado, K. Ibarra, Dr. Á. Morales-García, Prof. F. Viñes, Prof. Dr. F. Illas*
Departament de Ciència de Materials i Química Física & Institut de Química Teòrica i Computacional (IQTCUB), Universitat de Barcelona, c/Martí i Franquès 1-11, 08028 Barcelona, Spain
E-mail: angel.morales@ub.edu

Supporting information for this article is available on the WWW under https://doi.org/10.1002/cphc.202100600

that depends on selecting M and X elements, and the number of atomic layers, *n*, controlled by selecting the appropriate MAX precursors and, finally, the surface terminating species; T_x, whose presence depends on the employed etchant agent and on the followed synthesis protocol. These three structural variables offer great opportunities for tailoring the surface chemistry and properties of MXenes.[23] We must emphasize that, although the usual synthesis lead to functionalized MXenes, recent work reported experimental protocols that that provide bare MXenes without T_x,[15,21] which opens the way to study the intrinsic chemistry of MXenes as well as their possible applications.

The bi-dimensional (2D) structural nature along with its carbide and/or nitride chemical composition suggest that MXenes may occupy a privileged position within the field of heterogeneous catalysis and electrocatalysis.[24] This view is supported by the computational prediction that pristine MXene carbides with $M_{n+1}C_n$ formula have a strong capability for activating and converting CO_2,[11] a forecast later experimentally confirmed,[15] reinforcing the potential of MXenes for CO_2 abatement, with promising CO_2 uptakes of *ca.* 8–12 mol kg^{-1} on individual MXene sheets. Further studies investigating CO_2 adsorption and desorption isotherms on MXenes such as $Ti_3C_2T_x$ and V_2CT_x, carried out at 298 K under 0–4 MPa, confirmed that the slit-like shape interlayer space generated during their synthesis is responsible for the CO_2 storage.[16] The promising results observed on MXene carbides calls for research on their counterpart nitrides.

This family has proven difficult to synthesize because, compared to the carbide family, they exhibit lower cohesive and higher formation energies,[25,26] added to the fact that aqueous HF etchant solution are not suitable for isolating $M_{n+1}N_nT_x$.[27] Fortunately, novel synthetic routes as those mentioned earlier,[21,22] have contributed to overcome this drawback making the synthesis of nitride MXenes feasible.[28,29] At this point, investigating the performance nitride MXenes for CO_2 activation becomes timely. Indeed, a previous computational study employing Density Functional Theory (DFT) methods indicated that bare M_2N (M=Ti, Zr, Hf, V, Nb, Ta, Cr, Mo, and W) systems are suitable for CO_2 capture and activation with predicted adsorption energies even higher than those predicted for the counterpart carbides, using the same computational approach.[13] These promising results required further studies aimed at investigating several open issues such as the effect of the MXene thickness and, more importantly, to identify the temperature and CO_2 partial pressure conditions at which such materials are appropriate for CCS. Both issues are addressed in the present work, the reported results providing a guide nitride MXenes on which the activation of CO_2 occurs at mild conditions.

1.1. Computational Models and Methods

Extended surface models are employed to represent the basal (0001) plane of bare nitride MXenes with formula $M_{n+1}N_n$, *n* running from 1 to 3, and M being an early transition metal, including Ti, Zr, Hf, V, Nb, Ta, Cr, Mo, and W. The M_2N surface model is built by removing the A element of the MAX phase followed by a full structural optimization. The resulting M–N–M sandwich-like configuration provides a realistic model for bare MXenes with stoichiometry M_2N and constitutes the starting point for building up thicker MXenes with general M_3N_2 and M_4N_3 formula by simply altering M and N layers following the ABC stacking sequence. In all cases, the generated M_3N_2 and M_4N_3 structures were fully relaxed prior to study the CO_2 adsorption. A $p(3\times3)$ supercell is always used to minimize the lateral interaction between adsorbed CO_2 molecules in periodically replicated images. Because, as indicated below, the calculations involve an intrinsically periodic plane wave basis set, it is necessary to include a vacuum width to avoid a spurious interaction between the periodic replicas in the direction perpendicular to the surface. Thus, a width of 10 Å is selected as it is sufficient to obtain numerically converged results, as discussed in detail in previous works.[11,13] For comparison, the (001) and (111) surfaces of the corresponding bulk face-centered cubic (*fcc*) Transition Metal Nitrides (TMNs) have been also considered. The corresponding slab models are built following the standard approach. From a structural viewpoint, the planes perpendicular to the [001] direction maintain the 1 : 1 stoichiometry of the bulk TMN, whereas those perpendicular to the [111] direction feature alternating M or N atomic layers alternate generating either M or N surface terminations. To properly compare to the MXene (0001) surfaces, only the M-terminated layer perpendicular to the [111] direction is considered. By moving from 2D to extended surfaces of bulk TMNs we will be able to firmly establish the influence of thickness on the adsorption and subsequent activation of CO_2.

To investigate the properties of the surfaces and their interaction with CO_2, we rely on first-principles periodic DFT based calculations. From the obtained results we analyze the potential of these MXenes in CCS strategies. The total energy of the explored $M_{n+1}N_n$ (0001) surfaces –M=Ti, Zr, Hf, V, Nb, Ta, Cr, Mo, and W– with $n=1$–3, as well TMN (001) and (111) ones without or with CO_2 has been optimized using the Perdew-Burke-Ernzerhof (PBE)[30] exchange-correlation functional with the dispersion forces effects included through Grimme's D3 method,[31] as implemented in the Vienna *Ab Initio* Simulation Package (VASP) code.[32] A $p(3\times3)$ supercell is used for the TMN (111) surfaces, and a $c(2\sqrt{2}\times2\sqrt{2})$P45° for the TMN(001) ones, as previously used in the past,[11,33] and having a similar number of surface metal centers; nine or eight, respectively, and so, with a comparable molecular coverage. An expansion of the valence electron density in a Plane-Wave (PW) basis set with a kinetic energy cut-off of 415 eV is used to solve the Kohn-Sham (KS) equations and the interaction between the valence electron density and the core electrons is taken into account by means of the Projector Augmented Wave (PAW) method;[34] the numerical integrations in the reciprocal space were carried out using a Monkhorst-Pack[35] grid of 5×5×1 special **k**-points is. A denser 9×9×1 grid of **k**-points is used to study the TMN surfaces. The geometry optimizations reach the convergence when the forces acting over the nuclei are all below 0.01 eV Å^{-1}.

This computational setup ensures converged results up to 1 meV in the calculated adsorption energy.

The CO_2 adsorption energy on the different MXene (0001), and MN (001) and (111) substrates is computed as $E_{ad} = E_{CO_2@ubrae} - \left(E_{CO_2} + E_{ubrae}\right) + \Delta E_{ZPE}$ where $E_{CO_2@ubrae}$ corresponds to the total energy of the CO_2 anchored over either MXene and TMN surfaces, E_{ubrae} and E_{CO_2} stand for the total energy of relaxed pristine substrates and of an isolated CO_2 molecule, respectively, and ΔE_{ZPE} includes the difference in the zero-point energy of each energetic contribution obtained assuming the harmonic approximation and decoupling of surface phonons and adsorbate vibrations. The vibrational frequencies were obtained by diagonalization of the corresponding block of the Hessian matrix with elements computed as finite difference of analytical gradients with displacements of 0.03 Å. The definition of E_{ad} above implies that negative values correspond to exothermic adsorptions. Spin polarization was not considered as this does not significantly affect E_{ad} of the $M_{n+1}N_n$ (0001) surfaces as recently reported by some of us.[36]

The results from the DFT calculations are next used to compute adsorption, r_{ads}, and desorption, r_{des}, rates at different pressure and temperature conditions. Following a previous work on CO_2 adsorption/desorption on transition metal carbides,[33] it is assumed that CO_2 adsorption is a non-activated process and can be calculated from the well-known Hertz-Knudsen equation as in Eq. (1),

$$r_{ads} = \frac{S_0 \cdot p_{CO_2} \cdot A}{\sqrt{2\pi \cdot m \cdot k_B \cdot T}}, \tag{1}$$

where S_0 is the initial sticking coefficient, p_{CO_2} corresponds to the CO_2 partial pressure above the surface, A stands for the area of an active adsorption site and m is the mass of the adsorbed molecule. A conservative value of $S_0 = 0.40$ is selected for our study following a previous analysis where the CCS were investigated on transition metal carbides and MXenes.[11,13,33] On the other hand, the rate of desorption, r_{des}, is estimated from Transition State Theory (TST)[37] assuming that the transition state for desorption is close enough to the final state so that the energy barrier can be estimated from the desorption energy. Therefore, the (negative) E_{ads} is used to estimate r_{des} as in Eq. (2)

$$r_{des} = \nu_{des} \cdot exp\left(\frac{E_{ads}}{k_B \cdot T}\right);\ \nu_{des} = \frac{k_B \cdot T \cdot q^{gas}_{trans,2D} \cdot q^{gas}_{rot} \cdot q^{gas}_{vib}}{q^{ads}_{vib}}, \tag{2}$$

with ν_{des} corresponding to the partition function of the molecule in a late 2D transition state. Here, the calculated harmonic frequencies are used to estimate the partition function of the adsorbed species whereas all degrees of freedom are considered for the gas phase CO_2 molecule. Further details can be found in Refs. [13,33].

Following this strategy, multiscale simulations are carried with the aim to shed light on the conditions at which nitride MXenes may be appropriate for CCS. These are established by analyzing the crossover between CCS and non-CCS crossover that is defined by a temperature and a CO_2 partial pressure (p_{CO_2}) at which $r_{ads} = r_{des}$. This dynamic equilibrium situation allows us to derive what we refer to as kinetic phase diagrams, a newly developed tool introduced previously by some of us,[12] where the kinetic term indicates that the phase diagrams are directly built from rates rather that from thermodynamic equilibrium arguments.

2. Results and Discussion

2.1. Adsorption Trends

We start this section by analyzing the variation of the CO_2 adsorption energy with respect to the composition and thickness of nitride MXenes, see Figure 1a. In this analysis, we explored the Potential Energy Surfaces (PESs) corresponding to different possible adsorption sites and different orientations of the CO_2 molecule. The most favorable conformations for CO_2 adsorption on the investigated nitride MXenes are displayed in Figure 1. We point out that these configurations are favorable at least in one of investigated MXenes regardless of the thickness and the composition. Similar configurations were also

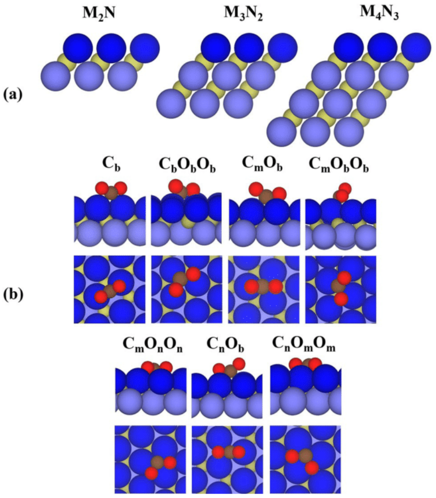

Figure 1. (a) Atomic structure of nitride MXene (0001) surfaces with formula $M_{n+1}N_n$ ($n = 1$–3) where dark and light blue spheres represent the M upper, intermediate, and bottom layers, respectively, and the inner nitrogen layer is depicted by dark yellow spheres. The M upper layer contains the sites CO_2 adsorption takes place; (b) side and top views of CO_2 adsorbed on C_b, $C_bO_bO_b$, C_mO_b, $C_mO_bO_b$, $C_mO_nO_n$, C_nO_b, and $C_nO_mO_m$ sites of MXene (0001) surfaces. In this notation, the capital letters (C or O) indicate the atoms of the CO_2 molecule that interact directly with the MXene surfaces, and the subindices indicate the bridge (b), metal (m) or nitrogen (n) hollow surface sites closest to C or O atoms.

ChemPhysChem
Articles
doi.org/10.1002/cphc.202100600
Chemistry Europe
European Chemical Societies Publishing

obtained for CO_2 adsorption on the M-terminated TMN (111) surfaces whereas different conformations were found on the TMN (001) surfaces as depicted in Figure S1 in the Supporting Information (SI).

Previous DFT calculations using PBE-D3 approach have recently reported highly exothermic CO_2 adsorption energies on bare M_2N MXenes with values ranging from −1.03 (Mo_2N) to −3.13 eV (Ti_2N).[13] This study also predicted that nitride d^2-MXenes (Ti, Zr, and Hf) have the strongest adsorption (*ca.* −3.0 eV) followed by d^3-V, Nb, and Ta (*ca.* −1.8 eV), and d^4-Cr, Mo, and W (*ca.* −1.4 eV). Here, the case of Cr_2N is an outlier being its behavior like a d^3-metal. These previous results together to those obtained here for the thicker M_3N_2 and M_4N_3 MXenes indicate that nitride MXenes with M_3N_2 stoichiometry have similar or even larger CO_2-philicity than the M_2N counterparts, see Figure 2. In particular, nitride d^2-MXenes with M_3N_2 stoichiometry feature CO_2 adsorption energies above −3.5 eV. Interestingly, no significant changes are found when moving to M_4N_3 nitride MXenes. The above results also show that the effect of the MXene thickness on the CO_2 adsorption nitride MXenes is significantly larger than in carbide MXenes.[12] This is a rather unexpected finding which hinders finding clear systematic trends. However, interesting results are observed when analyzing each case separately. Increasing the thickness markedly increases the CO_2-philicity in the Nb- and Ta-derived nitride MXenes, slightly in the Ti-, Zr-, Hf- and Mo-derived nitride MXenes, and no effect for the V- and Cr- ones. The case of nitride W-MXenes follows an opposite trend as its affinity for CO_2 decreases by increasing the thickness as further discussed later. Additional interesting insights emerges when comparing to (001) and (111) TMN surfaces. As expected from the trends in surface energy, the TMN (001) surface is clearly less active than the (111) one with a calculated adsorption energy below *ca.* −2.2 eV which is reasonable but not as high as the one corresponding to the TMN (111), behaving effectively as MXene surfaces. This indicates that the chemistry of the hard-to-prepare TMN (111) can be more easily studied using the corresponding nitride MXenes. Before closing the discussion regarding adsorption energies, it is worth mentioning that the presence of the CO_2 on the (001) and (111) CrN, MoN, and WN surfaces promotes superficial deformations inducing reconstruction which has been attributed to the fact that the rock-salt polymorph of these nitrides is not the most stable one.[38]

The large adsorption energy of CO_2 on the (0001) nitride MXene surfaces is accompanied by a considerable charge transfer from the substrate towards CO_2 which we estimate by adding the net Bader charge in the atoms of the adsorbed molecule. To explore whether a large adsorption energy is coupled to a large charge transfer with a concomitant CO_2 activation we computed the topological Bader charge, Q, of the CO_2 molecule and plotted it versus E_{ads}, see Figure 3. The corresponding plot evidences a clear trend but not a quantitative relationship. It is noteworthy that a similar trend emerges for the TMN (111) surfaces as clearly seen also in Figure 3. This is not surprising because the MXene (0001) and TMN (111) surfaces have a close structural resemblance which translates into a similar behavior towards the CO_2 adsorption. More in detail, the four set of data show that in the majority of the analyzed substrates, the E_{ads} and Q values concentrate in the −2.5 to −1.0 eV and −1.75 to −0.9 *e* range, respectively. The set of TMN (001) surfaces does not follow any clear trend except that low E_{ads} values are coupled to small Q on the CO_2 molecule. This is a clear indication of the relatively stability (low reactivity) of the TMN (001) surfaces. As expected, the charge transfer induces structural changes on the CO_2 molecule promoting a bending of the O–C–O angle; the activated $CO_2^{\delta-}$ adsorbate

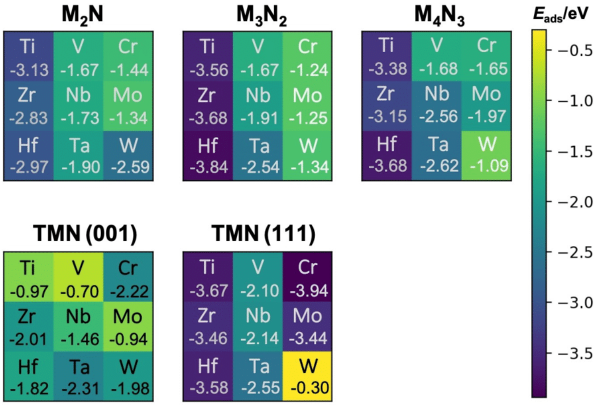

Figure 2. CO_2 adsorption energies, E_{ads}, on MXene and TMN surfaces. The scheme colors indicate the strength of the interaction between CO_2 and the substrates, given in eV. Dark blue and yellow correspond to the largest and weakest interaction. Further details can be found in the SI. Values below the label of atoms correspond to the most favorable adsorption energies on the corresponding MXene and TMN surfaces.

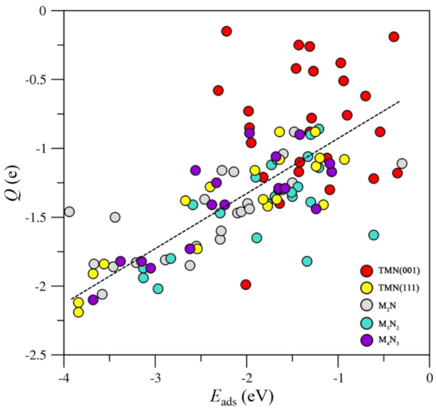

Figure 3. Bader charge on the adsorbed CO_2 molecule, Q, in e, versus adsorption energy, E_{ads}, in eV, on the MXenes nitrides ($M_{n+1}N_n$, $n=1$–3) (0001) surfaces, and TMN (001) and (111) surfaces. Note that all adsorption sites and modes for CO_2 on the explored surfaces are considered. The dashed black line is a guide view to visualize the trend.

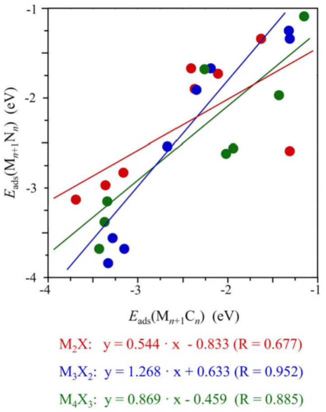

Figure 4. Comparison between E_{ads} for nitrides and carbides with different thickness. Red, blue, and green colors correspond to M_2X, M_3X_2, and M_4X_3 MXenes. The solid lines stand for the linear fitting. Note that only the most adsorption modes for CO_2 on the explored surfaces are considered.

having angles in the 111.7–135.6° interval, depending on the substrate. The deviation from linearity is connected to Q but without clear trends. All in all, the results discussed so far support the claim that bare $M_{n+1}N_n$ systems are appropriate for CO_2 abatement.

At this point, it is interesting to compare the CO_2 adsorption energy, E_{ads}, of nitride and carbide MXenes and its role on the activation of CO_2. We have shown in an earlier work that, in the case of carbide MXenes, the thickness has a small or negligible effect on their interaction with CO_2.[12] The results above show that thickness effects are much larger for nitride MXenes. To have a deeper insight in the influence of the X element (C or N) on the CO_2 adsorption, we compare the CO_2 adsorption energy for the two families of MXenes. To this end, in Figure 4 we plot E_{ads} ($M_{n+1}N_n$) versus E_{ads} ($M_{n+1}C_n$) with the data for the nitride MXenes obtained in the present work and that of MXene carbides taken from previous work.[12] The plots in Figure 4, even showing qualitative trends only, evidence that M_2N and M_4N_3 MXenes feature a lower CO_2-philicity than their carbide counterparts (M_2C and M_4C_3). On the other hand, M_3N_2 MXenes feature a larger affinity for CO_2 than their carbide counterpart (M_3C_2), although the reasons for these behaviors deserve a more detailed analysis which is out of the scope of the present work. Noting that the dispersion of the results, we observe that it is larger in E_{ads} ($M_{n+1}N_n$) than in E_{ads} ($M_{n+1}C_n$) and moving also from d^2- to d^4-MXenes which indicates that the non-metallic element in the MXenes plays a non-negligible role in the chemistry of these materials. According to the present results, one can conclude that the adsorption and activation of CO_2 could be modulated somehow playing with the nature (carbide or nitride) and the thickness of MXenes which opens a window to optimize pressure and temperature to control the adsorption/desorption process which is very relevant for the possible use of these materials in CCS technologies. This is investigated in detail in the next section.

2.2. Pressure and Temperature Effects

Here we describe the results obtained from TST derived adsorption/desorption rates and the resulting kinetic phase diagrams. These display the pressure/temperature regions where adsorption or desorption prevails with the dashed lines indicating the situations where the two rates coincide leading to a dynamic equilibrium situation. Note that these are in general different from the phase diagrams that may be obtained from atomistic thermodynamics[39] which require that the system reaches thermodynamic equilibrium. In the case that thermodynamics equilibrium occurs very rapidly both approaches coincide. Here we prefer to rely on the kinetic phase diagrams because it properly considers the dynamic nature of the equilibrium and the fact that desorption rates may be slow.

Figure 5 shows the most representative kinetic phase diagrams of bare nitride MXenes with M_2N, M_3N_2, and M_4N_3 stoichiometries. We focus mainly on nitride MXenes with the lowest (Cr_2N, Cr_3N_2, and W_4N_3) and largest (Ti_2N, Hf_3N_2, and Hf_4N_3) CO_2 adsorption energy, whereas the rest of cases including the TMN surfaces, with situations between the extreme situations shown in Figure 5, are reported in the SI. All kinetic phase diagrams display three well differentiate regions: *i*) one dominated by adsorption and relevant to CCS (dark orange) located at low *T*, *ii*) a transition zone where adsorption

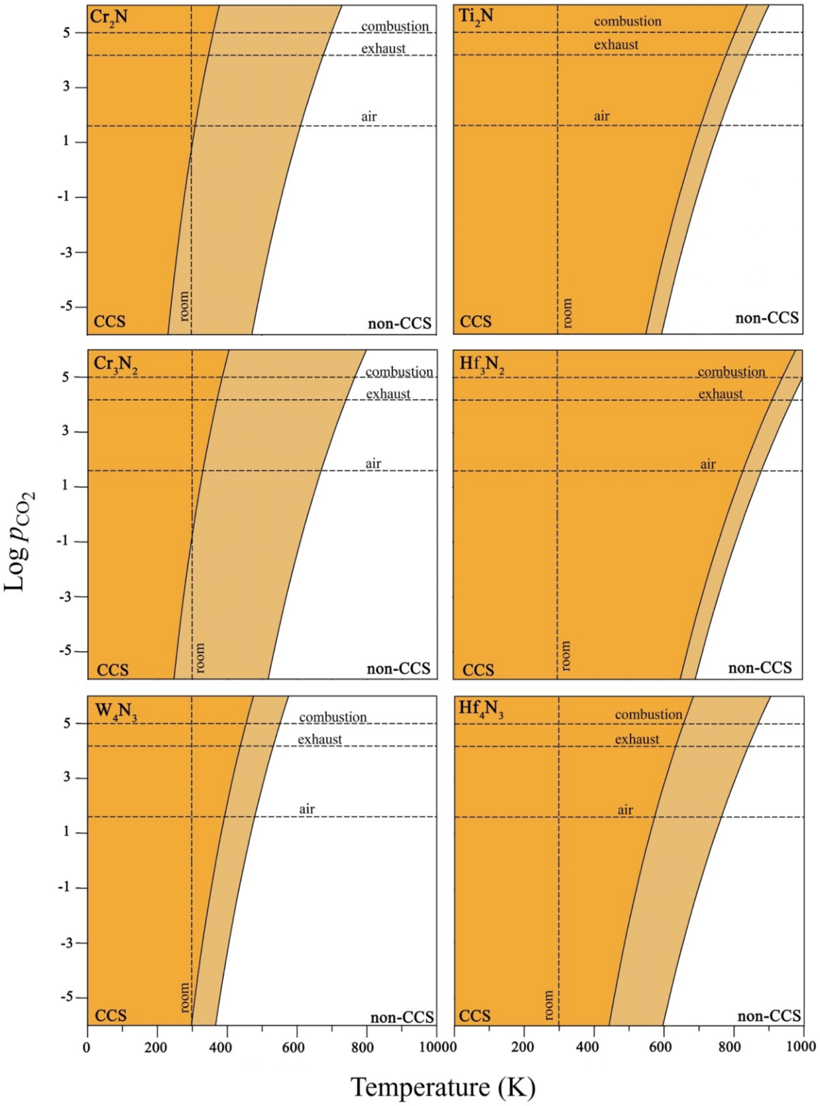

Figure 5. Kinetic phase diagrams for CO$_2$ adsorption/desorption on the (0001) $M_{n+1}N_n$ MXene surfaces. The crossover among the dashed lines indicates the conditions of CO$_2$ partial pressure (*e.g.*, air: 40 Pa, exhaust: 15 kPa, and combustion:100 kPa) and room temperature (300 K). The color scheme defines three plausible scenarios CCS, non-CCS and an intermediate situation that are depicted with dark yellow, white, and light yellow, respectively. Noting that the left and right panels stand for the least and most favorable cases for each MXene stoichiometries and the rest of cases are in the middle and are reported in the SI.

and desorption compete (light orange), and finally *iii*) the desorption dominated zone (white), where CO_2 does not adsorb at all (non-CCS zone). To provide error bars to the predictions, the border between the transition zones corresponds to the least favorable E_{ads} values as predicted by the PBE functional, whereas the border between the CCS transition and the non-CCS zones corresponds the E_{ads} values including dispersion through the PBE-D3 functional. This defines the light orange region which varies with the composition. Those substrates with a large variety of active sites with similar energetics expose a broader region than those ones whose adsorption energies are similar on different active sites. It must be noted that these limits are conservative because they include all plausible adsorption sites that are placed somewhere between them.

The CCS capability of a given surface depends on the CO_2 partial pressure, p_{CO_2}, and on the temperature. Thus, three actionable p_{CO_2} conditions are considered in the present study: *i*) atmospheric pressure where $p_{CO_2} = 40$ Pa,[40] *ii*) a benchmark value corresponding to postcombustion exhaust gases and, hence, $p_{CO_2} = 15$ kPa,[41] and *iii*) pure CO_2 stream generation from a CCS system with $p_{CO_2} = 100$ kPa (1 bar).[5] From a thermodynamic viewpoint it is convenient that CO_2 activation occurs at room temperature (*ca.* 300 K). These conditions are essential to achieve efficient CO_2 capture from air. Indeed, this is the main idea behind the technologies based on the Direct Air Capture (DAC).[42] From the results summarized in Figure 5, the Cr_2N, Cr_3N_2, and W_4N_3 MXene (0001) exposed surfaces exhibit the lowest CO_2-philicity. Although all partial p_{CO_2} at 300 K are located inside the CCS zone, CO_2 could be easily released just by increasing slightly the temperature at constant pressure. This scenario is especially highlighted on the Cr-derived MXenes. On the other hand, the Ti_2N, Hf_3N_2, and Hf_4N_3 MXene (0001) surfaces featuring the largest E_{ads} are appropriate exclusively for CO_2 trapping, as conditions are well in the CCS region and the shift towards the non-CCS regime maintaining the p_{CO_2} constant requires high temperatures that could compromise somehow the stability of these MXene compounds. Note that the latter MXenes are highly reactive, and their surfaces are passivized by CO_2 even under mild conditions.

From the preceding discussion Cr_2N, Cr_3N_2, and W_4N_3 nitride MXene emerge as promising DAC filters where CO_2 is chemisorbed but can be easily released. Thus, once the MXene filters become saturated, heating at temperatures close to 500 K release CO_2 for subsequent use or storage and regenerates the filter. The thus obtained CO_2 feedstock can be employed in a second step to synthesis of fuels and chemicals based on the heterogeneously catalyzed CO_2 hydrogenation *via* the reverse water gas shift (RWGS) or Fischer-Tropsch reactions.[43] Note also that the (001) surfaces of bulk TMNs constitute potential substrates due to their not so high interaction with CO_2 making feasible the carbon capture and usage.

Before ending this section, we must point out that the present results have been obtained for a low coverage situation and that lateral interactions are likely to decrease the adsorption energy so MXenes with larger E_{ads} at low coverage renders CCS suitable while those with smaller E_{ads} may end up in being less useful. Note, however, that that the experimental uptake in the work of Persson *et al.*[15] qualitatively agree with predictions for the M_2C MXenes made using a similar low coverage situation[11] thus indicating that the coverage effects, while important, will not change the overall conclusions of the present work. Besides, the border zone in the kinetic phase diagrams already take into account possible error bars in the adsorption energy.

3. Conclusions

The (0001) nitride MXene surfaces with $M_{n+1}N_n$ ($n = 1$–3; M=Ti, Zr, Hf, V, Nb, Ta, Cr, Mo, and W) stoichiometries and the (001) and (111) TMN surfaces were investigated as plausible substrates for CO_2 capture. By means of a combination of first-principles calculations and macroscopic simulations, the role of the thickness and the composition are revealed. The effect of the thickness on CO_2 adsorption and activation is larger than in the case of carbide MXenes. For a given TM, all nitride MXenes expose similar CO_2-philicity but with small, yet noticeable, differences. On the contrary, the effect of the TM is very large, as in carbide MXenes, with Ti, Hf, and Zr-derived nitride MXenes featuring the most exothermic adsorption followed by V, Nb, and Ta-derived nitride MXenes and, finally, Cr, Mo, and W-derived ones. The trends here reported for nitride MXenes of different thickness are somehow different to those reported for carbide MXenes with a much more marked influence of the nitride MXene thickness in the calculated CO_2 adsorption energy. The analysis of the results also shows that the MXene (0001) surfaces behave as the (111) surface of bulk TMNs. These trends in adsorption energy are consistent with a significant charge transfer from the MXene (or TMN) substrate towards the CO_2 molecule, a clear indication that, once chemisorbed on the MXenes, the CO_2 molecule is highly activated which call for additional work to analyze its possible conversion to other useful chemicals. By comparing MXene carbides and nitrides, it is concluded that M_2N and M_4N_3 MXenes have, in general, less affinity for CO_2 than their carbide counterparts (M_2C and M_4C_3), whereas the family M_3N_2 exposes larger affinities than M_3C_2. The present results suggest that the CO_2 adsorption on MXenes can be monitored by selecting the appropriate composition and thickness of the material.

Finally, newly developed kinetic phase diagrams have been introduced that allow one to identify the conditions at which the MXene substrates are able to capture and release CO_2. These diagrams provide unbiased information that can be useful to experimentalists and engineers working on CCS. We conclude that (Cr, Mo, and W)-derived MXenes constitute the most suitable materials to act as collector of CO_2 due to the feasible CO_2 capture at mild conditions and the affordable release by heating below 500 K. MXene can act as CO_2 feedstock to heterogenous catalytic processes as the CO_2 hydrogenation to obtain valuable fuels and chemicals.

Acknowledgements

The research carried out at the Universitat de Barcelona has been supported by the Spanish MICIUN/FEDER RTI2018-095460-B-I00 and María de Maeztu MDM-2017-0767 grants and, in part, by Generalitat de Catalunya 2017SGR13 grant and COST Action CA18234. A.M.-G. is thankful to the Juan de la Cierva Incorporación postdoctoral grant IJCI-2017-31979 and F. I. acknowledges additional support from the 2015 ICREA Academia Award for Excellence in University Research. Computational resources provided by the Red Española de Supercomputación (QS-2020-1-0006) are fully acknowledged.

Conflict of Interest

The authors declare no conflict of interest.

Keywords: carbon capture · nitride MXene · density functional calculations · charge transfer · kinetic phase diagram

[1] J. Lelieveld, K. Klingmüller, A. Pozzer, R. T. Burnett, A. Haines, V. Ramanathan, *Proc. Natl. Acad. Sci. USA* **2019**, *116*, 7192–7197.
[2] T. R. Anderson, E. Hawkins, P. D. Jones, *Endeavour* **2016**, *40*, 178–187.
[3] C. D. Keeling, *Proc. Natl. Acad. Sci. USA* **1997**, *94*, 8273–8274.
[4] C. Hepburn, E. Adlen, J. Beddington, E. A. Carter, S. Fuss, N. Mac Dowell, J. C. Minx, P. Smith, C. K. Williams, *Nature* **2019**, *575*, 87–97.
[5] M. E. Boot-Handford, J. C. Abandes, E. J. Anthony, M. J. Blunt, S. Brandani, N. Mac Dowell, J. R. Fernández, M.-C. Ferrari, R. Gross, J. P. Hallett, R. S. Haszeldine, P. Heptonstall, A. Lyngfelt, Z. Makuch, E. Mangano, R. T. J. Porter, M. Pourkashanian, G. T. Rochelle, N. Shah, J. G. Yao, P. S. Fennell, *Energy Environ. Sci.* **2014**, *7*, 130–189.
[6] Á. Morales-García, F. Viñes, J. R. B. Gomes, F. Illas, *WIREs Comput. Mol. Sci.* **2021**, *11*, e1530.
[7] T. P. Senftle, E. A. Carter, *Acc. Chem. Res.* **2017**, *50*, 472–475 and references therein.
[8] I. S. Omodolor, H. O. Otor, J. A. Andonegui, B. J. Allen, A. C. Alba-Rubio, *Ind. Eng. Chem. Res.* **2020**, *59*, 17612–17631.
[9] M. T. Dunstan, A. Jain, W. Liu, S. P. Ong, T. Liu, J. Lee, K. A. Persson, S. A. Scott, J. S. Dennis, C. P. Grey, *Energy Environ. Sci.* **2016**, *9*, 1346–1360.
[10] A. Álvarez, M. Borges, J. J. Corral-Pérez, J. G. Olcina, L. Hu, D. Cornu, R. Huang, D. Stoian, A. Urakawa, *ChemPhysChem* **2017**, *18*, 3135–3141.
[11] Á. Morales-García, A. Fernández-Fernández, F. Viñes, F. Illas, *J. Mater. Chem. A* **2018**, *6*, 3381–3385.
[12] Á. Morales-García, M. Mayans-Llorach, F. Viñes, F. Illas, *Phys. Chem. Chem. Phys.* **2019**, *21*, 23136–23142.
[13] R. Morales-Salvador, Á. Morales-García, F. Viñes, F. Illas, *Phys. Chem. Chem. Phys.* **2018**, *20*, 17117–17124.
[14] L. M. Azofra, N. Li, D. R. MacFarlane, C. Sun, *Energy Environ. Sci.* **2016**, *9*, 2545–2549.
[15] I. Persson, J. Halim, H. Lind, T. W. Hansen, J. B. Wagner, L.-Å. Näslund, V. Darakchieva, J. Palisaitis, J. Rosen, P. O. Å. Persson, *Adv. Mater.* **2019**, *31*, 1805472.
[16] B. Wang, A. Zhou, F. Liu, J. Cao, L. Wang, Q. Hu, *J. Adv. Ceram.* **2018**, *7*, 237–245.
[17] M. Naguib, M. Kurtoglu, V. Presser, J. Lu, J. Niu, M. Heon, L. Hultman, Y. Gogotsi, M. W. Barsoum, *Adv. Mater.* **2011**, *23*, 4248–4253.
[18] B. Anasori, Y. Gogotsi, *2D Metal Carbides and Nitrides (MXenes), Structure, Properties and Applications*. Springer: Berlin, **2019**.
[19] Y. Gogotsi, B. Anasori, *ACS Nano* **2019**, *13*, 8491–8494.
[20] Z. Zhang, X. M. Duan, D. C. Dechang, Y. Zhou, S. van der Zwaag, *J. Eur. Ceram. Soc.* **2021**, *41*, 3851–3878.
[21] V. Kamysbayev, A. S. Filatov, H. Hu, X. Rui, F. Lagunas, D. Wang, R. F. Klie, D. V. Talapin, *Science* **2020**, *369*, eaba8311.
[22] Y. Li, H. Shao, Z. Lin, J. Lu, L. Liu, B. Duployer, P. O. Å. Persson, P. Eklund, L. Hultman, M. Li, K. Chen, X.-H. Zha, S. Du, P. Rozier, Z. Chai, E. Raymundo-Piñero, P.-L. Taberna, P. Simon, Q. Huang, *Nat. Mater.* **2020**, *19*, 894–899.
[23] Y. Gogotsi, Q. Huang, *ACS Nano* **2021**, *15*, 5775–5780.
[24] Á. Morales-García, F. Calle-Vallejo, F. Illas, *ACS Catal.* **2020**, *10*, 13487–13503.
[25] I. R. Shein, A. L. Ivanovskii, *Comput. Mater. Sci.* **2012**, *65*, 104–114.
[26] D. Dolz, Á. Morales-García, F. Viñes, F. Illas, *Nanomaterials* **2021**, *11*, 127.
[27] Q. Ye, P. Xiao, W. Liu, K. Chen, T. Chen, J. Xue, S. Du, Q. Huang, *RSC Adv.* **2015**, *5*, 70339–70344.
[28] P. Urbankowski, B. Anasori, T. Makaryan, D. Er, S. Kota, P. L. Walsh, M. Zhao, V. B. Shenoy, M. W. Barsoum, Y. Gogotsi, *Nanoscale* **2016**, *8*, 11385–11391.
[29] B. Soundiraraju, B. K. Goerge, *ACS Nano* **2017**, *11*, 8892–8900.
[30] J. P. Perdew, K. Burke, M. Ernzerhof, *Phys. Rev. Lett.* **1996**, *77*, 3865–3868.
[31] S. Grimme, J. Antony, S. Ehrlich, H. Krieg, *J. Chem. Phys.* **2010**, *132*, 154104.
[32] G. Kresse, J. Furthmüller, *Phys. Rev. B* **1996**, *54*, 11169–11186.
[33] C. Kunkel, F. Viñes, F. Illas, *Energy Environ. Sci.* **2016**, *9*, 141–144.
[34] P. E. Blöchl, *Phys. Rev. B* **1994**, *50*, 17953–17979.
[35] H. J. Monkhorst, J. D. Pack, *Phys. Rev. B* **1976**, *13*, 5188–5192.
[36] J. D. Gouveia, Á. Morales-García, F. Viñes, F. Illas, J. R. B. Gomes, *Appl. Catal. B* **2020**, *260*, 118191.
[37] K. Reuter, *Modelling and Simulation of Heterogeneous Catalytic Reactions*, Wiley-VCH Verlag GmbH & Co. KgaA, New York, NY, **2011**.
[38] M. Figueras, A. Jurado, Á. Morales-García, F. Viñes, F. Illas, *Phys. Chem. Chem. Phys.* **2020**, *22*, 19249–19253.
[39] K. Reuter, M. Scheffler, *Phys. Rev. B* **2001**, *65*, 035406.
[40] T. Takahashi, S. Sutherland, A. Kozyr, *Global Ocean Surface Water Partial Pressure of CO_2 Database: Measurements Performed During 1957–2014 (Version 2014), Environmental Sciences Division*, Oak Ridge National Laboratory, **2015**.
[41] D. M. D'Alessandro, B. Smit, J. R. Long, *Angew. Chem. Int. Ed.* **2010**, *49*, 6058–6082; *Angew. Chem.* **2010**, *122*, 6194–6219.
[42] E. S. Sanz-Pérez, C. R. Murdock, S. A. Didas, C. W. Jones, *Chem. Rev.* **2016**, *116*, 11840–11876.
[43] R.-P. Ye, J. Ding, W. Gong, M. D. Argyle, Q. Zhong, Y. Wang, C. K. Russell, Z. Xu, A. G. Russell, Q. Li, M. Fan, Y.-G. Yao, *Nat. Commun.* **2019**, *10*, 5698.

Manuscript received: August 12, 2021
Revised manuscript received: September 23, 2021
Accepted manuscript online: September 23, 2021
Version of record online: October 13, 2021

4.4 Conclusions

The interaction of CO_2 with nine-transition metal nitrides (M=Ti, Zr, Hf, V, Nb, Ta, Cr, Mo, and W), TMN (001) and (111), and their low-dimensional counterparts, MXenes, with different thickness M_2N, M_3N_2 and, M_4N_3 has been carried out. Calculations show that the composition of the material influences on the CO_2-philicity of the sample while the thickness presents a low effect. The results prior presented lead to the following conclusions:

- d^2-MXenes, Ti, Zr and Hf, present the most exothermic adsorption energies followed by d^3-MXenes (V, Nb and Ta) and d^4-MXenes (Cr, Mo and W).
- The increase of the thick of the structure slightly affect this trend. However, d^3- Nb- and Ta-MXenes are widely affected by the thickness increase, whereas V- and d^4 Cr-MXenes are not affected at all.
- CO_2 affinity decreases by increasing the thickness on W-derived MXenes.
- The similarities between TMN(111) and MXene surfaces also implies resemblances towards CO_2 adsorption.
- Kinetic phase diagrams show diagrams with smaller regions or lower CO_2-philicity when the adsorption energies are small. In the other hand, larger adsorption energies exhibit larger CCS conditions, suitable for trapping CO_2.
- CO_2 affinity of MXenes can be controlled by the composition and thickness of the material.

4.5 References

1. Alhabeb, M.; Maleski, K.; Mathis, T. S.; Sarycheva, A.; Hatter, C. B.; Uzun, S.; Levitt, A.; Gogotsi, Y. Selective Etching of Silicon from Ti_3SiC_2 (MAX) To Obtain 2D Titanium Carbide (MXene). *Chem., Int. Ed.,* **2018,** 57, 5444.
2. Anasori, B.; Lukatskaya, M. R.; Gogotsi, Y. 2D Metal Carbides and Nitrides (MXenes) for Energy Storage. *Nat. Rev. Mater.* **2017**, 2, 16098.
3. Alhabeb, M.; Maleski, K.; Anasori, B.; Lelyukh, P.; Clark, L.; Sin, S.; Gogotsi, Y. Guidelines for Synthesis and Processing of Two-Dimensional Titanium Carbide ($Ti_3C_2T_x$ MXene). *Chem. Mater.*, **2017,** 29, 7633−7644.
4. Zhan, X.; Si, C.; Zhou, J.; Sun, Z. MXene and MXene-Based Composites: Synthesis, Properties and Environment-Related Applications. *Nanoscale Horiz.*, **2020**, *5*, 2 235–258.
5. Zhao, D.; Chen, Z.; Yang, W.; Liu, S.; Zhang, X.; Yu, Y.; Cheong, W.-C.; Zheng, L.; Ren, F.; Ying, G.; Cao, X.; Wang, D.: Peng, Q., Wang, G., Chen, C. MXene (Ti_3C_2) Vacancy-Confined Single-Atom Catalyst for Efficient Functionalization of CO_2. *J. Am. Chem. Soc.*, **2019**. *141*, 9, 4086–4093.
6. Morales, R.; Gouveia, J. D.; Morales-García, Á.; Viñes, F.; Gomes, J. R. B.; Illas. F. Carbon Capture and Usage by MXenes. *ACS Catal.* **2021,** 11, 17, 11248–11255.
7. Truhlar, D. G.; Garrett, B. C.; Klippenstein, S. J. Current Status of Transition-State Theory. *J. Phys. Chem.* **1996**, 100, 31, 12771-12800.

8. Peters, B. Reaction Rate Theory and Rare Events Simulations, Elsevier, **2017**, 10, 227-271. 10.1016/B978-0-44-456349-1.0001

CHAPTER FIVE

Effect of Stacking on Adsorption of Molecular Probes on Carbide MXenes

Chapter 5

5.1 Introduction

Usually, MXene materials present a layered hexagonal structure which comes directly from the MAX phase.[1] In principle, the ABC stacking is the most stable one in MXenes.[2] Recently, Gouveia *et al*.[3] performed a computational study showing that carbide and nitride MXenes can display two different stackings arising from a phase transition, where the C-layer shifts to the A-layer position, with the consequence of the narrow of the structure. This analysis found out Cr-, Mo-, and W-derived MXenes are energetically more stable in their ABA stacking sequence. Pristine Mo_2C exhibits these two competitive crystal structures with an addressable energy barrier and, given the fact that how the structure can influence on their adsorption properties is not well understood, the motivation of this study is to understand the possible effect of stacking on the carbide MXenes.

To fulfil this, adsorption properties of ABA and ABC slabs of Mo_2C MXene are studied through periodic density functional based calculations of a group of chosen probe molecules, CO, CO_2, and H_2O. Thereby, substantial differences are present between the different stackings that could be used to provide information about the crystal structure through the IR vibration of the active molecules on the surface.

5.2 Main results

To analyse the adsorption properties of the different slabs of Mo_2C MXene, four different structures are used: 1T and 2H (ABC and ABA), the conventional structures of the Mo_2C MXene and their compressive and tensile structures, 1T' and 2H'. Figure 5.1 show the most favourable adsorption sites for the 1T and 2H, being the same sites investigated in their intermediate structures.

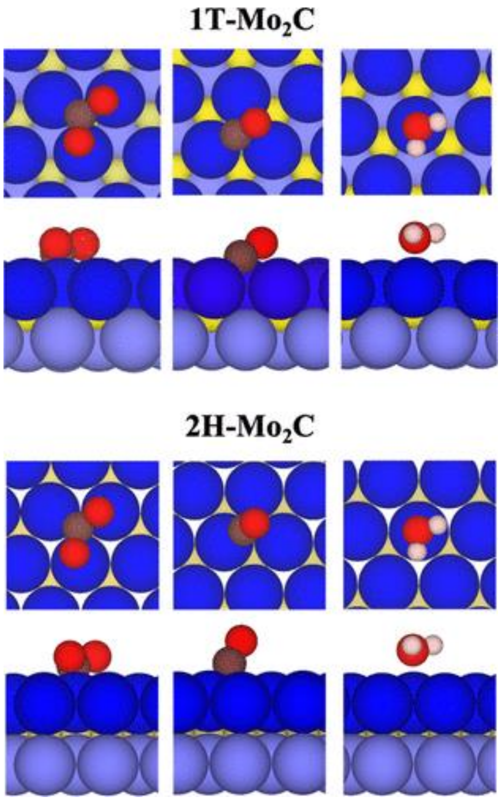

1T-Mo_2C

2H-Mo_2C

Figure 5.1 Top (top) and side (bottom) views of the adsorption sites of CO_2, CO, and H_2O species on 1T- and 2H-Mo_2C MXenes. Sites investigated on 1T′- and 2H′-Mo_2C MXenes are analogous. In addition, dark and light blue spheres represent the molybdenum atoms, yellow sphere the carbon atom of the MXene and the brown, white, and red spheres represent carbon, hydrogen, and oxygen atoms, respectively.

Results show that the adsorption energy of the 1T structure -1.85 eV decreases to -1.21 eV with the compression strain. Going to the 2H structure further reduces to -0.94 eV and as expected, increasing the tensile strain the value of the energy increases to -2.03 eV. All structures perform an exothermic adsorption, and the strong chemisorption promotes the elongation of the C–O distance and the O–C–O angle with respect to the gas-phase values, see Table 5.1. Note that this trend also holds for the CO and H_2O molecule.

	E_{ads} / eV	$d_{C\text{-}O}$ / Å	$d_{Mo\text{-}O}$ / Å	$d_{Mo\text{-}C}$ / Å	∠OCO / º	Q / e
1T	-1.80	1.34(×2)	2.08(×2)	1.64	117	-1.27
1T’	-1.21	1.32(×2)	2.11(×2)	1.63	119	-1.24
2H	-0.94	1.31(×2)	2.15(×2)	1.63	121	-1.24
2H’	-2.03	1.32(×2)	2.04(×2)	1.33	115	-1.23
CO_2 (g)		1.18(×2)			180	

Table 5.1 CO_2 Adsorption Energies, E_{ads}, on (0001) Mo2C MXene Surfaces. Most Relevant Structural Features Based on Atomic Distances, d, and Angles.

However, results show that the structural features of H_2O are unaltered in comparison to their gas phase molecule and the charge transfer toward water is almost zero. The reason behind this is that water could be governed by dispersion.

Thus, regardless of the molecule (CO_2, CO and, H_2O) the adsorption strength is larger on the (0001) 1T than on 2H-Mo_2C surfaces. This is correlated with the relative stability of the surfaces: adsorption stabilizes the less stable 1T-Mo_2C surface.

Considering that the adsorption properties are influenced by the stacking of the MXene structure, the IR or Raman vibrational analysis of the molecules (CO_2, H_2O and CO) can be used to identify the different polymorphs of the MXene. For example, for the CO_2 molecule, its asymmetric stretching for the 1T polymorph decreases its value by 1000 cm^{-1} with respect to its gas-phase counterpart and differs by ∼200 cm^{-1} with respect with 2H-Mo2C MXenes. On the CO case, the difference on its symmetric stretching between the gas phase with respect the 1T is ~700 cm^{-1}. These differences could be sufficient to distinguish ABC and ABA stackings in Mo2C MXene samples.

	Gas phase	**1T**	**1T’**	**2H**	**2H’**
			CO_2		
ν_{as}	2363	1130	1212	1283	1141
Δ		1233	1151	1080	1222
ν_s	1317	1033	1044	1049	1100
Δ		284	273	268	217
δ	635	662	673	674	710
Δ		-27	-38	-39	-75
			H_2O		
ν_{as}	3842	3625	3641	3656	3685
Δ		217	201	186	157
ν_s	3729	3527	3536	3549	3576
Δ		202	193	180	153
δ	1587	1519	1520	1526	1530
Δ		68	67	61	57
			CO		
ν_s	2131	1465	1795	1773	1439
Δ		666	336	358	692

Table 5.2 Vibrational Modes and Frequencies of the CO_2, H_2O, and CO Molecules in the Gas Phase and when adsorbed over (0001) 1T-, 1T′-, 2H-, and 2H′-Mo2C MXene Surfaces. All values in cm^{-1}.

5.3 Publication 2

Identifying the atomic layer stacking of Mo_2C MXene by probe molecule adsorption

THE JOURNAL OF PHYSICAL CHEMISTRY C
A JOURNAL OF THE AMERICAN CHEMICAL SOCIETY
pubs.acs.org/JPCC
Article

Identifying the Atomic Layer Stacking of Mo_2C MXene by Probe Molecule Adsorption

Anabel Jurado, Ángel Morales-García,* Francesc Viñes, and Francesc Illas

Cite This: J. Phys. Chem. C 2021, 125, 26808−26813
Read Online

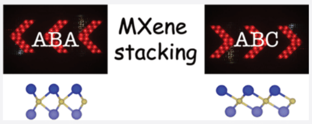

ABSTRACT: A density functional theory study is presented here aimed at investigating whether the atomic stacking on the new family of two-dimensional MXene materials has an influence on their adsorption properties and whether these properties can provide information about this structural feature. To this end, the Mo_2C MXene, exhibiting two nearly degenerate crystal structures with either ABC or ABA atomic stacking, is chosen as a case study. The study of the adsorption of CO, CO_2, and H_2O on both polymorphs of Mo_2C reveals substantial differences that could be used in experiments to provide information about the atomic stacking of a given sample. Particularly, we show that the asymmetric and symmetric stretching modes of the adsorbed CO_2 and the CO stretching mode are clear features that allow one to identify the stacking of atomic layers of the Mo_2C MXene. The present finding is likely to apply to other MXenes as well.

1. INTRODUCTION

The discovery of low-dimensional transition-metal carbides and nitrides, known as MXenes,[1,2] has generated great expectation because of the broad number of applications of these materials emerging from their unique electronic, optical, chemical, mechanical, catalytic, and sensing properties.[3−8] To some extent, these properties can be modulated by varying the MXene structure and composition. MXenes are specified by the $M_{n+1}X_nT_x$ general formula where $n = 1−3$ and M, X, and T_x denote an early transition metal, carbon or nitrogen, and surface terminations on the surface of the outer transition metal layer, respectively. MXenes are synthesized from MAX precursors, a well-known class of layered materials.[3] This generally implies a top-down approach where the atomic A-layer—generally a *p*-block element—is selectively etched and MXene flakes of different sizes are thus obtained.[1] Depending on the synthesis procedure and conditions, the MXene flakes can be covered (*i.e.*, functionalized) by O, H, OH, NH, F, Cl, Br, S, Se, or Te,[6,9,10] although terminations can be altered or even completely removed by postprocessing.[10−12] The resulting MXenes may have different stoichiometries depending on the occupation of M sites, which may correspond to one or more transition metal atoms forming solid solutions or ordered structures. In the first case, one has the conventional family of MXenes, whereas the second case leads to newer families that are referred to as *i*-MXenes or *o*-MXenes.[13−15] Recently, it has been theoretically suggested that the MXene synthesizability is related somehow to the exfoliating energy of the MAX precursor.[16] As expected, the MXene atomic composition largely defines the underlying chemistry. For instance, the response of M_2C and M_2N MXenes to the presence of carbon dioxide (CO_2) is larger for M = Ti, Zr, and Hf, milder for M = Cr, Mo, and W, and quite reactive for M = V, Nb, and Ta. Apart from the MXene composition and, obviously, from surface functionalization, there are two additional features that, in principle, can influence the reactivity of a given MXene. These are the number of atomic layers and the atomic layer stacking.

In the case of bare MXenes, the effect of the atomic thickness has been recently investigated, analyzing the adsorption of CO_2 over a broad family of MXene carbides with three, five, or seven ($n = 1−3$) atomic layers.[17] This computational study confirmed that the thickness of bare MXene has a rather little contribution to the reactivity of MXenes. However, the effect of atomic layer stacking deserves some separate discussion. It is often assumed that because of their good thermal stability,[18] MXenes feature the ABC stacking inherited from the MAX precursor. In this stacking, each atomic layer is horizontally shifted with respect to the immediate predecessor layer, but a different ABA stacking is also possible. Recently, first-principles based calculations have been used to explore the relative stability of the ABA and ABC stackings for a series of MXenes.[19] This study predicted that the ABA layer stacking is energetically favorable in Cr-, Mo-, and W-derived MXene carbides and nitrides, and such trends are more pronounced with increasing thickness. Hence, even if the ABC stacking is initially expected to show up, a phase transformation is indeed possible, driven simply by thermody-

Received: August 26, 2021
Revised: October 11, 2021
Published: November 23, 2021

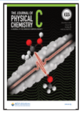

ACS Publications

https://doi.org/10.1021/acs.jpcc.1c07577
J. Phys. Chem. C 2021, 125, 26808−26813

namics. In addition, the presence of adsorbates could also change the relative stability order of the two phases. This hypothesis has been confirmed in Mo_2N and W_2N MXenes, where the activation of the N_2 molecule promotes somehow the mentioned structural distortion.[20] Another interesting case is V_2N MXene, which after etching the MAX precursor initially exhibits the ABC stacking. However, the ABA stacking has also been observed after exposing the former carbides to ammonia.[21] To study the implication of the stacking on the chemical activity, the adsorption and dissociation of molecular N_2 were studied, and it confirmed that stacking affects the adsorption strength with changes of up to ∼1 eV.[19]

Previous studies call for further investigations aimed at better understanding the effect that atomic layer stacking in MXenes has on their surface properties and, in particular, on the activation of the stable molecules. Furthermore, there is a need to provide a simple way to assess whether the ABC or ABA stacking is present in a given sample. In the present work, we investigate the adsorption of CO_2, CO, and H_2O molecules, taken as probe molecules, on the Mo_2C MXene which is an appropriate case example. In this MXene, both ABC and ABA stackings are energetically competitive; the ABA being energetically more favorable by ∼0.4 eV per formula unit only. In addition, Mo_2C is one of the MXenes with moderate adsorption strengths which make it suitable for sensing purposes.[4] The analysis of the results presented in this work provides compelling evidence that ABC and ABA stackings lead to different chemistries. In addition, we will show that the vibrational frequencies of the adsorbed species provide a simple and efficient way to identify the atomic stacking in the experiments.

2. COMPUTATIONAL DETAILS AND MODELS

To investigate the influence of the stacking on the surface properties, we have chosen the CO molecule which is a prototypal probe molecule in surface science and included CO_2 and H_2O molecules because they exhibit strong interactions with the bare MXene surfaces.[22−24] The present study relies on periodic density functional theory based calculations for the interaction of CO_2, CO, and H_2O on slab models of Mo_2C MXenes with ABC and ABA stackings. In analogy to single-layer transition metal dichalcogenides featuring similar structures,[25] these are referred to as 1T and 2H. In the 2H phase, the Mo atomic layers are vertically aligned, whereas in the 1T phase, the two Mo layers are horizontally shifted relative to each other; see Figure 1. A $p(3\times3)$ supercell is always used to minimize the lateral interaction between adsorbed molecules in the periodically replicated images, and a vacuum width of 10 Å is included to avoid spurious interactions between the periodic replicas in the direction perpendicular to the surface. These settings have proven to be sufficient to obtain numerically converged results (see *e.g.*, the review in ref 26).

The valence electron density is expanded in a plane wave basis set with a cutoff of 415 eV for the kinetic energy, while the effect of the atomic cores on the valence electronic density is taken into account through the projector augmented wave approach.[27] A Monkhorst−Pack[28] grid of 5×5×1 special **k**-points is used to carry out the numerical integrations in the reciprocal space. The total energy is obtained by solving the Kohn−Sham equations with the generalized gradient approximation for the exchange and correlation density functional using the form proposed by Perdew−Burke−Ernzerhof (PBE)[29] augmented with the Grimme D3 method to account for the contribution of dispersion.[30] Regarding the choice of the functional used in the present work, it is necessary to point out that none of the existing functionals is free of limitations, so it cannot be claimed that a particular choice will provide near-exact results. Nevertheless, the PBE functional has proven to be among the most robust when describing the properties of bulk and surface transition metals.[31−33] Consequently, it has been broadly used in the computational heterogeneous catalysis field.[26] In addition, the adsorption and, more importantly, reactivity of molecules adsorbed at the MXene surfaces is well-described by PBE-D3 as shown in previous works.[17,19] In any case, we must emphasize that our goal here is to capture trends based on adsorption strengths that allow us to distinguish different stackings of Mo_2C MXene as discussed later, and the choice of a different functional within the same or higher level of theory is likely to predict essentially the same trends.

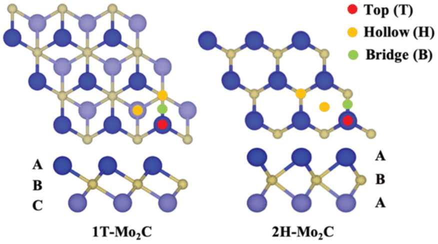

Figure 1. Top (top images) and side (bottom images) views of $Mo_2C(0001)$ MXene with ABC (1T) and ABA (2H) atomic sequences. Dark and light blue spheres represent the top and bottom Mo layers, while yellow spheres represent the C layer located between them. Red, yellow, and green spheres indicate the adsorption sites where the probed molecules are anchored.

The geometry optimization calculations are considered converged when the forces acting over the nuclei are all below 0.01 eV Å^{-1}. Overall, this computational setup ensures converged results up to 1 meV in the calculated adsorption energies. For the studied molecules, the adsorption energy, E_{ads}, on each of the two models of the $Mo_2C(0001)$ surface, see Figure 1, is computed as

$$E_{ads} = E_{molecule@Mo_2C} - (E_{molecule} + E_{Mo_2C}) + \Delta E_{ZPE} \qquad (1)$$

where $E_{molecule@Mo_2C}$ corresponds to the total energy of the molecule adsorbed on the Mo_2C surface, while $E_{molecule}$ and E_{Mo_2C} stand for the total energy of the isolated molecule in the gas phase and the relaxed pristine Mo_2C slab model, either with 1T or 2H stacking. Finally, ΔE_{ZPE} stands for the difference in the zero-point energy (ZPE) between the gas phase and adsorbed molecules. Note that inclusion of the ZPE term is necessary to compare with the experiments as it accounts for the contribution of the adsorbate normal modes to the total energy. ΔE_{ZPE} is here approximated assuming harmonic frequencies for adsorbate vibrations decoupled from surface phonons. The frequencies are obtained by diagonalization of the corresponding block of the Hessian matrix with elements computed as finite difference of analytical gradients with displacements of 0.03 Å. The definition of E_{ads} above implies that negative values correspond to exothermic adsorptions. All calculations have been carried out using the Vienna *ab initio* simulation package.[34]

3. RESULTS AND DISCUSSION

We start this section by analyzing the adsorption strength of CO_2, CO, and H_2O species on the two different Mo_2C(0001) surfaces corresponding to the two possible stackings in this MXene plus a third set corresponding to intermediate structures that are used to extract additional information, as described below. The first surface model, hereafter denoted as 1T-Mo_2C MXene, corresponds to the ABC stacking expected from the exfoliation of the corresponding MAX phase. The second structural model is obtained by inducing a biaxial in-plane compression on 1T-Mo_2C; this will be referred to as the strained 1T′-Mo_2C MXene model. Finally, the third surface is obtained by shifting one of the Mo layers in 1T′-Mo_2C leading to the 2H-Mo_2C MXene with ABA stacking. Note also that a biaxial in-plane tensile strain over 2H-Mo_2C leads to the strained 2H′-Mo_2C, which by shifting one of the Mo layers closes the cycle as it leads to the original 1T-Mo_2C MXene. We note that previous theoretical work suggests that the ABA to ABC transition is achievable at a rather low energy cost.[19] Note that the strain is brought here to easily identify the connectivity among different Mo_2C structures rather than just relying on raw values for each structure.

From a structural viewpoint, the conventional 1T- and 2H-Mo_2C MXenes have different lattice parameters, 9.29 and 8.52 Å, respectively. On the other hand, the 1T′-Mo_2C model has the same stacking of 1T structure but with the 2H-Mo_2C lattice parameter. Similarly, the 2H′-Mo_2C features the 2H structure stacking but with the 1T-Mo_2C lattice parameter. Therefore, the strained 1T′- and 2H′-Mo_2C MXenes are described as the compressive and tensile structures of 1T- and 2H-Mo_2C MXenes, respectively. Among them, the 1T-Mo_2C MXene has been previously investigated by some of us analyzing its adsorption capacity with CO_2, CO, and H_2O molecules,[22−24] and no information is available for the rest of the models. Providing this information is also a goal of the present work.

Based on the topology of the MXene surface, we have considered top (T), bridge (B), and hollow (H) sites (see Figure 1), which are systematically investigated for all probed molecules. Furthermore, the probed molecules are anchored over MXene surfaces considering different conformations. Different sites and molecular orientations have been investigated, the most likely sites being those depicted in Figure 2 for the basal (0001) surface of the 1T- and 2H-Mo_2C MXenes. Here, all these sites are systematically analyzed on the strained 1T′- and 2H′-Mo_2C MXene surfaces. By this analysis, one the most stable site and molecular conformation are determined.[22−24] Starting with the CO_2 molecule, the calculated adsorption energy, structural features, and topological Bader charge are listed in Table 1. The adsorption of CO_2 is clearly exothermic regardless of the Mo_2C MXene surface considered. This strong chemisorption promotes the elongation of the C−O distance and the O−C−O angle closure with respect to the gas-phase values. Precisely, the structural deformation of the CO_2 molecule has a rather large energy cost which is the reason why the adsorption energy is only moderate. Looking at Figure 2, one can observe that the C atom is well-located over a H site, whereas the O atoms are connected to MXenes with Mo atoms locating on top sites. This flat orientation of the CO_2 molecule promotes the largest adsorption energies in all Mo_2C MXene substrates investigated here. In addition, there is a considerable net electron transfer from the MXene surface toward the CO_2 molecule, which thus becomes the activated $CO_2^{\delta-}$ adsorbed species. Following the cycle-like sequence outlined above when describing the surface models, note that the CO_2 adsorption energy on the 1T-Mo_2C MXene of −1.80 eV decreases to −1.21 eV on the 1T′-Mo_2C MXene because of the compression strain. Going to the 2H-Mo_2C MXene further reduces the adsorption energy to −0.94 eV. Finally, the tensile strain increases, as expected, the activation of the resulting 2H′-Mo_2C with E_{ads} equal to −2.03 eV. In short, the adsorption of CO_2 depends on the structure of the (0001) Mo_2C surface, and the elongation of the C−O distances, the O−C−O angle, and the charge of the CO_2 molecule vary accordingly in a systematic way; see Table 1. The trends for CO_2 do also hold for the rest of probe molecules, easily interpreted in terms of the relative stability of bare models as explained in detail below.

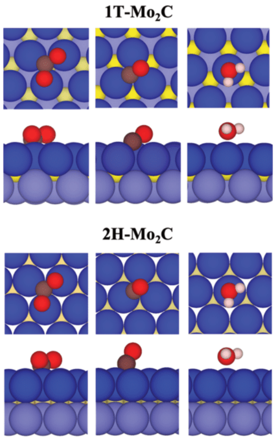

Figure 2. Top (top) and side (bottom) views of the adsorption sites of CO_2, CO, and H_2O species on 1T- and 2H-Mo_2C MXenes. Analogous sites are investigated on 1T′- and 2H′-Mo_2C MXenes. The sequence color of MXene is described in Figure 1. In addition, the brown, white, and red spheres represent carbon, hydrogen, and oxygen atoms, respectively.

Table 2 compiles the set of results for H_2O adsorption in the different models. The H_2O molecule is anchored to the MXene surface on a T site, where the O atom is connected to the Mo atom; see Figure 2. This orientation reports the most favorable adsorption energy. Interestingly, E_{ads} decreases along the 1T−1T′−2H structural path and increases along the 2H−2H′−1T path as for CO_2. However, we note that the adsorption of water could be governed by dispersion because the structure of the H_2O molecule is almost unaltered showing negligible structural variations with respect to the gas molecule. In addition, the charge transfer toward water is almost zero. Finally, the results for the CO molecule are reported in Table 3. The trends for E_{ads} of the CO molecule are once again analogous to those discussed for the CO_2 molecule; see Table 1. Note, however, that the CO adsorption energy is even larger than that of CO_2 on the different Mo_2C MXene surfaces. A

Table 1. Adsorption Energies, E_{ads}, of CO_2 on (0001) Mo_2C MXene Surfaces along with the Most Relevant Structural Features Based on Atomic Distances, *d*, and Angles, ∠[a]

	E_{ads}/eV	d_{C-O}/Å	d_{Mo-O}/Å	d_{Mo-C}/Å	∠OCO/deg	Q/e
1T	−1.80	1.34(×2)	2.08(×2)	1.64	117	−1.27
1T′	−1.21	1.32(×2)	2.11(×2)	1.63	119	−1.24
2H	−0.94	1.31(×2)	2.15(×2)	1.63	121	−1.24
2H′	−2.03	1.32(×2)	2.04(×2)	1.33	115	−1.23
CO_2 (g)		1.18(×2)			180	

[a] The topological Bader charge, Q, is also displayed. The structural parameters of CO_2 in the gas phase are included for comparison.

Table 2. Adsorption Energies, E_{ads}, of H_2O on (0001) Mo_2C MXene Surfaces along with the Most Relevant Structural Features Based on Atomic Distances, *d*, and Angles, ∠[a]

	E_{ads}/eV	d_{H-O}/Å	d_{Mo-O}/Å	∠HOH/deg	Q/e
1T	−0.95	0.98(×2)	2.28	106	−0.01
1T′	−0.72	0.98(×2)	2.32	106	−0.03
2H	−0.63	0.98(×2)	2.36	106	−0.03
2H′	−0.68	0.98(×2)	2.35	106	−0.03
H_2O (g)		0.97(×2)		104	

[a] The topological Bader charge, Q, is also displayed. The structural parameters of H_2O in the gas phase are included for comparison.

Table 3. Adsorption Energies, E_{ads}, of CO on (0001) Mo_2C MXene Surfaces along with the Most Relevant Structural Features Based on Atomic Distances, *d*[a]

	E_{ads}/eV	d_{C-O}/Å	d_{Mo-C}/Å	Q/e
1T	−2.39	1.26	1.97	−0.97
1T′	−2.08	1.19	2.01	−0.63
2H	−1.83	1.19	2.20	−0.66
2H′	−2.51	1.26	1.99	−1.06
CO (g)		1.14		

[a] The topological Bader charge, Q, is also displayed. The structural parameters of CO in the gas phase are included for comparison.

plausible reason comes from the largest cost to distort the CO_2 molecule as depicted clearly in Figure 3. Again, the trend of E_{ads} systematically correlates with the C−O bond distance variations with a clear activation of the molecule *via* charge transfer from Mo_2C MXene surfaces to the CO molecule; see Table 3. Notice that the CO molecule interacts with the Mo_2C MXene surfaces through the C atom on H sites, adopting a flat-like orientation. Before closing this analysis, an important aspect related to the reactivity of the conventional 1T- and 2H-Mo_2C MXenes must be pointed out. Clearly, the adsorption strength is larger on the (0001) 1T-than on 2H-Mo_2C surfaces regardless of the guest molecule. This is directly correlated with the relative stability of the Mo_2C MXene surfaces; the less stable 1T-Mo_2C surface gets partially stabilized by adsorption.

One of the main conclusions till here is that the stacking of the Mo_2C MXene influences the adsorption strength and related properties. Thus, one may wonder whether this can be used as an experimental way to identify the stacking of a synthesized Mo_2C sample. A simple experiment may just involve analyzing the IR or Raman vibrational modes of the selected probe molecules. To this end, Table 4 reports the vibrational analysis of the selected probe molecules including their gas phase and adsorbed configurations on the four (0001) Mo_2C MXene surfaces. For practical purposes, we focus on the 1T- and 2H-Mo_2C surfaces, which may be present in experimental Mo_2C samples based on computational predictions.[19] The results compiled in Table 4 strongly suggest that CO_2 and CO are suitable molecules to identify the Mo_2C stacking based just on the vibrational analysis. Starting with the CO_2 molecule, its asymmetric stretching emerges as a clear way to identify the Mo_2C MXene stacking. This vibrational

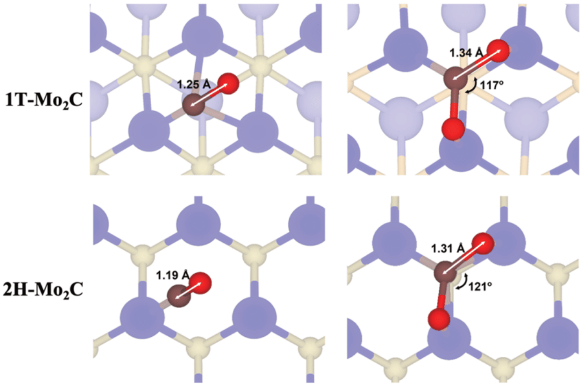

Figure 3. Schematic representation of key structural features of CO and CO_2 adsorbed on the (0001) 1T- and 2H-Mo_2C MXene surfaces. MXene atoms are shadowed for better visibility; color code as in Figure 1.

https://doi.org/10.1021/acs.jpcc.1c07577
J. Phys. Chem. C 2021, 125, 26808−26813

Table 4. Vibrational Modes and Frequencies, in cm^{-1}, of the CO_2, H_2O, and CO Molecules in the Gas Phase and when Adsorbed over (0001) 1T-, 1T′-, 2H-, and 2H′-Mo_2C MXene Surfaces[a]

	gas phase	1T	1T′	2H	2H′
		CO_2			
ν_{as}	2363	1130	1212	1283	1141
Δ		1233	1151	1080	1222
ν_s	1317	1033	1044	1049	1100
Δ		284	273	268	217
δ	635	662	673	674	710
Δ		−27	−38	−39	−75
		H_2O			
ν_{as}	3842	3625	3641	3656	3685
Δ		217	201	186	157
ν_s	3729	3527	3536	3549	3576
Δ		202	193	180	153
δ	1587	1519	1520	1526	1530
Δ		68	67	61	57
		CO			
ν_s	2131	1465	1795	1773	1439
Δ		666	336	358	692

[a] The ν_{as}, ν_s, and δ notations correspond to the asymmetric, symmetric stretching, and bending modes. Δ is the difference between gas phase and adsorbed vibrational modes.

mode of the adsorbed CO_2 decreases its value by 1000 cm^{-1} with respect to its gas-phase counterpart. More importantly, the asymmetric stretching of the adsorbed CO_2 molecule on the 1T- and 2H-Mo_2C MXenes differs by ∼200 cm^{-1}. This difference could be in principle sufficient to distinguish ABC and ABA stackings in Mo_2C MXene samples.

Additionally, the CO symmetric stretching can also be used to identify the stacking structure of these MXenes. Upon adsorption on the 1T- and 2H-Mo_2C surfaces, this mode downshifts by ∼700 and ∼350 cm^{-1} with respect to the gas-phase value, respectively. The difference for the two stacking is ∼300 cm^{-1}, sufficient to identify the MXene stacking and, eventually, to see if both are present in freshly synthetized samples. Nevertheless, apart from exhibiting a noticeable shift, a probe molecule for vibrational spectroscopy must be adsorbed in such a way that the corresponding spectroscopic transition is allowed. In the case of adsorbed CO_2 and CO molecules, the intensity of the corresponding transition fulfils the surface dipole selection rule,[35] also referred to as the metal surface selection rule,[36] as there is at least one component of the dipole moment perpendicular to the surface.[37] This makes these two molecules excellent probe molecules to explore the stacking of MXenes.

4. CONCLUSIONS

A computational study has been carried out to analyze the effect of the stacking layer of MXenes on the adsorption of molecules, with CO_2, H_2O, and CO chosen as examples. Four (0001) Mo_2C MXene surface models have been considered and labeled as 1T, 2H, 1T′, and 2H′. The first two correspond to ABC and ABA stacking layers, whereas the last two are the compressive (1T′) and tensile (2H′) strains of the former, respectively. We have unequivocally shown that the MXene stacking layer influences significantly the adsorption strength of the CO_2, H_2O, and CO molecules which also results in different vibrational shifts with respect to the gas-phase entities. It is suggested that these differences can be used to identify the presence of one, another, or both MXene stackings in the synthesized samples. In particular, the CO_2 asymmetric and the CO symmetric stretching modes emerge as a rather direct and simple way to identify the stacking of Mo_2C as both vibrational transitions will carry considerable intensity.

The present results have been obtained for the Mo_2C MXene, and it is likely that similar conclusions will hold for other MXenes as well. More importantly, this study could be important for experimentalists because spectroscopy measurements would easily identify the MXene stacking layer and observe whether any structural transition takes place when using these materials in practical applications as a sensor or during a given catalytic reaction.

■ AUTHOR INFORMATION

Corresponding Author

Ángel Morales-García − *Departament de Ciència de Materials i Química Física & Institut de Química Teòrica i Computacional (IQTCUB), Universitat de Barcelona, 08028 Barcelona, Spain;* orcid.org/0000-0003-0491-1234; Email: angel.morales@ub.edu

Authors

Anabel Jurado − *Departament de Ciència de Materials i Química Física & Institut de Química Teòrica i Computacional (IQTCUB), Universitat de Barcelona, 08028 Barcelona, Spain*

Francesc Viñes − *Departament de Ciència de Materials i Química Física & Institut de Química Teòrica i Computacional (IQTCUB), Universitat de Barcelona, 08028 Barcelona, Spain;* orcid.org/0000-0001-9987-8654

Francesc Illas − *Departament de Ciència de Materials i Química Física & Institut de Química Teòrica i Computacional (IQTCUB), Universitat de Barcelona, 08028 Barcelona, Spain;* orcid.org/0000-0003-2104-6123

Complete contact information is available at:
https://pubs.acs.org/10.1021/acs.jpcc.1c07577

Notes

The authors declare no competing financial interest.

■ ACKNOWLEDGMENTS

The research carried out at the Universitat de Barcelona has been supported by the Spanish MICIUN/FEDER RTI2018-095460-B-I00 and María de Maeztu MDM-2017-0767 grants and, in part, by Generalitat de Catalunya 2017SGR13 grant and COST Action CA18234. A.M.-G. is thankful to the Juan de la Cierva Incorporación postdoctoral grant IJCI-2017-31979.

■ REFERENCES

(1) Naguib, M.; Kurtoglu, M.; Presser, V.; Lu, J.; Niu, J.; Heon, M.; Hultman, L.; Gogotsi, Y.; Barsoum, M. W. Two-Dimensional Nanoscrystals Produced by Exfoliation of Ti_3AlC_2. *Adv. Mater.* **2011**, *23*, 4248−4253.

(2) Naguib, M.; Barsoum, M. W.; Gogotsi, Y. Ten Years of Progress in the Synthesis and Development of MXenes. *Adv. Mater.* **2021**, *33*, 2103393.

(3) VahidMohammadi, A.; Rosen, J.; Gogotsi, Y. The World of Two-Dimensional Carbides and Nitrides (MXenes). *Science* **2021**, *372*, No. eabf1581.

(4) Sinha, A.; Dhanjai; Zhao, H.; Huang, Y.; Lu, X.; Chen, J.; Jain, R. MXene: An Emerging Material for Sensing and Biosensing. *Trends Anal. Chem.* **2018**, *105*, 424−435.

(5) Hart, J. L.; Hantanasirisakul, K.; Lang, A. C.; Anasori, B.; Pinto, D.; Pivak, Y.; van Omme, J. T.; May, S. J.; Gogotsi, Y.; Taheri, M. L. Control of MXenes Electronic Properties Through termination and Intercalation. *Nat. Commun.* **2019**, *10*, 522.

(6) Anasori, B.; Lukatskaya, M. R.; Gogotsi, Y. 2D Metal Carbides and Nitrides (MXenes) for Energy Storage. *Nat. Rev. Mater.* **2017**, *2*, 16098.

(7) Handoko, A. D.; Steinmann, S. N.; Seh, Z. W. Theory-Guided Materials Design: Two-Dimensional MXenes in Electro- and Photocatalysis. *Nanoscale Horiz.* **2019**, *4*, 809−827.

(8) Morales-García, Á.; Calle-Vallejo, F.; Illas, F. MXenes: New Horizons in Catalysis. *ACS Catal.* **2020**, *10*, 13487−13503.

(9) Alhabeb, M.; Maleski, K.; Anasori, B.; Lelyukh, P.; Clark, L.; Sin, S.; Gogotsi, Y. Guidelines for Synthesis and Processing of Two-Dimensional Titanium Carbide ($Ti_3C_2T_x$ MXene). *Chem. Mater.* **2017**, *29*, 7633−7644.

(10) Kamysbayev, V.; Filatov, A. S.; Hu, H.; Rui, X.; Lagunas, F.; Wang, D.; Klie, R. F.; Talapin, D. V. Covalent Surface Modifications and Superconductivity of Two-Dimensional Metal Carbide MXenes. *Science* **2020**, *369*, 979−983.

(11) Seredych, M.; Shuck, C. E.; Pinto, D.; Alhabeb, M.; Precetti, E.; Deysher, G.; Anasori, B.; Kurra, N.; Gogotsi, Y. High-Temperature Behavior and Surface Chemistry of Carbide MXenes Studied by Thermal Analysis. *Chem. Mater.* **2019**, *31*, 3324−3332.

(12) Persson, I.; Halim, J.; Lind, H.; Hansen, T. W.; Wagner, J. B.; Näslund, L.-Å.; Darakchieva, V.; Palisaitis, J.; Rosen, J.; Persson, P. O. Å. 2D Transition Metal Carbides (MXenes) for Carbon Capture. *Adv. Mater.* **2019**, *31*, 1805472.

(13) Hong, W.; Wyatt, B. C.; Nemani, S. K.; Anasori, B. Double Transition-Metal MXenes: Atomistic Design of Two-Dimensional Carbides and Nitrides. *MRS Bull.* **2020**, *45*, 850−861.

(14) Tao, Q.; Dahlqvist, M.; Lu, J.; Kota, S.; Meshkian, R.; Halim, J.; Palisaitis, J.; Hultman, L.; Barsoum, M. W.; Persson, P. O. Å.; Rosen, J. Two-Dimensional $Mo_{1.33}C$ MXene with Divacancy Ordering Prepared from Parent 3D Laminate With in-plane Chemical Ordering. *Nat. Commun.* **2017**, *8*, 14949.

(15) Anasori, B.; Xie, Y.; Beidaghi, M.; Lu, J.; Hosler, B. C.; Hultman, L.; Kent, P. R. C.; Gogotsi, Y.; Barsoum, M. W. Two-Dimensional, Ordered, Double Transition Metals Carbides (MXenes). *ACS Nano* **2015**, *9*, 9507−9516.

(16) Dolz, D.; Morales-García, Á.; Viñes, F.; Illas, F. Exfoliation Energy as a Descriptor of MXenes Synthesizability and Surface Chemical Activity. *Nanomaterials* **2021**, *11*, 127.

(17) Morales-García, Á.; Mayans, M.; Viñes, F.; Illas, F. Thickness Biased Capture of CO_2 on Carbide MXenes. *Phys. Chem. Chem. Phys.* **2019**, *21*, 23136−23142.

(18) Li, X.; Huang, Z.; Zhi, C. Environmental Stability of MXenes as Energy Storage Materials. *Front. Mater.* **2019**, *6*, 312.

(19) Gouveia, J. D.; Viñes, F.; Illas, F.; Gomes, J. R. B. MXenes Atomic Layer Stacking Phase Transitions and Their Chemical Activity Consequences. *Phys. Rev. Mater.* **2020**, *4*, 054003.

(20) Shao, M.; Shao, Y.; Chen, W.; Ao, K. L.; Tong, R.; Zhu, Q.; Chan, I. N.; Ip, W. F.; Shi, X.; Pan, H. Efficient Nitrogen Fixation to Ammonia on MXenes. *Phys. Chem. Chem. Phys.* **2018**, *20*, 14504−14512.

(21) Urbankowski, P.; Anasori, B.; Hantanasirisakul, K.; Yang, L.; Zhang, L.; Haines, B.; May, S. J.; Billinge, S. J. L.; Gogotsi, Y. 2D Molybdenum and Vanadium Nitrides Synthesized by Ammoniation of 2D Transition Metal Carbides (MXenes). *Nanoscale* **2017**, *9*, 17722−17730.

(22) Morales-García, Á.; Fernández-Fernández, A.; Viñes, F.; Illas, F. CO_2 Abatement Using Two-Dimensional MXene Carbides. *J. Mater. Chem. A* **2018**, *6*, 3381−3385.

(23) Gouveia, J. D.; Morales-García, Á.; Viñes, F.; Illas, F.; Gomes, J. R. B. MXenes as Promising Catalysts for Water Dissociation. *Appl. Catal., B* **2020**, *260*, 118191.

(24) Morales-Salvador, R.; Gouveia, J. D.; Morales-García, Á.; Viñes, F.; Gomes, J. R. B.; Illas, F. Carbon Capture and Usage by MXenes. *ACS Catal.* **2021**, *11*, 11248−11255.

(25) Wang, R.; Yu, Y.; Zhou, S.; Li, H.; Wong, H.; Luo, Z.; Gan, L.; Zhai, T. Strategies on Phase Control in Transition Metal Dichalcogenides. *Adv. Funct. Mater.* **2018**, *28*, 1802473.

(26) Morales-García, Á.; Viñes, F.; Gomes, J. R. B.; Illas, F. Concepts, models and methods in computational heterogeneous catalysis illustrated through CO_2 conversion. *Wiley Interdiscip. Rev.: Comput. Mol. Sci.* **2021**, *11*, No. e1530.

(27) Blöchl, P. E. Projector Augmented-Wave Method. *Phys. Rev. B: Condens. Matter Mater. Phys.* **1994**, *50*, 17953.

(28) Monkhorst, H. J.; Pack, J. D. Special Points for Brillouin-Zone Integrations. *Phys. Rev. B: Solid State* **1976**, *13*, 5188−5192.

(29) Perdew, J. P.; Burke, K.; Ernzerhof, M. Generalized Gradient Approximation Made Simple. *Phys. Rev. Lett.* **1996**, *77*, 3865.

(30) Grimme, S.; Antony, J.; Ehrlich, S.; Krieg, H. A Consistent and Accurate Ab Initio Parametrization of Density Functional Dispersion Correction (DFT-D) for the 94 elements H-Pu. *J. Chem. Phys.* **2010**, *132*, 154104.

(31) Janthon, P.; Kozlov, S. M.; Viñes, F.; Limtrakul, J.; Illas, F. Establishing the Accuracy of Broadly Used Density Functionals in Describing Bulk Properties of Transition Metals. *J. Chem. Theory Comput.* **2013**, *9*, 1631−1640.

(32) Vega, L.; Ruvireta, J.; Viñes, F.; Illas, F. Jacob's Ladder as Sketched by Escher: Assessing the Performance of Broadly Used Density Functionals on Transition Metal Surface Properties. *J. Chem. Theory Comput.* **2018**, *14*, 395−403.

(33) Vega, L.; Viñes, F. Generalized gradient approximation adjusted to transition metals properties: Key roles of exchange and local spin density. *J. Comput. Chem.* **2020**, *41*, 2598−2603.

(34) Kresse, G.; Furthmüller, J. Efficient Iterative Schemes for Ab Initio Total-Energy Calculations Using a Plane-Wave Basis Set. *Phys. Rev. B: Condens. Matter Mater. Phys.* **1996**, *54*, 11169.

(35) Greenler, R. G. Infrared Study of Adsorbed Molecules on Metal Surfaces by Reflection Techniques. *J. Chem. Phys.* **1966**, *44*, 310.

(36) Pearce, H. A.; Sheppard, N. Possible Importance of a "Metal-Surface Selection Rule" in the Interpretation of the Infrared Spectra of Molecules Adsorbed on Particulate Metals; Infrared Spectra from Ethylene Chemisorbed on Silica-Supported Metal Catalysts. *Surf. Sci.* **1976**, *59*, 205.

(37) Valcárcel, A.; Ricart, J. M.; Illas, F.; Clotet, A. Theoretical Interpretation of the IR Spectrum of Propyne Cu(111). *J. Phys. Chem. B* **2004**, *108*, 18297.

5.4 Conclusions

The effect of the stacking on carbide MXenes, taking Mo_2C MXene as a case of study is investigated through the adsorption of probe molecules as CO_2, CO, and H_2O. Calculations show that the stacking influences on the resulting adsorption, and, in turn, the changes of the vibrational modes are relatively enough to distinguish the MXene stackings, ABA and ABC. In summary, the following conclusions can be extracted:

- The difference between the four models is noticeable *e.g.*, -1.80 eV (ABC) and -2.03 eV (ABA), concluding that depends on the structure of the surface.
- The interaction of CO_2 shows an exothermic adsorption in the four surfaces. These trends are shared also with the CO molecule but not with H_2O, that changes are negligible due to the fact that the molecule is governed by the dispersion.
- The results present distinguishable vibrational modes between structures *e.g.*, the asymmetric stretching the CO_2 molecule differs by ~200 cm^{-1} between ABC and ABA structures. This concludes that the MXene stacking can be distinguished indirectly by analysing the vibrational modes of activated molecules.

5.5 References

1. Naguib, M.; Kurtoglu, M.; Presser, V.; Lu, J.; Niu, J.; Heon, M.; Hultman, L.; Gogotsi, Y.; Barsoum, M. W. Two-Dimensional Nanoscrystals Produced by Exfoliation of Ti_3AlC_2. *Adv. Mater.*, **2011**, 23, 4248−4253.
2. Li, X.; Huang, Z.; Zhi, C. Environmental Stability of MXenes as Energy Storage Materials. *Front. Mater.*, **2019**, 6, 312.
3. Gouveia, J. D.; Viñes, F.; Illas, F.; Gomes, J. R. B. MXenes Atomic Layer Stacking Phase Transitions and their Chemical Activity Consequences. *Phys. Rev. Mater.*, **2020**, 4, 054003.

CHAPTER SIX

The Reverse Water Gas Shift Reaction on MXenes

Chapter 6

6.1 Introduction

There is no doubt about the urgency to reduce anthropogenic CO_2 through CCU and CCS technologies. Transition metal carbides (TMCs) such as Ti_2C and Mo_2C,[1] have shown a good performance towards catalysis and their bidimensional counterparts, MXenes, share these properties. Thereby, the good performance of CO_2 activation on bare MXenes[2] and the low energy barriers on H_2 dissociation,[3] opens the possibility to use these materials as catalysts for the capture and transformation of CO_2 molecule in the Reverse Water Gas Shift Reaction. Thus, in this Chapter, Mo_2C MXene has shown promising results emerging as a candidate as catalyst.

To carry out these investigations, the RWGS reaction is investigated through periodic density functional based calculations where the search of transition states went through climbing-image nudged elastic band (CI-NEB)[4] and the Dimer methods.[5] This thermodynamic and kinetic information allow us to access to the microkinetic modelling to the identification of the rate-limiting elementary steps is carried out using the MKMCXX[6] program and finally, the obtaining of the free-energy profile through AIAT framework.

6.2 Main results

To analyse the Reverse Water Gas Shift reaction on the Mo_2C MXene, the adsorption energies of reactants (CO_2 and H_2), products (CO and H_2O) and intermediates (H, O, HCOO, tCOOH, cCOOH, COH, HCO, and OH) are calculated and ZPE corrected. Thus, the most stable conformations are shown in the Figure 6.1.

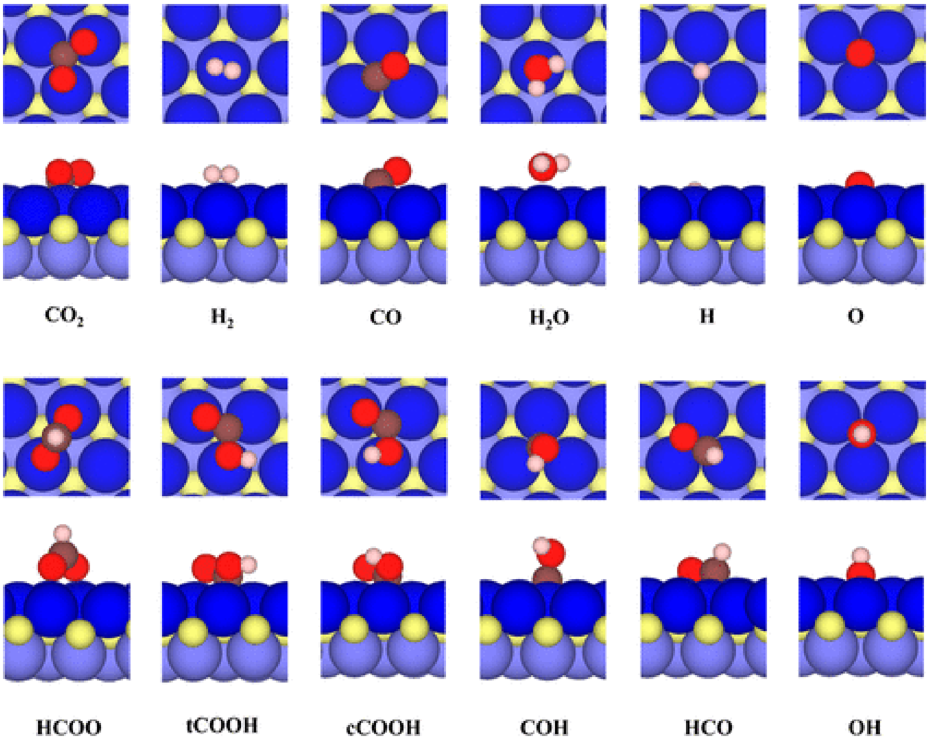

Figure 6.1. CO_2, H_2, CO, H_2O, H, O, HCOO, tCOOH, cCOOH, COH, HCO, and OH most stable adsorption sites on the Mo_2C MXene (0001) surface. In addition, dark and light blue spheres represent the molybdenum atoms, yellow sphere the carbon atom of the MXene and the brown, white, and red spheres represent carbon, hydrogen, and oxygen atoms, respectively.

The Reverse Water Gas Shift reaction is an endothermic process with an experimental value of 0.42 eV or 40.52 kJ mol^{-1}.[7] The comparison of this value with the obtained through the gas phase calculation, 0.85 eV, shows a noticeable deviation that can be corrected by accounting for DFT systematic errors on the energy of gas phase molecules. Thus, the final value is 0.42 eV, matching the experimental value. However, being and endothermic process, the reaction needs high temperature to work through the formation of CO and H_2O. Performing the Gibbs free energy at 700 K and partial pressures of 1 bar, the value becomes ΔG = -0.09 eV.

It is important to note that the Reverse Water Gas Shift exhibits three different mechanisms throughout it can work: redox, HCOO and, COOH path. Thus, the redox route follows the $1 \rightarrow 2 \rightarrow 5 \rightarrow 6 \rightarrow 7 \rightarrow 8 \rightarrow 3 \rightarrow 4$ sequence; formate route and carboxyl routes imply the $1 \rightarrow 2 \rightarrow 9 \rightarrow 10 \rightarrow 11 \rightarrow 7 \rightarrow 8 \rightarrow 3 \rightarrow 4$ and $1 \rightarrow 2 \rightarrow 12 \rightarrow 13 \rightarrow 14 \rightarrow 15 \rightarrow 7 \rightarrow 8 \rightarrow 3 \rightarrow 4$ sequences, respectively, see Table 6.1

Step	**Elementary reaction step**	**Forward**			**Backward**		
		$E_{a(i)}$	A_i	ΔE	$E_{a(i)}$	A_i	ΔE
1	CO_2 (g) → CO_2*	—	—	-1.65	—	—	1.65
2	H_2 (g)→H_2*	—	—	-0.85	—	—	0.85
3	CO* → CO (g)	—	—	1.92	—	—	-1.92
4	H_2O* → H_2O (g)	—	—	0.94	—	—	-0.94
5	H_2*→2 H*	0.01	8.35×10^{12}	-0.81	0.93	8.88×10^{13}	0.81
6	CO_2* → CO*+ O*	0.47	4.31×10^{13}	-1.43	1.90	8.86×10^{12}	1.43
7	O*+ H* → OH*	1.59	1.99×10^{13}	0.88	0.70	1.67×10^{13}	-0.88
8	OH* + H*→ H_2O*	1.68	3.04×10^{14}	1.36	0.32	1.15×10^{13}	-1.36
9	CO_2*+ H* → HCOO*	0.56	2.34×10^{14}	0.08	0.48	7.49×10^{13}	-0.08
10	HCOO* → HCO* + O*	0.29	3.03×10^{13}	-1.00	1.30	4.53×10^{13}	1.00
11	HCO*→ H*+ CO*	0.36	1.67×10^{13}	-0.50	0.86	1.99×10^{13}	0.50
12	CO_2*+ H* → tCOOH*	0.84	7.93×10^{13}	0.83	0.01	4.40×10^{13}	-0.83
13	tCOOH* → cCOOH*	0.27	2.09×10^{13}	-0.75	1.02	2.53×10^{13}	0.75
14	cCOOH* → COH* + O*	1.30	1.32×10^{13}	-0.81	1.43	2.00×10^{12}	0.81
15	COH* → CO* + H*	0.62	1.50×10^{13}	-1.40	1.43	2.03×10^{13}	1.40

Table 6.1 Elementary Reaction Steps of the RGWS Reaction.

Regarding the redox path from the Gibbs free energy profile, the reaction starts with the adsorption of the CO_2 molecule and the H_2 dissociation to 2 H* adatoms. Next step is the dissociation of CO_2 adsorbed molecule into CO* and O*, being a 0.47 eV the barrier for it. Thus, the rest of the mechanism involves the formation of water from the O* and H*, requiring overcoming a barrier of 1.59 eV to form OH* and 1.68 eV to form H_2O* from OH* + H*. Therefore, these reactions are the determining steps of the redox route.

The formate path starts equal to the redox with the adsorption of the CO_2 molecule and the H_2 dissociation to 2 H* adatoms. However, the hydrogenation of the CO_2 molecule is the following step, being the energy barrier slightly small, 0.56 eV. The following steps are the dissociation of HCOO* to HCO* and O* and finally, CO* , O* and H*. being the determining steps the same as the redox route, the formation of OH* and the consequent H_2O*.

The last mechanism, the carboxyl path proceeds with the adsorption of the CO_2 molecule and the H_2 dissociation to 2 H* adatoms, followed by the hydrogenation of CO_2 into t-COOH* with an energy barrier of 0.84 eV. Here, there is a conformational transition toward *c*-COOH with an energy barrier of 0.27 eV. The following steps are the dissociation into COH* and O* and later, into CO* and H* , being the energy barriers 1.30 and 0.62 eV, respectively.

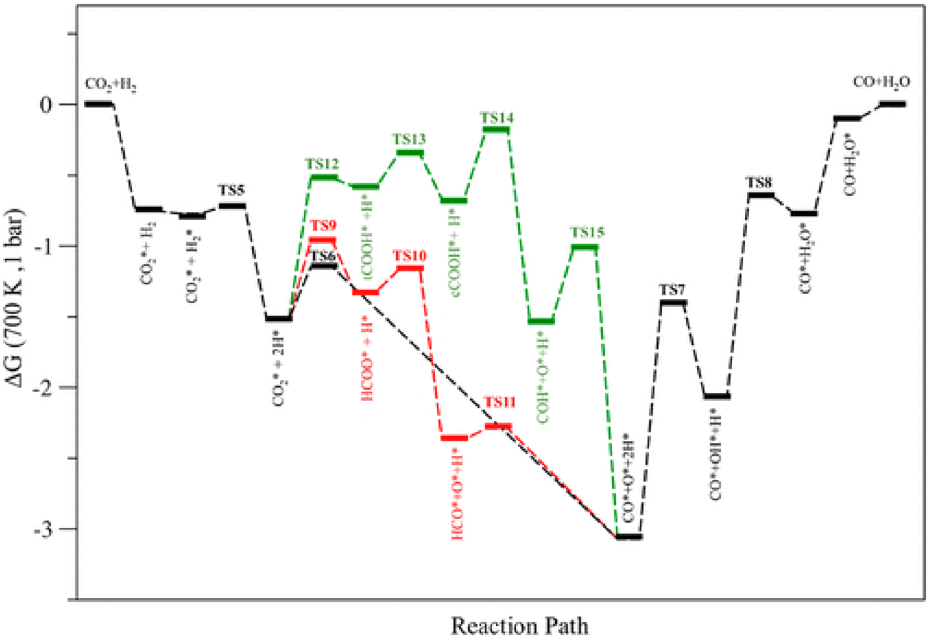

Figure 6.2. Gibbs free energy, Δ*G*, given in eV, profile of the redox (black), HCOO (red), and COOH (green) route mechanisms for the RWGS reaction on the Mo_2C MXene (0001) surface.

With the values of table 6.1, using different temperature and pressure working conditions, (300 to 850 K and 1 to 10 bar) and and different feed (H_2/CO_2 ratios of 2:1, 1:1, and 1:2) i the microkinetic analysis using the MXene Mo_2Cas catalyst is performed.

The variation of surface coverage reveals that the formation of CO product is observed above 350 K, being from the route of the HCO decomposition, or through the redox mechanism. However, results show that whereas the HCOO route progresses beyond 200 K, redox path is only available when H* decreases, being a possible reason that the lateral interactions between H* are negligible and CO_2 dissociation is inhibited, see Figure 6.3.

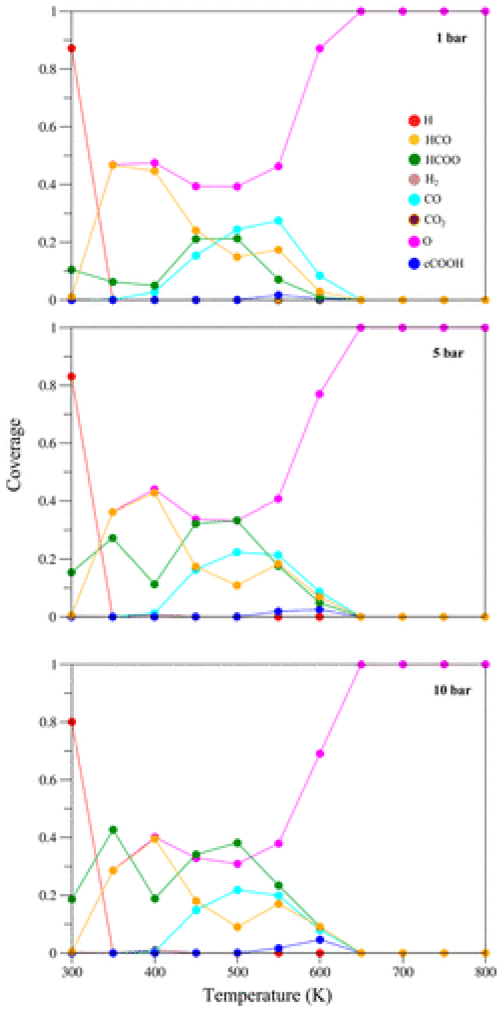

Figure 6.3 Surface coverage variation with the temperature for the RWGS reaction species on the Mo_2C MXene (0001) surface at three different total pressures: 1, 5, and 10 bar, s in top, middle, and bottom panels. The selected feed ratio is H_2/CO_2 2:1.

Finally, analysing the turnover frequency, the measure of the instantaneous efficiency of the Mo_2C MXene as a catalyst is carried out. Results show that the CO production is slightly higher than the exhibited by H_2O, and that to obtain reasonable TOF values of this molecule, higher temperatures are required. This is due to the energy barriers of the OH* and H_2O formation. Thus, focusing on the CO production with

CO_2/H_2 1:2 ratio, the highest production appears at ~600K where the surface is partially covered by CO* species. However, this particular production is not affected by the ratio or the total pressure, being only affected regions where the TOF has lower values, being more favourable when the presence of H_2 is higher.

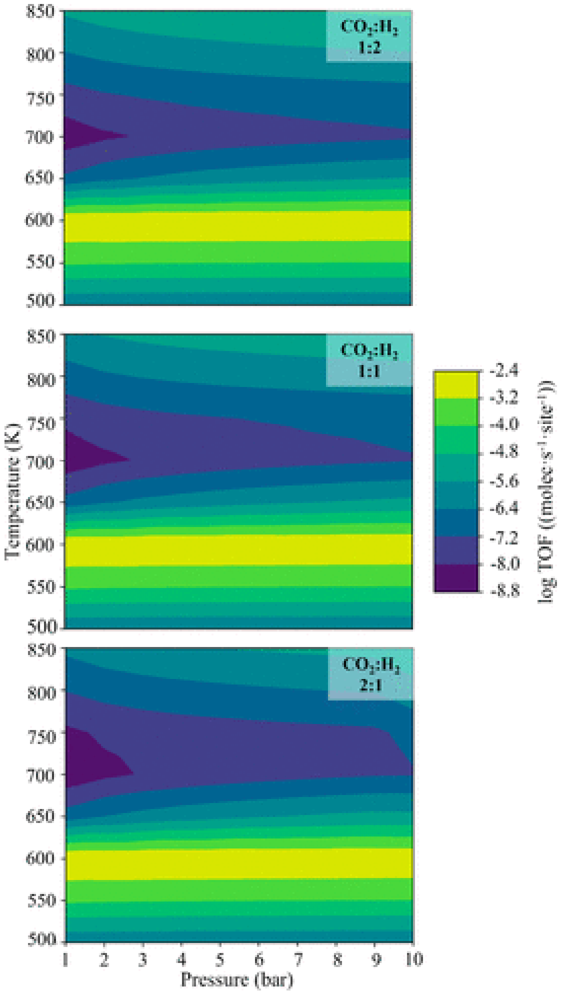

Figure 6.4 Heating map of TOF under different working conditions of pressure and temperature on the (0001) Mo_2C MXene surface for the CO production. Pressure, temperature, and TOF are bar, K, and molecules·site^{-1}·s^{-1}, respectively. The TOF scale corresponds to the common logarithm with base 10.

6.2 Publication 3

Molecular Mechanism and Microkinetic Analysis of the Reverse Water Gas Shift Reaction Heterogeneously Catalyzed by the Mo_2C MXene

ACS Catalysis

pubs.acs.org/acscatalysis

Research Article

Molecular Mechanism and Microkinetic Analysis of the Reverse Water Gas Shift Reaction Heterogeneously Catalyzed by the Mo_2C MXene

Anabel Jurado, Ángel Morales-García,* Francesc Viñes, and Francesc Illas*

Cite This: *ACS Catal.* 2022, 12, 15658−15667

Read Online

ACCESS | Metrics & More | Article Recommendations | Supporting Information

ABSTRACT: The potential of the Mo_2C MXene to catalyze the reverse water gas shift (RWGS) reaction has been investigated by a combination of density functional theory (DFT)-based calculations, atomistic thermodynamics, and microkinetic simulations. Different catalytic routes are explored including redox and associative (carboxyl and formate) mechanisms at a high temperature at which the RWGS reaction is exothermic. The present study predicts that, on the Mo_2C MXene, the RWGS reaction proceeds preferentially through the redox and formate catalytic routes, the rate-limiting step being the formation of the OH intermediate followed by the H_2O formation, whereas the carboxyl route to form the carboxyl intermediate is hindered by a large energy barrier. Microkinetic simulations confirm the formation of carbon monoxide (CO) under relatively mild conditions (i.e., ∼400 °C and 1 bar). The CO formation is not affected either by the total pressure or by the CO_2/H_2 ratio. However, water formation requires high temperatures of ∼700 °C and pressures above 5 bar. In addition, an excess of hydrogen in the CO_2/H_2 ratio favors water formation. Shortly, the present study confirms that the Mo_2C MXene emerges as a heterogeneous catalyst candidate for generating a CO feedstock that can be used for subsequent transformation into methanol through the Fischer−Tropsch process.

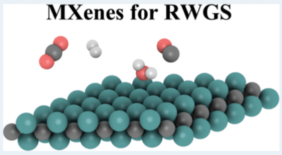

KEYWORDS: *Mo_2C, MXene, reverse water gas shift, density functional theory, microkinetics*

1. INTRODUCTION

Catalysis has generated a great impact in the human societies being at the forefront of addressing fundamental challenges in climate change, sustainable energy, and food supply.[1] To date, more than 80% of all chemical products in the world are produced via heterogeneous catalysis. Henceforth, the design and development of new robust and selective catalysts continue being imperative to maintain the present welfare state.[2] In this context, new catalysts with high affinity for carbon dioxide (CO_2) are demanded with the goal of development technologies for capturing and utilizing CO_2.[3,4]

In principle, high-volume chemicals can be produced from CO_2 through carbon capture and utilization (CCU) strategies by using a specific heterogeneous catalyst: the dry reforming of methane (DRM) or ethanol (DRE), methanol synthesis, the CO_2 methanation (known as Sabatier reaction), and the reverse water gas shift (RWGS) reactions are some examples of heterogeneous catalytic reactions where the CO_2 is transformed into chemicals or hydrocarbon fuels. Especially interesting is the RWGS reaction: $CO_2 + H_2 \rightarrow CO + H_2O$. This is a fundamental step providing a CO feedstock for methanol synthesis through the efficient Cu/ZnO catalysts with possible subsequent transformation to acetic acid through the Monsanto/Cativa process or to hydrocarbon through the Fischer−Tropsch synthesis. Due to the large impact of the RWGS reaction in heterogeneous catalysis, several catalysts have been investigated and developed. Initially, reduced inorganic oxides such as CeO_2, ZnO, Al_2O_3, Fe_2O_3, or MnO_2 were used.[5−7] However, such oxides present drawbacks as low CO_2 activation and easy sintering. To overcome these limitations, composite oxides, spinel oxides, solid solution oxides, and perovskite-type oxides have been investigated showing a structural stability and reverse oxygen storage to increase RWGS performance.[8−11] In addition, supported metal catalysts involving for instance Pt, Pd, or Au anchored onto the metal oxide support material facilitate the CO_2 activation in the metal/oxide interfaces making suitable catalysts for the RGWS reaction,[12,13] although there is clear room for improvement.

In this quest for heterogeneous catalysts for the RWGS, transition metal carbides (TMCs) emerged as a possible alternative due to their similar properties to precious metal-based catalysts.[14] The incorporation of carbon in the metal lattice induces new chemistry from the metallic counterparts affecting to the binding energy and the reactivity of adsorbates.[15] Particularly, Mo_2C is interesting for CO_2

Received: September 12, 2022
Revised: November 22, 2022
Published: December 6, 2022

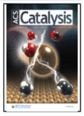

conversion because of its good performance for H_2 dissociation and CO bond scission, two key chemical aspects required in the RWGS reaction.[16−18] During this process, the dissociation of CO_2 into CO + O, the formation of oxycarbide species, and the facile removal of oxygen from the Mo_2C surface by H_2 were found to be the key steps for achieving high activity, selectivity, and stability of Mo_2C.

Recently, low-dimensional carbides known as MXenes have been successfully synthetized.[19,20] MXenes are produced through a top-down synthesis procedure from layered ternary materials known MAX phases with the chemical formula $M_{n+1}AX_n$ (n = 1−3), where M is an early transition metal, A represents XIII- and XIV-group elements, and X stands for C and/or N atoms. The M−A chemical bond is susceptible to chemical etchant agents promoting the disassembly of the MAX phase and forming the $M_{n+1}X_nT_x$ or MXene phases. Normally, the as-synthetized MXene phases are functionalized depending on the etchant employed in the chemical exfoliation. Such functionalization is represented by the T_x term, where x indicates a non-stoichiometric termination. HF, LiF/HCl, or NH_4HF_2 are the most regular etchants employed to break the M−A bond.[21] Although this top-down procedure drives to functionalized MXenes, recent work reported a strategy combining high-temperature and hydrogenation reaction to generate defunctionalized (clean or bare) MXenes.[22] In addition, new synthetic routes using alkali halides as etchant agents lead to produce MXene with not so strong bonded halide (T_x = Cl or Br) that further facilitates the generation of bare MXenes.[23]

Bare MXenes have been predicted to exhibit an outstanding performance in the activation of the CO_2 molecule, later confirmed by experiments.[22,24,25] These results demonstrate the feasibility of these MXene materials for carbon capture and storage (CCS) procedures. However, clean MXenes result even more interesting because they can dissociate CO_2 into CO + O requiring energy barriers below 0.6 eV that makes them also appropriate candidates for CCU.[26] Furthermore, MXenes easily dissociate H_2 with almost negligible barriers.[27] Thus, MXenes meet the main conditions of suitable substrates for the RWGS reaction. In addition, MXenes preserve the physical and chemical properties of their 3D carbide counterparts together with a large surface area, as described recently in detail by some of us.[28] Furthermore, experimental analysis has confirmed the stability of Ti_3C_2 MXene up to 800 °C.[29]

To assess the suitability of MXene as candidate heterogeneous catalysts for the RWGS reaction, we present a multiscale analysis on the bare Mo_2C MXene phase with an ABC stacking.[30] This choice is based on a prescreening step evidencing that this particular MXene exhibits moderate binding energies of reactant and intermediates that make feasible the progression of the reaction. Furthermore, its choice is based on the good performance of its bulk Mo_2C counterpart.[31] The present study combines first-principles calculations and microkinetic simulations to investigate in detail the mechanisms of the RWGS reaction via redox and associative routes, see Figure 1.[7] Noting that associative routes involve the formation of carbon-containing intermediates, namely, formate and carboxyl.

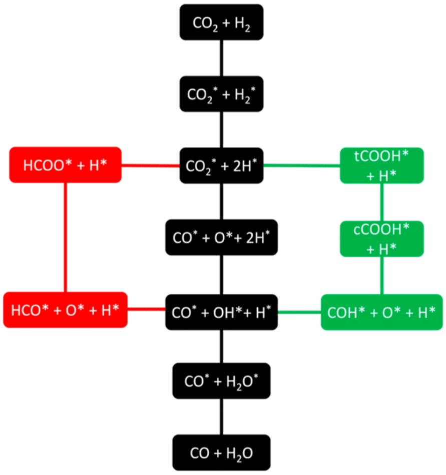

Figure 1. Scheme of the investigated RWGS reaction sequences including redox (black), associative carboxyl, that is, COOH (green), and associative formate, that is, HCOO (red).

2. COMPUTATIONAL DETAILS AND MATERIALS MODELS

The present study combines periodic density functional theory (DFT)-based calculations and microkinetic simulations. The DFT calculations are carried out by means of the Vienna Ab Initio Simulation Package (VASP)[32] with exchange and correlation effects accounted through a generalized gradient approximation (GGA) as described by the Perdew−Burke−Ernzerhof (PBE) density functional.[33] Furthermore, the dispersion interactions were included through Grimme's D3 approach.[34] A cutoff energy of 415 eV were selected to expand the valence electron density using a plane-wave basis set, whereas the effect of the core electrons on the valence density was described using the projector augmented wave (PAW) method.[35] For the unit cell described below, the numerical integration in the reciprocal space was carried out using a **Γ**-centered 5 × 5 × 1 ***k***-point grid in the Brillouin zone. The convergence threshold for the geometry optimization calculations is reached when the forces on all atoms are below 0.01 $eV \cdot Å^{-1}$ and the relaxation of the electronic degrees of freedom steps is 10^{-6} eV. Note that this computational scheme has been used in previous works, reporting results with accuracy below 0.04 eV.[24−29]

The RWGS reaction is studied using a $p(3 \times 3)$ supercell representing the basal (0001) plane of Mo_2C with an ABC stacking of the atomic layers, see Figure 2. Larger supercells give similar results to the $p(3 \times 3)$ supercell used in the present work. Looking at the top side of the MXene surface, one may identify easily four high-symmetry sites including on-top of a surface Mo site (T), bridging two vicinal surface Mo sites (B), and two threefold hollow sites involving three surface Mo atoms, having one Mo atom two layers underneath (H_M), or one C atom a layer underneath (H_C). The slabs are separated by a vacuum of at least 10 Å in the [0001] direction to vanish the interaction between the periodic replicas as the model used

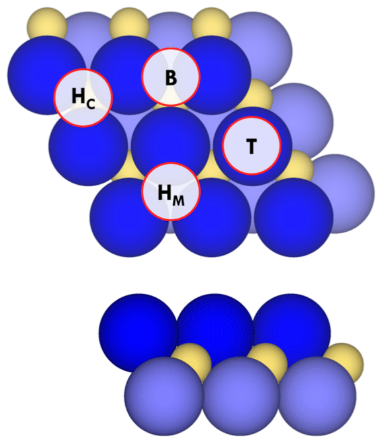

Figure 2. Top (top) and side (bottom) views of the Mo_2C (0001) surface $p(3 \times 3)$ supercell. C atoms are represented by yellow spheres, while Mo atoms are represented by dark and light blue spheres to distinguish upmost and bottommost layers. The four relevant high-symmetry sites are depicted as T, B, H_M, and H_C labels identifying top, bridge, hollow metal, and hollow carbon sites, respectively.

is periodic in the three dimensions of space. The adsorption energy, E_{ads}, of the reactants and products, denoted by the term of species, is calculated as

$$E_{ads} = E_{species@Mo_2C} - (E_{species} + E_{Mo_2C}) + \Delta ZPE \qquad (1)$$

where $E_{species@Mo_2C}$ is the total energy of the corresponding species adsorbed, that is, reactants or products, on the Mo_2C MXene, $E_{species}$ stands for their energy in gas phase, while E_{Mo_2C} corresponds to the energy of the pristine MXene slab model. The $E_{species}$ is calculated isolating the species in an asymmetric box with 10 × 11 × 12 Å dimensions and considering the **Γ**-point only. The term ΔZPE stands for the difference in the zero-point energy contribution between the adsorbed and phase gas species. This term is obtained directly from the vibrational frequencies in gas phase and those vibrational modes once the species is anchored to the surface. The latter includes the vibrational modes coming from the frustrated translational and rotational degrees of freedom; see Table S1 in the Supporting Information. The frequencies are obtained by diagonalization of the corresponding block of the Hessian matrix with elements computed as finite differences of analytical gradients with displacements of 0.03 Å. In all cases, calculations were sufficiently refined to ensure that all adsorbed species exhibit real frequencies and transition states only one imaginary frequency corresponding to the reaction coordinate.

The search for the transition states (TSs) of each step listed in Table 1 was carried out using climbing-image nudged elastic band (CI-NEB) and dimer methods, the former including five intermediate images and minimizing forces acting on atoms below 0.03 eV·Å^{-1}.[36,37] Frequency analyses was carried out over the located TS structures to ensure that just one imaginary frequency was identified along the reaction pathway. In each step, the initial atomic configurations used to locate TSs were the most stable adsorption configuration. The activation energy barrier, E_a, is thus calculated as the difference between the TS and the initial configuration, and its energy includes the ZPE contribution. All these minima and reaction step energy barriers allow one outlining the free-energy profile along the coordination reaction at certain temperature and gas pressure using the Ab initio thermodynamics (AIAT) framework.[38]

The identification of reaction intermediates and rate-limiting elementary reaction of the RWGS reaction is carried out using

Table 1. Elementary Reaction Steps of the RGWS Reaction[a]

		forward			backward	
step	elementary reaction step	$E_{a,i}$	A_i	ΔE	$E_{a,i}$	A_i
1	$CO_2(g) \rightarrow CO_2^*$					
2	$H_2(g) \rightarrow H_2^*$					
3	$CO^* \rightarrow CO(g)$					
4	$H_2O^* \rightarrow H_2O(g)$					
5	$H_2^* \rightarrow 2H^*$	0.01	8.35×10^{12}	−0.81	0.93	8.88×10^{13}
6	$CO_2^* \rightarrow CO^* + O^*$	0.47	4.31×10^{13}	−1.43	1.90	8.86×10^{12}
7	$O^* + H^* \rightarrow OH^*$	1.59	1.99×10^{13}	0.88	0.70	1.67×10^{13}
8	$OH^* + H^* \rightarrow H_2O^*$	1.68	3.04×10^{14}	1.36	0.32	1.15×10^{13}
9	$CO_2^* + H^* \rightarrow HCOO^*$	0.56	2.34×10^{14}	0.08	0.48	7.49×10^{13}
10	$HCOO^* \rightarrow HCO^* + O^*$	0.29	3.03×10^{13}	−1.00	1.30	4.53×10^{13}
11	$HCO^* \rightarrow H^* + CO^*$	0.36	1.67×10^{13}	−0.50	0.86	1.99×10^{13}
12	$CO_2^* + H^* \rightarrow tCOOH^*$	0.84	7.93×10^{13}	0.83	0.01	4.40×10^{13}
13	$tCOOH^* \rightarrow cCOOH^*$	0.27	2.08×10^{13}	−0.07	0.34	2.53×10^{13}
14	$cCOOH^* \rightarrow COH^* + O^*$	0.49	1.32×10^{13}	−0.81	1.30	2.00×10^{12}
15	$COH^* \rightarrow CO^* + H^*$	0.62	1.50×10^{13}	−1.40	1.43	2.03×10^{13}

[a] The relevant kinetic parameters of the RWGS reaction over the Mo_2C MXene surface are the activation barriers, E_a, given in eV, and pre-exponential factors, A_i, given in s^{-1}, both shown for forward and backward reactions. Reaction energies, ΔE, given in eV, are listed for each elementary reaction in the forward reaction, but note that $\Delta E_{forward} = -\Delta E_{backward}$. The activation energy values include the ZPE contribution, whereas A_i factors are obtained from the intercept of the of the Arrhenius linear plot when representing the Ln(rate) of each elementary reaction step versus $1/T$. This is the limit of A_i for $T \rightarrow \infty$. The steps corresponding to adsorption/desorption of reactants (CO_2 and H_2) and products (CO and H_2O) are included just for consistency with the labeling of steps in the microkinetic study.

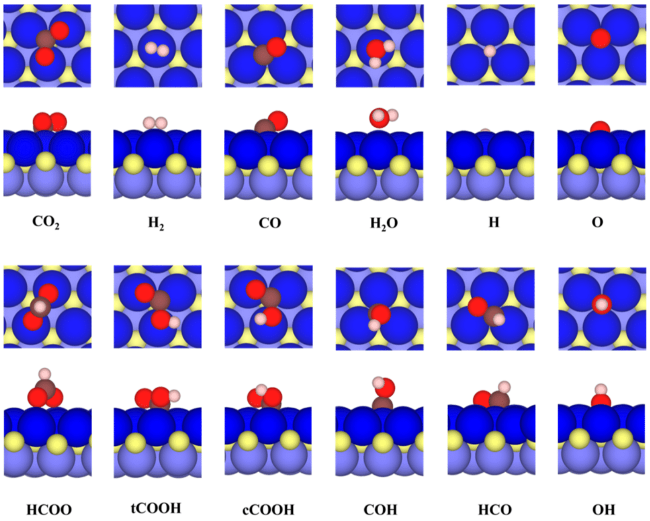

Figure 3. Most stable adsorption sites for CO_2, H_2, CO, H_2O, H, O, HCOO, tCOOH, cCOOH, COH, HCO, and OH on the Mo_2C MXene (0001) surface. Color coding for MXene as in Figure 1, whereas brown, red, and white spheres denote C, O, and H atoms, respectively.

microkinetic modeling as implemented in the MKMCXX program.[39] Our microkinetic model is based on 15 elementary steps for studying the RWGS reaction; see Table 1. The redox mechanism and the associative mechanisms via formate (HCOO) or carboxyl (COOH) intermediates are analyzed. In short, the redox route follows the 1 → 2 → 5 → 6 → 7 → 8 → 3 → 4 sequence, see Table 1; whereas formate route and carboxyl routes imply the 1 → 2 → 9 → 10 → 11 → 7 → 8 → 3 → 4 and 1 → 2 → 12 → 13 → 14 → 15 → 7 → 8 → 3 → 4 sequences, respectively. Note that CO_2 and H_2 adsorptions—steps 1 and 2, respectively—, OH* and H_2O* formations—steps 7 and 8, respectively—, and the CO and H_2O desorptions—steps 3 and 4, respectively—are common for the three mechanisms.

The parameters defining the rates of the surface and desorption reaction steps were estimated from transition state theory (TST),[40,41] including activation energy barriers and the partition functions accounting for the vibration degrees of freedom of ground state and TSs. For surface reactions, constants were estimated through the equation.

$$k = \frac{k_B T}{h}\frac{Q^{TS}}{Q}e^{-E_a/k_B T} \tag{2}$$

where Q and Q^{TS} correspond to the partition functions of the initial state and TS, respectively. The reaction rate constant for unimolecular adsorption is calculated using the collision theory as

$$k_{ads}^{i} = \frac{A_{site}\cdot P_i \cdot S_i}{\sqrt{2\cdot\pi\cdot m_i\cdot k_B\cdot T}} \tag{3}$$

where A_{site} is the area of the adsorption site and is calculated by dividing the supercell area of the (0001) surface by the total number of sites in it;[42] p_i stands for the partial pressure of the component i; S_i corresponds to the sticking coefficient of the component i; and m_i, k_B, and T are the molecular mass, Boltzmann's constant, and working temperature, respectively. Last but not least, note that the sticking coefficient of reactants and products was fixed to 1.0. This selection was based on previous estimations of this coefficient for these molecules on Pt surfaces, where the interaction of the molecules was of the same order of magnitude reporting high S_i values above 0.7,[43−45] and, therefore, no significant influence is expected from this variable in the optimal conditions at which the RWGS reaction proceeds which is confirmed by additional simulations varying this parameter. Further details are given in Table S2 in the Supporting Information.

The steady-state surface coverage for each adsorbed species, θ_i, were calculated by solving the differential equations over time of each intermediate i, where the steady-state solution is reached when $\frac{\partial\theta_i}{\partial t} = 0$.[39] These coverage values were next used to calculate the rates of the individual elementary reaction steps and the overall rate per surface atom. Lateral interactions and their influence on activation barriers were not considered in this study. The present microkinetic simulation rely on a mean-field approximation in which interactions between the adsorbed species are neglected, and all species are randomly distributed over the Mo_2C MXene surface. The kinetic database used as input for the microkinetic simulations is reported in Table 1, with additional details given in the Supporting Information. Our simulations only include the initial partial pressure of reactants (i.e., CO_2 and H_2), which is consistent with the design of a given type of differential reactor in which products are constantly removed. This reactor consists of a thin catalyst bed, which results in a small conversion of reactants into products. In other words, the zero-conversion approximation is considered because the focus is on

https://doi.org/10.1021/acscatal.2c04489
ACS Catal. 2022, 12, 15658−15667

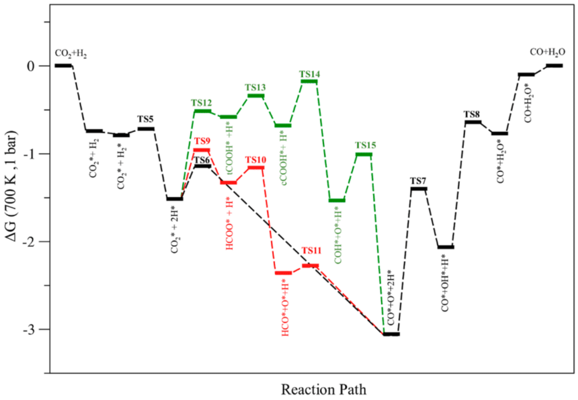

Figure 4. Calculated Gibbs free energy, ΔG, given in eV, profile of the redox (black), HCOO (red), and COOH (green) route mechanisms for the RWGS reaction on the Mo_2C MXene (0001) surface. The TSs are identified in consistency with the reaction elementary step number as listed in Table 1.

the behavior of Mo_2C MXene as a suitable catalyst for the RWGS reaction.

3. RESULTS AND DISCUSSION

3.1. Total Energy and Gibbs Free Energy Profiles. We start by exploring the adsorption energy landscape for the different gas phase species involved in the RWGS reaction on the basal (0001) plane of the Mo_2C MXene model, depicted in Figure 2. This analysis involves the CO_2 and H_2 reactants and CO and H_2O products in their most stable configuration, as shown in Figure 3. The calculated E_{ads} values for reactants and products are −1.80, −0.79, −2.39, and −0.95 eV including ZPE correction for the CO_2, H_2, CO, and H_2O molecules, respectively. These exothermic adsorption energies agree with those in previous work published by some of us.[27,29] Among them, the largest activation corresponds to CO followed by CO_2, whereas the E_{ads} values for H_2 and H_2O are below −1 eV, indicating that, in these cases, the molecular interaction can well correspond to a physisorption process. Similar H_2 molecular interaction, known as the Kubas state, has been observed in other supports such as graphene.[46] The interactions of CO_2, H_2, and H_2O with the Mo_2C (0001) surface are in a parallel orientation to the MXene surface; meanwhile, the CO molecule interacts through its C atom with a certain tilt locating the O atom far from the surface, see Figure 3.

The reaction energy, ΔE, of the RWGS reaction in gas phase calculated with the PBE exchange−correlation functional is 0.85 eV which deviates significantly from the experimental reaction enthalpy of 0.42 eV (40.52 kJ mol^{-1}) at room temperature.[47] On the other hand, accurate predictions based on coupled cluster singles and doubles (CCSD) report ΔE equal to 0.39 eV, thus close to the experimental value. We note that CCSD results are introduced just to compare with our PBE results. Clearly, the difference between PBE and CCSD or experiments is due to intrinsic errors of these DFT-based methods, an error that can be minimized by correcting the DFT-based gas phase values accounting for DFT systematic errors on the energy of gas phase molecules.[48] Because the error in the energy of H_2 and H_2O is negligible, we extract the CO_2 and CO PBE energy corrections from the values provided for the errors in the standard Gibbs formation energy reported in ref 48. These were computed using experimental entropy values, the error in the Gibbs formation energy arises solely from the DFT energy. Thus, we used values of −0.19 and 0.24 eV for CO_2 and CO, respectively. Taking into account these errors, the calculated ΔE becomes 0.42 eV, matching the experiment. Shortly, the RGWS reaction is an endothermic process and thus requires high temperature to shift the equilibrium toward product formation. This is confirmed by calculating the reaction Gibbs free energy, ΔG, at a temperature of 700 K and partial gases pressures of 1 bar, which, including the total energy correction for gas phase errors, becomes −0.09 eV at 700 K, see Figure 4, and even more exergonic at 1000 K, with ΔG = −0.29 eV.

The total errors in the formation energy of CO_2 and CO represent the difference between DFT Gibbs formation energy and the experimental value. These errors in the standard free energies are density functional-dependent so that the signs and magnitude change in each case. In this work, we apply a semiempirical correction to estimate the corresponding values at room temperatures as the standard total entropies and the experimental standard free energies were obtained from thermodynamic tables at such temperatures. Further details about this semiempirical correction can be found in ref 48.

Once the energy minima of the involved species shown in Figure 3 are identified and properly characterized, we proceeded to investigate the energy barriers required to be surmounted in each one of the elementary reaction steps; see Figure S2 in the Supporting Information to visualize the TSs. The kinetic parameters of each elementary step are listed in Table 1, and the Gibbs energy profile at 700 K and 1 bar of gases partial pressures is depicted in Figure 4 showing that the RWGS reaction progresses through either the redox or the associative mechanisms. The former requires explicitly the dissociation of CO_2* into CO* + O*, whereas the latter ones involve alternative pathways where the CO_2* molecule is hydrogenated and the reaction thus advances through different carbon-containing intermediates. For completeness, the calculated energy profile is shown in Figure S1 in the Supporting Information.

Focusing on the redox (black) route, see Figures 1 and 4, the RWGS reaction starts by the H_2 dissociation to form two H* adatoms followed by the dissociation of CO_2 into CO* and O* adsorbed species. Here, breaking the CO_2 molecule demands an energy barrier of 0.47 eV only. The rest of the route involves the formation of water from the O* and H* adatoms. However, the formation of OH* requires a high energy barrier of 1.59 eV to be overcome, and even the subsequent formation of H_2O is uphill with a demand of 1.68 eV of energy. Therefore, these two latter reaction steps constitute the rate-determining steps in the redox route. Interestingly, a similar rate-determining step was found on the Cu@Mo_2C(001) catalyst involving the corresponding bulk carbide, where the step for OH* formation had an activation barrier of 1.14 eV.[49]

A second competitive pathway involves HCOO* formation (red), see Figures 1 and 4. This is formed by the CO_2* hydrogenation requiring surmounting a mild barrier of 0.56 eV. From here on, the following steps involve the sequential dissociation reaction to produce CO*. The first one corresponds to the formation of HCO*, followed by its dissociation into CO* + H*. The two sequential dissociation steps demand quite low activation energies of 0.29 and 0.36 eV, respectively. The interaction of HCO* intermediate with the Mo_2C (0001) MXene surface implies that the C=O fragment lays planar and in full contact with the surface of catalyst, see Figure 2, which may justify the low activation energy required to obtain CO*. Finally, similar to the redox route, the steps for the formation of OH* and H_2O* species constitute the rate-limiting steps. We notice that the formation of HCOOH, a plausible product, requires a large energy barrier (2.21 eV) compared to that leading to the HCOO* intermediate dissociation to HCO* + O*, making thus the formation of formaldehyde a kinetically inhibited process.

The third pathway (green) proceeds through the formation of the COOH carboxyl intermediate, see Figure 4, produced by activating and hydrogenating the CO_2 molecule leading to COOH*.[50] In particular, the *trans*-COOH (tCOOH*) species is formed with an activation barrier of 0.84 eV. Later, there is a conformational transition toward *cis*-COOH (cCOOH*), with an activation barrier of solely 0.27 eV. This later intermediate is then first dissociated into COH* plus O* and later into CO* plus H* featuring energy barriers of 1.30 and 0.62 eV, respectively. The present calculations confirm that the tCOOH* formation, with an E_a of 0.84 eV, is not fully competitive compared to the redox or the formate formation, with values of 0.47 and 0.56 eV, respectively, so probably the path is not really followed, or at a negligible pace compared to the other two mechanisms, even though the carboxyl mechanism was previously confirmed to be followed, and cCOOH* dissociation being a rate-determining step in the RWGS reaction involving Ni_n/YSZ(111) interfaces.[51]

Thus, from the free energy profile depicted in Figure 4, one concludes that the Mo_2C MXene constitutes an optimal candidate for the heterogeneously catalyzed RWGS reaction, as this reaction takes place with affordable energy barriers, yet the rate-determining steps of the RWGS reaction involve the formation of OH* and H_2O* regardless the followed mechanistic route, together with the CO and H_2O products desorption. This implies that the reaction requires high a working temperature and gas pressures to be carried out, a point nevertheless dictated by the reaction thermodynamics, because, obviously, the catalyst effect is actually on the kinetics only. To further clarify this latter issue, microkinetic simulations are carried out to identify the optimal conditions to generate CO and H_2O.

3.2. Microkinetic Analysis. We now focus on microkinetic simulations to predict surface coverages and relative product selectivity including the detection of most abundant reaction intermediates. Based on the DFT data from Table 1, we developed different microkinetic models to further investigate the activity of the Mo_2C MXene catalyst under different T/p_i working conditions. To select the working conditions of the simulations, we relied on literature for Molybdenum carbide-derived catalysts that have shown good performance for the RWGS reaction. Thus, 1% Cu@β-Mo_2C and 7.5% Co@Mo_2C have shown selectivities of 40 and ~98.1% for the RWGS using 2:1 H_2/CO_2 ratio at 300 °C and 0.1 and 1.07×10^{-4} MPa (10 and 1.07×10^{-3} bar), respectively.[16,52] Bare Mo_2C catalysts have shown as well an outstanding selectivity above 90% under the same conditions of 7.5% Co@Mo_2C.[16] These available experimental data are taken as the reference for setting the working conditions to perform microkinetic simulations of the RWGS reaction over Mo_2C MXene.

Thus, the microkinetic simulations have been carried at three different total pressures (i.e., 1, 5, and 10 bar) and using a H_2/CO_2 ratio of 2:1. The evolution of the coverage of the different adsorbed species with the temperature is shown in Figure 5. The total pressure has an influence on the coverage in the temperature window of 300−550 K. Here, one observes that the HCOO* species has a coverage slightly above 0.1 at 1 bar, and increases reaching coverages of 0.3 and 0.4 at 5 and 10 bar, respectively. The HCO* coverage is around 0.4 regardless the total pressure. On the other hand, the CO* species is also present at the MXene catalyst surface regardless the total pressure because CO desorption starts at 700 K. Finally, the presence of O* starts to be important at 400 K and above such temperature increases exponentially promoting the O-functionalization of the Mo_2C MXene surface, a trend that is systematically observed regardless the total pressure as well. For practical applications, the catalysts surface may need to be regenerated after a few cycles. Note that the steady-state is reached at short timescales when the production/consumption rate of the gas species is constant. However, from a microkinetic viewpoint, and because the MXene trends to functionalize its surface, it is more reasonable to describe this process as a "quasi-steady state".

The present microkinetic simulations reveal that the RWGS reaction progresses through the formate associative mechanism beyond 200 K, where the formation of HCOO*, with an E_a of 0.56 eV is overcome. From 300 K on, the HCO* formation is observed, overcoming the E_a of 0.29 eV. Above 350 K, the formation of the CO product is observed, either coming from HCO decomposition, with an E_a of 0.36 eV, or through the redox mechanism, with an E_a of 0.47 eV. At this point, one may wonder why the RGWS reaction does not proceed through a redox route having an initial lower energy barrier than the HCOO route. A plausible response is found in the high hydrogen adatom, H*, coverage of the Mo_2C catalyst above 350 K. Given that the lateral interactions between H* are negligible,[27] the formate associate pathway is favorable, and CO_2 dissociation is inhibited. Only when H* decreases, the formation of CO* species is possible through the redox path.

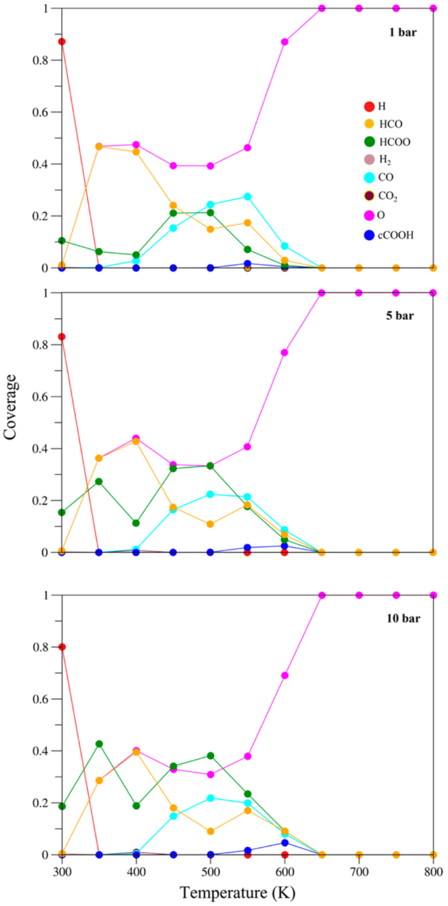

Figure 5. Variation of the surface coverage with the temperature for the RWGS reaction species on the Mo_2C MXene (0001) surface with input H_2/CO_2 2:1 ratio and carried out at three different total pressures: 1, 5, and 10 bar, shown in top, middle, and bottom panels, respectively.

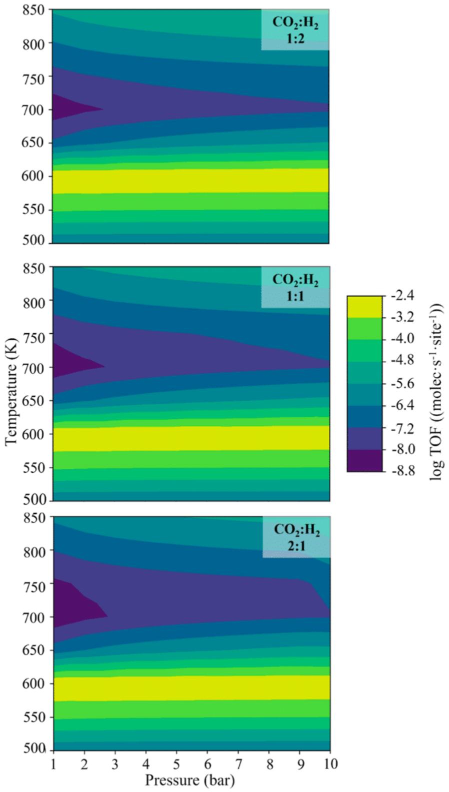

Figure 6. Heating map of TOF under different p and T working conditions for the RWGS reaction on the (0001) Mo_2C MXene surface for the CO production. Units for pressure, temperature, and TOF are bar, K, and molecules·site^{-1}·s^{-1}, respectively. The TOF scale corresponds to the common logarithm with base 10.

To measure the instantaneous efficiency of the Mo_2C MXene as a RWGS catalyst, we analyzed the turnover frequency (TOF), defined here as the number of molecules generated per site and second. This analysis allows us to identify the optimal pressure and temperature conditions at which the RGWS reaction has the largest production (or TOF number). Figure 6 depicts a heating contours map for the RWGS using three H_2/CO_2 ratios of 2:1, 1:1, and 1:2 for the CO production. By using this type of maps, one can identify the effect of the partial pressure on the final production. The TOF scale depicted in Figure 6 corresponds to the CO production, generated in the 400−650 K temperature range, see Figure 5, with similar heating maps considering the TOF of water reported in Figure S3 in the Supporting Information. Even if CO is produced in the 400−650 K temperature range, reasonable TOF values for water require a higher temperature. This prediction is somehow expected given the aforementioned high energy barriers to form OH* and H_2O*, see Figure 4. In other words, the Mo_2C MXene surface easily dissociates H_2O into HO + H, as predicted in an earlier work,[53] and higher temperatures are needed to hydrogenate O adatoms toward water.[22]

Focusing on CO production, the present multiscale analysis predicts that the highest production will take place at ∼600 K, see Figure 6. Interestingly, such production is not affected neither by the CO_2/H_2 ratio nor by the total pressure. To clarify the analysis, we focus on the CO_2/H_2 1:2 ratio. Here, one can see that the temperature range of maximum CO* production matches with the same range where the MXene surface is partially covered by CO species; see cyan dots in

Figure 5. On the other hand, the CO_2/H_2 ratio only affects the region where the TOF has the lowest values; the blue dark regions of the Figure 6 heatmap. Furthermore, the present simulations indicate that the water production is significantly lower than that of CO and that the highest TOF values are reached at high temperatures, above 800 K, and using high pressures, around 10 bar, see Figure S3. Finally, we note that the water production is affected by the CO_2/H_2 ratio, being more favorable with a H_2 partial pressure higher than that of CO_2. The apparent activation route for each route can be estimated directly from our microkinetic simulations and values of 2.83, 2.70, and 2.22 eV are obtained for the redox, HCOO, and COOH routes at 700 K.

To summarize, the Mo_2C MXene basal surface constitutes an appropriate heterogeneous catalyst candidate for the RWGS reaction. The formation of CO is easily achieved at low pressures and ~600 K (~300 °C), but water generation demands higher pressures and temperatures that can compromise the stability of the catalyst, but leave the path open to swing operando conditions where CO is first generated and released, and later, the O-terminated MXene is regenerated by hydrogenating O* species to H_2O at larger temperatures (~550 °C).[26] Attending to the stability of Ti_3C_2,[29] this temperature does not compromise, in principle, the stability of its Ti_2C counterpart.

Available experimental data reported for MoC, Mo_2C catalysts derived from these carbides show that these systems exhibit different performances for the RWGS reaction. For instance, Mo_2C, MoC_{1-x}, and Mo_xC_y/SiO_2 catalysts promote CO_2 conversion below 20 bar, 240 °C, and H_2/CO_2 ratio equal to 16:3 conditions.[54] Other catalysts involving semiconducting materials such as MoC/TiO_2 and MoC_2/ZrO_2 transform CO_2 below 20 bar, 250 °C, and H_2/CO_2 ratio equal to 5:1 conditions.[55] Finally, β-Mo_2C, Cu/Mo_2C, Cs/Mo_2C, and $Cu/Cs{-}Mo_2C$ catalysts requires similar pressures 20 bar but lower temperature (150 °C) and H_2/CO_2 ratio of 3:1.[56] By this comparison, one can conclude that the relative mild conditions at which CO is produced put the Mo_2C MXene in a privileged position for using it as co-catalyst, either for the RWGS, or for subsequent hydrogenation processes aimed at obtaining new high-value chemicals such as CH_4 or CH_3OH.

Before ending this section, we must highlight that there are two main differences between the Mo_2C MXene and the pristine Mo_2C surfaces making the first one a better candidate. The former has an intrinsic bidimensional nature that facilities the interaction with the molecules and exposes the (0001) surface Mo-terminated. This latter surface is equivalent to the $Mo_2C(111)$ surface also terminated in Mo. This latter surface is difficult to realize experimentally, whereas the (0001) surface in MXenes is the exposed one. Additional information is provided in ref 28.

4. CONCLUSIONS

First-principles electronic structure calculations coupled to microkinetic simulations have been carried out to investigate the performance of the Mo_2C MXene as a heterogenous catalyst for the RWGS reaction. This reaction requires relatively high temperatures to make the thermodynamics favorable. Indeed, temperatures around or higher than 700 K are found to be convenient for a reasonable production at a standard pressure of 1 bar. The three different RWGS mechanisms—redox, formate, and carboxyl routes—were investigated thoroughly by considering thermodynamic and kinetics aspects. Among them, the redox and formate routes emerge as the most plausible for the Mo_2C MXene-catalyzed RWGS reaction. The present analysis predicts that the formation of OH and the subsequent formation of H_2O constitute the rate-limiting step to complete the reaction; meanwhile, CO formation is easily achieved.

Microkinetic simulations showed that, not surprisingly, the catalyst coverage can be altered by the total pressure, largely observed indeed for HCOO* and HCO* intermediates. On the other hand, the temperature range at which the CO is formed is found to be rather pressure-independent. By means of TOF heating maps as a function of p/T working conditions, we identified the optimal pressure and temperature situations at which the TOF acquires the maximum values. Our simulations conclude that the formation of CO is feasible at ~600 K and a low total pressure of 1 bar, and that such optimal conditions are maintained regardless the CO_2/H_2 ratio. Although the formation of CO is relatively accessible, water formation requires harsher conditions, observable at ~800 K and above 5 bar, and it is also predicted that low CO_2/H_2 ratios may promote the H_2O formation at total pressure below 5 bar.

All in all, the present multiscale analysis poses Mo_2C MXene as a catalyst candidate for the RWGS reaction, thus contributing to CO_2 valorization economy by converting this waste product into generating CO, a precursor toward the formation of CH_4 or CH_3OH. Because the Mo_2C MXene is able to produce CO through the RWGS rection under mild conditions, one can also speculate about using it as a co-catalyst in subsequent CO hydrogenation processes leading to higher added value chemicals such as CH_4 or CH_3OH.

■ ASSOCIATED CONTENT

Supporting Information

The Supporting Information is available free of charge at https://pubs.acs.org/doi/10.1021/acscatal.2c04489.

> Calculated frequencies, energy profile of the RWGS, transition state schemes, brief description of the microkinetic simulations, and heating maps of TOF versus p/T of RWGS for H_2O production (PDF)

■ AUTHOR INFORMATION

Corresponding Authors

Ángel Morales-García – *Departament de Ciència de Materials i Química Física & Institut de Química Teòrica i Computacional (IQTCUB), Universitat de Barcelona, 08028 Barcelona, Spain;* orcid.org/0000-0003-0491-1234; Email: angel.morales@ub.edu

Francesc Illas – *Departament de Ciència de Materials i Química Física & Institut de Química Teòrica i Computacional (IQTCUB), Universitat de Barcelona, 08028 Barcelona, Spain;* orcid.org/0000-0003-2104-6123; Email: francesc.illas@ub.edu

Authors

Anabel Jurado – *Departament de Ciència de Materials i Química Física & Institut de Química Teòrica i Computacional (IQTCUB), Universitat de Barcelona, 08028 Barcelona, Spain*

Francesc Viñes – *Departament de Ciència de Materials i Química Física & Institut de Química Teòrica i Computacional (IQTCUB), Universitat de Barcelona,* *08028 Barcelona, Spain;* orcid.org/0000-0001-9987-8654

Complete contact information is available at:
https://pubs.acs.org/10.1021/acscatal.2c04489

Notes

The authors declare no competing financial interest.

■ ACKNOWLEDGMENTS

This study has been supported by the Spanish Ministry of Science and Innovation (MICIN) through the project MCIN/AEI/10.13039/501100011033 PID2021-126076NB-I00, TED2021-129506B-C22, PID2020-115293RJ-I00, and the CEX2021-001202-M *María de Maeztu* unit of excellence. *Red Española de Supercomputación* (RES) is also acknowledged for the generous computational resources provides through the QHS-2021-3-0021 project.

■ REFERENCES

(1) Catlow, C. R.; Davidson, M.; Hardacre, C.; Hutchings, G. J. Catalysis Making The World a Better Place. *Philos. Trans. R. Soc., A* **2016**, *374*, 20150089.

(2) Friend, C. M.; Xu, B. Heterogeneous Catalysis: A Central Science for a Sustainable Future. *Acc. Chem. Res.* **2017**, *50*, 517−521.

(3) Whang, H. S.; Lim, J.; Choi, M. S.; Lee, J.; Lee, H. Heterogeneous catalysts for catalytic CO_2 conversion into value-added chemicals. *BMC Chem. Eng.* **2019**, *1*, 9.

(4) Morales-García, Á.; Viñes, F.; Gomes, J. R. B.; Illas, F. Concepts, Models, and Methods in Computational Heterogeneous Catalysis Illustrated through CO_2 Conversion. *Wiley Interdiscip. Rev.: Comput. Mol. Sci.* **2021**, *11*, No. e1530.

(5) He, Y. L.; Yang, K. R.; Yu, Z. W.; Fishman, Z. S.; Achola, L. A.; Tobin, Z. M.; Heinlein, J. A.; Hu, S.; Suib, S. L.; Batista, V. S.; Pfefferle, L. D. Catalytic manganese oxide nanostructures for the reverse water gas shift reaction. *Nanoscale* **2019**, *11*, 16677−16688.

(6) Saeidi, S.; Najari, S.; Fazlollahi, F.; Nikoo, M. F.; Sefidkon, F.; Klemeš, J. J.; Baxter, L. L. Mechanisms and kinetics of CO_2 hydrogenation to value-added products: A detailed review on current status and future trends. *Renewable Sustainable Energy Rev.* **2017**, *80*, 1292−1311.

(7) Su, X.; Yang, X. L.; Zhao, B.; Huang, Y. Q. Designing of highly selective and high-temperature endurable RWGS heterogeneous catalysts: recent advances and the future directions. *J. Energy Chem.* **2017**, *26*, 854−867.

(8) Ginés, M. J. L.; Marchi, A. J.; Apesteguía, C. R. Kinetic study of the reverse water-gas shift reaction over $CuO/ZnO/Al_2O_3$ catalysts. *Appl. Catal., A* **1997**, *154*, 155−171.

(9) Daza, Y. A.; Kent, R. A.; Yung, M. M.; Kuhn, J. N. Carbon Dioxide Conversion by Reverse Water-Gas Shift Chemical Looping on Perovskite-type Oxides. *Int. Eng. Chem. Res.* **2014**, *53*, 5828−5837.

(10) Dong, Q.; Yin, S.; Guo, C. S.; Sato, T. $Ce_{0.5}Zr_{0.4}Sn_{0.1}O_2/Al_2O_3$ catalysts with enhanced oxygen storage capacity and high CO oxidation activity. *Catal. Sci. Technol.* **2012**, *2*, 2521−2524.

(11) Graciani, J.; Mudiyanselage, K.; Xu, F.; Baber, A. E.; Evans, J.; Senanayake, S. D.; Stacchiola, D. J.; Liu, P.; Hrbek, J.; Sanz, J. F.; Rodriguez, J. A. Highly active copper-ceria and copper-ceria-titania catalysts for methanol synthesis from CO_2. *Science* **2014**, *345*, 546−550.

(12) Álvarez Galván, C.; Schumann, J.; Behrens, M.; Fieero, J. L. G.; Schlogl, R.; Frei, E. Reverse Water-gas Shift Reaction at the Cu/ZnO Interface: Influence of the Cu/Zn ratio on Structure-Activity Correlations. *Appl. Catal., B* **2016**, *195*, 104−111.

(13) Ishito, N.; Hara, K. J.; Nakajima, K.; Fukuoka, A. Selective Synthesis of Carbon Monoxide via Formates in Reverse Water-Gas Shift Reaction Over Alumina-Supported Gold Catalyst. *J. Energy Chem.* **2016**, *25*, 306−310.

(14) Ramanathan, S.; Oyama, S. T. New Catalysts for Hydroprocessing: Transition Metal Carbides and Nitrides. *J. Phys. Chem.* **1995**, *99*, 16365−16372.

(15) Chen, J. G. Carbide and Nitride Overlayers on Early Transition Metal Surfaces: Preparation, Characterization, and Reactivities. *Chem. Rev.* **1996**, *96*, 1477−1498.

(16) Porosoff, M. D.; Yang, X.; Boscoboinik, J. A.; Chen, J. G. Molybdenum Carbide as Alternative Catalysts to Precious Metals for Highly Selective Reduction of CO_2 to CO. *Angew. Chem., Int. Ed.* **2014**, *53*, 6705−6709.

(17) Ma, Y.; Guo, Z.; Jiang, Q.; Wu, K.-H.; Gong, H.; Liu, Y. Molybdenum carbide clusters for thermal conversion of CO_2 to CO via reverse water-gas shift reaction. *J. Energy Chem.* **2020**, *50*, 37−43.

(18) Posada-Pérez, S.; Viñes, F.; Rodriguez, J. A.; Illas, F. Fundamentals of Methanol Synthesis on Metal Carbide Based Catalysts: Activation of CO_2 and H_2. *Top. Catal.* **2015**, *58*, 159−173.

(19) Naguib, M.; Kurtoglu, M.; Presser, V.; Lu, J.; Niu, J.; Heon, M.; Hultman, L.; Gogotsi, Y.; Barsoum, M. W. Two-Dimensional Nanocrystals Produced by Exfoliation of Ti_3AlC_2. *Adv. Mater.* **2011**, *23*, 4248−4253.

(20) Naguib, M.; Barsoum, M. W.; Gogotsi, Y. Ten Years of Progress in the Synthesis and Development of MXenes. *Adv. Mater.* **2021**, *33*, 2103393.

(21) Alhabeb, M.; Maleski, K.; Anasori, B.; Lelyukh, P.; Clark, L.; Sin, S.; Gogotsi, Y. Guidelines for Synthesis and Processing of Two-Dimensional Titanium Carbide ($Ti_3C_2T_x$ MXene). *Chem. Mater.* **2017**, *29*, 7633−7644.

(22) Persson, I.; Halim, J.; Lind, H.; Hansen, T. W.; Wagner, J. B.; Näslund, L.; Darakchieva, V.; Palisaitis, J.; Rosen, J.; Persson, P. O. Å. 2D Transition Metal Carbides (MXenes) for Carbon Capture. *Adv. Mater.* **2018**, *31*, 1805472.

(23) Kamysbayev, V.; Filatov, A. S.; Hu, H.; Rui, X.; Lagunas, F.; Wang, D.; Klie, R. F.; Talapin, D. V. Covalent Surface Modifications and Superconductivity of Two-Dimensional Metal Carbide MXenes. *Science* **2020**, *369*, 979−983.

(24) Morales-García, Á.; Fernández-Fernández, A.; Viñes, F.; Illas, F. CO_2 Abatament Using Two-Dimensional MXenes Carbides. *J. Mater. Chem. A* **2018**, *6*, 3381−3385.

(25) Morales-Salvador, R.; Morales-García, Á.; Viñes, F.; Illas, F. Two-dimensional nitrides as highly efficient potential candidates for CO_2 capture and activation. *Phys. Chem. Chem. Phys.* **2018**, *20*, 17117−17124.

(26) Morales-Salvador, R.; Gouveia, J. D.; Morales-García, Á.; Viñes, F.; Gomes, J. R. B.; Illas, F. Carbon Capture and Usage by MXenes. *ACS Catal.* **2021**, *11*, 11248−11255.

(27) López, M.; Morales-García, Á.; Viñes, F.; Illas, F. Thermodynamics and Kinetics of Molecular Hydrogen Adsorption and Dissociation on MXenes: Relevance to Heterogeneously Catalyzed Hydrogenation Reactions. *ACS Catal.* **2021**, *11*, 12850−12857.

(28) Morales-García, Á.; Calle-Vallejo, F.; Illas, F. MXenes: New Horizons in Catalysis. *ACS Catal.* **2020**, *10*, 13487−13503.

(29) Li, Z.; Wang, L.; Sun, D.; Zhang, Y.; Liu, B.; Hu, Q.; Zhou, A. Synthesis and thermal stability of two-dimensional carbide MXene Ti_3C_2. *Mater. Sci. Eng., B* **2015**, *191*, 33−40.

(30) Jurado, A.; Morales-García, Á.; Viñes, F.; Illas, F. Identifying the Atomic Layer Stacking of Mo_2C MXene by Probe Molecule Adsorption. *J. Phys. Chem. C* **2021**, *125*, 26808−26813.

(31) Posada-Pérez, S.; RamírezGutiérrez, P. R.; Stacchiola, D.; Viñes, F.; Liu, P.; Illas, F.; Rodriguez, J. A. The Conversion of CO_2 to Methanol on orthorhombic β-Mo_2C and Cu/β-Mo_2C Catalysts: Mechanism for Admetal Induced Change in the Selectivity and Activity. *Catal. Sci. Technol.* **2016**, *6*, 6766−6777.

(32) Kresse, G.; Furthmüller, J. Efficient iterative schemes forab initiototal-energy calculations using a plane-wave basis set. *Phys. Rev. B: Condens. Matter Mater. Phys.* **1996**, *54*, 11169.

(33) Perdew, J. P.; Burke, K.; Ernzerhof, M. Generalized Gradient Approximation Made Simple. *Phys. Rev. Lett.* **1996**, *77*, 3865−3868.

(34) Grimme, S.; Antony, J.; Ehrlich, S.; Krieg, S. A. A consistent and accurate ab initio parametrization of density functional dispersion

correction (DFT-D) for the 94 elements H-Pu. *J. Chem. Phys.* **2010**, *132*, 154104.

(35) Blöch, P. E. Projector Augmented-Wave Method. *Phys. Rev. B: Condens. Matter Mater. Phys.* **1994**, *50*, 17953.

(36) Henkelman, G.; Uberuaga, B. P.; Jónsson, H. A. A climbing image nudged elastic band method for finding saddle points and minimum energy paths. *J. Chem. Phys.* **2000**, *113*, 9901.

(37) Henkelman, G.; Jónsson, H. A. A dimer method for finding saddle points on high dimensional potential surfaces using only first derivatives. *J. Chem. Phys.* **1999**, *111*, 7010.

(38) Rogal, J.; Reuter, K.Ab Initio Atomistic Thermodynamic for Surfaces: A Primer. *Experiment, Modeling and Simulation of GasSurface Interactions for Reactive Flows in Hypersonic Flights*; Educational Notes RTO-EN-AVT-142: Neuilly-sur-Seine, France, 2007; Vol. *2*, pp 1−18.

(39) Filot, I. A. W.*Introduction to Microkinetic Modeling*; Technische Universiteit Eindhoven: Eindhoven, 2018; p 217.

(40) Laldler, K. J.; King, M. C. The Development of Transition-State Theory. *J. Phys. Chem.* **1983**, *87*, 2657−2664.

(41) Truhlar, D. G.; Garrett, B. C.; Klippenstein, S. J. Current Status of Transition-State Theory. *J. Phys. Chem.* **1996**, *100*, 12771−12800.

(42) Pogodin, S.; López, N. A More Accurate Kinetic Monte Carlo Approach to a Monodimensional Surface Reaction: The Interaction of Oxygen with the $RuO_2(110)$ Surface. *ACS Catal.* **2014**, *4*, 2328−2332.

(43) Liu, J.; Xu, M.; Nordmeyer, T.; Zaera, F. Sticking Probabilities for CO Adsorption on Pt(111) Surfaces Revisited. *J. Phys. Chem.* **1995**, *99*, 6167−6175.

(44) Hellsing, B.; Kasemo, B.; Ljungström, S.; Rosén, A.; Wahnström, T. Kinetic model and experimental results for H_2O and OH production rates on Pt. *Surf. Sci.* **1987**, *189*−*190*, 851−860.

(45) McCabe, R. W.; Schmidt, L. D. binding states of CO and H_2 on clean and oxidized (111)Pt. *Surf. Sci.* **1977**, *65*, 189−209.

(46) Manadé, M.; Viñes, F.; Gil, A.; Illas, F. On the H_2 Interactions with Transition Metal Adatoms Supported on Graphene: A Systematic Density Functional Theory. *Phys. Chem. Chem. Phys.* **2018**, *20*, 3819−3830.

(47) King, A. D.; King, R. B.; Yang, D. B. Homogeneous Catalysis of the Water Gas Shift Reaction Using Iron Pentacarbonyl. *J. Am. Chem. Soc.* **1980**, *102*, 1028−1032.

(48) Granda-Marulanda, L. P.; Rendón-Calle, A.; Builes, S.; Illas, F.; Koper, M. T. M.; Calle-Vallejo, F. A Semiempirical Method to Detect and Correct DFT-Based Gas-Phase Errors and Its Application in Electrocatalysis. *ACS Catal.* **2020**, *10*, 6900−6907.

(49) Jing, H.; Li, Q.; Wang, J.; Liu, D.; Wu, K. Theoretical Study of the Reverse Water Gas Shift Reaction on Copper Modified β-$Mo_2C(001)$ Surfaces. *J. Phys. Chem. C* **2019**, *123*, 1235−1251.

(50) Tibiletti, D.; Goguet, A.; Meunier, F. C.; Breen, J. P.; Burch, R. On the Importance of Steady-State Isotropic Techniques for the Investigation of the Mechanism of the Reverse Water-Gas-Shift Reaction. *Chem. Commun.* **2004**, 1636−1637.

(51) Cadi-Essadek, A.; Roldan, A.; Aparicio-Anglès, X.; de Leeuw, N. H. CO_2 and H_2 Adsorption and Reaction at Nin/YSZ(111) Interfaces: A Density Functional Theory Study. *J. Phys. Chem. C* **2018**, *122*, 19463−19472.

(52) Zhang, X.; Zhu, X. B.; Lin, L. L.; Yao, S. Y.; Zhang, M. T.; Liu, X.; Wang, X.; Li, Y.-W.; Shi, C.; Ma, D. Highly Dispersed Copper over β-Mo2C as an Efficient and Stable Catalyst for the Reverse Water Gas Shift (RWGS) Reaction. *ACS Catal.* **2017**, *7*, 912−918.

(53) Gouveia, J. D.; Morales-García, Á.; Viñes, F.; Illas, F.; Gomes, J. R. B. MXenes as promising catalysts for water dissociation. *Appl. Catal., B* **2020**, *260*, 118191.

(54) Blanco, A. A. G.; Furlong, O. J.; Stacchiola, D. J.; Sapag, K.; Nazzarro, M. S. Porous Mo_xC_y/SiO_2 Material for CO_2 Hydrogenation. *Top. Catal.* **2019**, *62*, 1026−1034.

(55) Hamdan, M. A.; Nassereddine, A.; Checa, R.; Jahjah, M.; Pinel, C.; Piccolo, L.; Perret, N. Supported Molybdenum Carbide and Nitride Catalysts for Carbon Dioxide Hydrogenation. *Front. Chem.* **2020**, *8*, 452−464.

(56) Dongil, A. B.; Zhang, Q.; Pastor-Pérez, L.; Ramírez-Reina, T.; Guerrero-Ruiz, A.; Rodríguez-Ramos, I. Effect of Cu and Cs in the β-Mo_2C System for CO_2 Hydrogenation to Methanol. *Catalysts* **2020**, *10*, 1213.

6.3 Conclusions

The Reverse Water Gas Shift (RWGS) reaction has been investigated using Mo_2C MXene as catalysts. Calculations show these materials as a candidate for the conversion of CO_2 into CO, a plausible feedstock for the methanol synthesis through the Fischer-Tropsch process. The main results can be summarized as follows:

- Microkinetic simulations present that the coverage can be tuneable by the total pressure.
- The favourable mechanism involved is the Redox path. However, the reaction only takes place when Hydrogen is present in low ratio.
- The determining steps for all available routes are the formation of OH* and H_2O*, being the energy barriers 1.59 eV and 1.68 eV, respectively.
- The highest production of CO appears at ~600 K regardless the total pressure of the system or the H_2/CO_2 ratio.
- Temperature required for the H_2O formation is higher than the CO formation. This is linked to aforementioned energy barriers.
- RWGS on Mo_2C MXene needs temperatures above 700 K at 1 bar to be thermodynamically favourable.

6.4 References

1. Ramanathan, S.; Oyama, S. T. New Catalysts for Hydroprocessing:Transition Metal Carbides and Nitrides. *J. Phys. Chem.,* **1995**, *99*, 16365– 16372
2. Morales-Salvador, R.; Morales-García, Á.; Viñes, F.; Illas, F. Two-dimensional nitrides as highly efficient potential candidates for CO_2 capture and activation. *Phys. Chem. Chem. Phys.,* **2018**, *20*, 17117–17124,
3. López, M.; Morales-García, Á.; Viñes, F.; Illas, F. Thermodynamics and Kinetics of Molecular Hydrogen Adsorption and Dissociation on MXenes: Relevance to Heterogeneously Catalyzed Hydrogenation Reactions. *ACS Catal.,* **2021**, *11*, 12850– 12857
4. Henkelman, G.; Uberuaga, B. P.; Jónsson, H. A Climbing Image Nudged Elastic Band Method for Finding Saddle Points and Minimum Energy Paths. *J. Chem. Phys*., **2000**, 113, 9901.
5. Henkelman, G.; Jónsson, H. A Dimer Method for Finding Saddle Points on High Dimensional Potential Surfaces Using Only First Derivatives. *J. Chem. Phys*. **1999**, 111, 7010.
6. Filot, I. A. W.; van Santen, R. A.; Hensen, E. J. M. The Optimally Performing Fischer–Tropsch Catalyst, *Angew. Chem. Int. Ed.,* **2014**, 53, 12746-12750.
7. King, A. D.; King, R. B.; Yang, D. B. Homogeneous Catalysis of the Water Gas Shift Reaction Using Iron Pentacarbonyl. *J. Am. Chem. Soc*. **1980,** 102, 1028– 1032.

CHAPTER SEVEN

Final Conclusions

The goal of the present Doctoral Thesis has been the study of MXenes as catalyst for capture and transformation of the CO_2. This study has been carried out through computational approaches using DFT. The overall conclusions are summarized the following conclusions.

Regarding Adsorption and Activation on Nitride MXenes:

This systematic analysis confirms the capability of nitride MXenes with different stoichiometries, M_2N, M_3N_2 y M_4N_3 (M=Ti, Zr, Hf, V, Nb, Ta, Cr, Mo, and W), to active and capture CO_2. In general, d^2-MXenes (Ti, Zr and Hf) present the most exothermic adsorption energies followed by d^3-MXenes (V, Nb and Ta) and d^4-MXenes (Cr, Mo and W). This trend remains increasing the thickness of the structure showing slight difference. However, it is interesting to note that a separately analysis show that d^3- Nb- and Ta-MXenes are widely affected by the thickness increase, whereas V- and d^4 Cr-MXenes are not affected at all. In the middle, d^2 and Mo- MXenes show small but noticeable differences. Curiously, W-derived MXenes follow an opposite trend: CO_2 affinity decreases by increasing the thickness. Regarding the TMN, (111) surfaces behave as MXene surfaces. This fact opens an easier way to study the hard-to-prepare (111) surface. (001) surfaces are less active as expected. Finally, the comparison with carbide MXene counterparts exhibits that M_2N and M_4N_3 carbides have a major affinity for CO_2 whether M_3N_2 for the nitrides.

Topological analysis based on Bader charges reveals a charge transfer from the MXene towards the CO_2 molecule. Thus, the resulting activated CO_2 molecules expose charges between -1.75 and -0.9 *e*. Similar charge transfer is observed in the TMN(111) surfaces.

Interestingly, the low reactivity of TMN (001) is connected with a low activation due to the low charge transfer.

In this way, one can vary the CO_2 affinity changing the composition and thickness of the sample and optimize the adsorption/desorption process. Kinetic phase diagrams describe these results. Thus, with our focus on the endpoints of CO_2 E_{ads}, we can observe whether or not the MXene is suitable for CCS. Low adsorption energies show diagrams with smaller regions or lower CO_2-philicity. Here, it is important to denote that even though at room temperature CO_2 is adsorbed, increasing the temperature the molecule could be easy released. On the other hand, larger adsorption energies exhibit larger CCS conditions, suitable for trapping CO_2.

Regarding the Effect of Stacking on Adsorption of Molecular Probes on Carbide MXenes:

First-principles calculation show that the stacking can influence on the adsorption processes. Here, four different (0001) Mo_2C MXene surface models are analyzed: 1T (ABC), 2H (ABA), the stable ones, and 1T' and 2H' for the compressive and tensile strain, respectively. CO_2, CO and H_2O are used as probe molecules to study adsorption energy, structural features and vibrational modes over all (0001) Mo_2C MXene surfaces.

From the adsorption strength of the studied species, it concludes that the adsorption depends on the MXene surface. The interaction of CO_2 shows an exothermic regardless the stacking, and it follows a sequence: 1T adsorption energy (-1.80 eV) decreases when compressing the structure to 1T’ (-1.21 eV) and this decreases going to 2H (-0.94 eV) structure. From 2H to 2H’(-2.03 eV) the structure becomes tensile and the energy increases. Thereby, the structural parameters elongation distances of C-O and the angle between O-C-O, and the topological Bader charge, follows the same pattern as E_{ads}, see Table 1 of Publication 2. These trends are shared also with the CO molecule but not with H_2O, that changes are negligible due to the fact that the molecule is governed by the dispersion.

Regarding the vibrational analysis performed on the three probe molecules, the results present distinguishable vibrational modes between structures. The asymmetric stretching of the CO_2 molecule differs by ~200 cm^{-1} between the 1T and 2H surfaces and the symmetric stretching of the CO molecule, also performs a noticeable difference of ~300 cm^{-1} between structures. Besides, these molecules accomplish the surface dipole selection rule, allowing thus to be used in spectroscopy.

In short, we conclude that adsorption properties are affected by the stacking sequence of the MXene surface presented. Thus, these properties and the vibrational modes of the molecules, CO_2, CO and, H_2O in lesser extent, suffers a significantly change that allows via simple spectroscopy measurements like IR to distinguish between the different stackings, ABC and ABA.

Regarding Reverse Water Gas Shift Reaction on MXenes:

Calculations show that from the three involved mechanisms: redox, HCOO (formate) and, COOH (carboxyl). The most favorable one is the redox route being the determining limit steps the formation of OH* (1.59 eV) and H_2O* (1.68 eV). However, the microkinetic analysis show that, although the redox route is favourable, CO* is formed through the HCOO route in presence of high ratios of hydrogen given the negligible interaction between H* adatoms. Finally, we conclude that the reaction needs temperatures 700 K or higher to be thermodynamically favourable at 1 bar.

Through the introduction of heating maps, the efficiency of the Mo_2C MXene analysing the TOF as the number of molecules generated per site and second is presented. Thereby, it can be identified that for the H_2O formation, a higher temperature is needed in comparison to CO formation. This is connected with the prior mentioned energy barriers of OH* and H_2O*, meaning that the surface dissociates the molecule into H + OH. Regarding CO, the highest production appears at ~600 K, not being affected by the total pressure of the system or the H_2/CO_2 ratio, see Figure 6 of Publication 3.

In conclusion, Mo_2C MXene as a catalyst for the RWGS is a feasible candidate given the mild conditions needed to produce CO. Thus, this material could be used as a co-catalyst for further hydrogenation processes, decreasing the presence of CO_2 and favouring the formation of value-added products.

Future of this Thesis

Once finished the present Thesis some questions have flourished regarding the MXene scenario. Thus, some topics might be considered for future lines of research:

- Reverse Water Gas Shift Monte-Carlo simulations on Mo_2C MXene to consider lateral interactions.
- Study of the Reverse Water Gas Shift reaction on the ABA stacking of Mo_2C MXene given the presence of the stacking and its effect on adsorption properties.
- Study of the Fisher-Tropsch reaction on Mo_2C, following the conversion of CO into hydrocarbons, e.g., gasoil, kerosene and lubricants.

CHAPTER EIGHT

Contribution to Publications

This chapter describes the contribution to the publications.

Jurado, A.; Ibarra, K.; Morales-García, Á.; Viñes, F.; Illas, F. Adsorption and Activation of CO_2 on Nitride MXenes: Composition, Temperature, and Pressure Effects. *ChemPhysChem*, **2021**, 22, 2456-2463.

> Contribution: Formal Analysis; Investigation; Data Curation; Writing - Original Draft; Writing - Review & Editing.

Jurado, A.; Morales-García, Á.; Viñes, F.; Illas, F. Identifying the Atomic Layer Stacking of Mo_2C MXene by Probe Molecule Adsorption. *J. Phys. Chem. C.,* **2021**, 125, 26808-26813.

> Contribution: Formal Analysis; Investigation; Data Curation; Writing - Original Draft; Writing - Review & Editing.

Jurado, A.; Morales-García, Á.; Viñes, F.; Illas, F. Molecular Mechanism and Microkinetic Analysis of the Reverse Water Gas Shift Reaction Heterogeneously Catalyzed by the Mo_2C MXene. *ACS Catal.* **2022**, 12, 15658-15667.

> Contribution: Formal Analysis; Investigation; Data Curation; Writing - Original Draft; Writing - Review & Editing.

Other publications

Figueras, M.; **Jurado, A**.; Morales-García, Á.; Viñes, F.; Illas, F. Bulk (in)stability as a Possible Source of Surface Reconstruction. *Phys. Chem. Chem. Phys*.**,** **2020**, 22**,** 19249-19253.

Contribution: Formal Analysis; Investigation; Data Curation; Writing - Original Draft; Writing - Review & Editing.

Vázquez-Parga, D.; **Jurado, A.**; Roldan, A.; Viñes, F. A Computational Map of the Probe CO Molecule Adsorption and Dissociation on Transition Metal Low Milles Indices Surfaces. *Appl. Surf. Sci.*, **2023**, 618, 156581.

Contribution: Formal Analysis; Investigation; Data Curation.

APPENDIX

Appendix A:

Supporting Information for “Adsorption and Activation on Nitride MXenes”

ChemPhysChem

Supporting Information

Adsorption and Activation of CO_2 on Nitride MXenes: Composition, Temperature, and Pressure effects

Anabel Jurado, Kevin Ibarra, Ángel Morales-García,* Francesc Viñes, and Francesc Illas

Supporting Information

Adsorption and Activation of CO_2 on Nitride MXenes: Composition, Temperature, and Pressure effects

Anabel Jurado, Kevin Ibarra, Ángel Morales-García*, Francesc Viñes, Francesc Illas

Departament de Ciència de Materials i Química Física & Institut de Química Teòrica i Computacional (IQTCUB), Universitat de Barcelona, c/Martí i Franquès 1-11, 08028 Barcelona, Spain

e-mail: angel.morales@ub.edu

Contents

Table S1. Adsorption energy, E_{ads}, and structural parameters, including CO_2 C-O bond distance, δ(CO), distance between surface metal atoms and CO_2 O atoms, δ(MO), and CO_2 molecular angle, α(OCO), for the activated CO_2 adsorbed on M_3N_2 MXenes on different sites. Q corresponds to the net Bader charge of the activated CO_2. Bolt font indicates the most exothermic E_{ads} for each MXene substrate.

MXene	DFT	E_{ads}/eV	δ(CO)/Å	δ(MO)/Å	α(OCO)/°	Q/*e*
C_b						
Hf_3N_2	PBE	-3.55	1.38/1.43	2.27/2.29	113.4	-2.14
	PBE-D3	-3.84	1.39/1.41	2.28/2.25	114.0	-2.12
V_3N_2	PBE	-1.36	1.26	2.11	136.5	-1.07
	PBE-D3	-1.64	1.27	2.11	134.7	-1.08
Nb_3N_2	PBE	**-1.63**	1.28	2.20	132.3	-1.15
	PBE-D3	**-1.91**	1.28	2.20	132.3	-1.16
Ta_3N_2	PBE	-2.16	1.29	2.12	131.2	-1.28
	PBE-D3	-2.40	1.29	2.12	131.2	-1.28
Cr_3N_2	PBE	**-0.91**	1.26	2.11	136.5	-0.93
	PBE-D3	**-1.58**	1.26	2.08	137.2	-0.88
Mo_3N_2	PBE	**-0.85**	1.26	2.28	135.4	-0.89
	PBE-D3	**-1.25**	1.26	2.26	136.0	-0.88
$C_bO_bO_b$						
Cr_3N_2	PBE	-1.10	1.40/1.29	1.95/2.11	121.7	-1.28
	PBE-D3	-1.43	1.38/1.30	2.06/2.01	119.2	-1.38
Mo_3N_2	PBE	-0.86	1.38/1.36	2.35/2.21	111.7	-1.41
	PBE-D3	-1.16	1.39/1.36	2.24/2.19	111.7	-1.41
C_mO_b						
V_3N_2	PBE	**-1.38**	1.35/1.26	2.20/2.28	132.8	-1.37
	PBE-D3	**-1.67**	1.26/1.34	2.21/2.28	132.9	-1.37
Nb_3N_2	PBE	-1.49	1.27/1.33	2.34/2.36	132.0	-1.42
	PBE-D3	-1.77	1.27/1.33	2.34	132.9	-1.42
Mo_3N_2	PBE	-0.61	1.29/1.26	2.47/2.33	134.4	-1.07
	PBE-D3	-0.93	1.26/1.29	2.46/2.32	134.4	-1.08
$C_mO_nO_n$						
Ti_3N_2	PBE	**-3.30**	1.38	2.20	115.0	-1.85
	PBE-D3	**-3.56**	1.38	2.20	115.1	-1.84
Zr_3N_2	PBE	**-3.42**	1.38/1.39	2.33	114.9	-1.90
	PBE-D3	**-3.68**	1.38/1.39	2.33	114.8	-1.91
Hf_3N_2	PBE	**-3.55**	1.37/1.45	2.31/2.28	113.1	-2.19
	PBE-D3	**-3.84**	1.37/1.44	2.30	113.2	-2.19
C_nO_b						
V_3N_2	PBE	-1.31	1.32/1.26	2.21/2.23	134.1	-1.3
	PBE-D3	-1.61	1.32/1.26	2.22	134.2	-1.3
Nb_3N_2	PBE	-1.54	1.28	2.20	131.3	-1.37
	PBE-D3	-1.82	1.33/1.27	2.33	131.7	-1.37
Cr_3N_2	PBE	**-1.20**	1.26/1.32	2.20/2.18	134.2	-1.20
	PBE-D3	**-1.52**	1.26/1.30	2.17/2.19	135.6	-1.13
$C_nO_mO_m$						

Ta_3N_2	PBE	**-2.32**	1.40	1.98/1.95	111.1	-1.73
	PBE-D3	**-2.54**	1.40	1.98/1.96	111.1	-1.73
			$C_mO_mO_b$			
W_3N_2	PBE	**-1.05**	1.32/1.26	2.40	123.6	-1.07
	PBE-D3	**-1.34**	1.34/1.26	2.40	122.6	-1.07

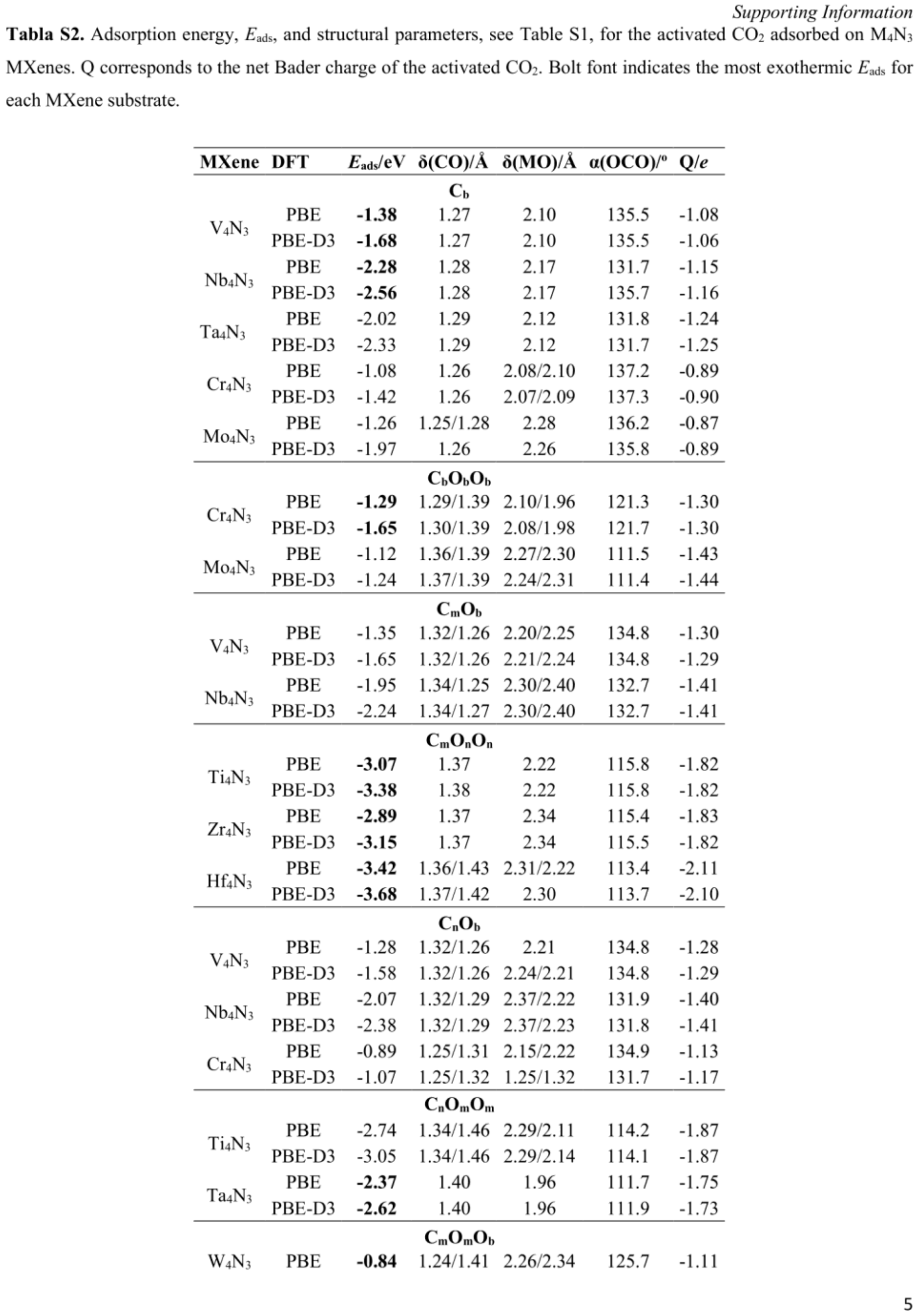

Tabla S2. Adsorption energy, E_{ads}, and structural parameters, see Table S1, for the activated CO_2 adsorbed on M_4N_3 MXenes. Q corresponds to the net Bader charge of the activated CO_2. Bolt font indicates the most exothermic E_{ads} for each MXene substrate.

MXene	DFT	E_{ads}/eV	δ(CO)/Å	δ(MO)/Å	α(OCO)/°	Q/*e*
			C_b			
V_4N_3	PBE	**-1.38**	1.27	2.10	135.5	-1.08
	PBE-D3	**-1.68**	1.27	2.10	135.5	-1.06
Nb_4N_3	PBE	**-2.28**	1.28	2.17	131.7	-1.15
	PBE-D3	**-2.56**	1.28	2.17	135.7	-1.16
Ta_4N_3	PBE	-2.02	1.29	2.12	131.8	-1.24
	PBE-D3	-2.33	1.29	2.12	131.7	-1.25
Cr_4N_3	PBE	-1.08	1.26	2.08/2.10	137.2	-0.89
	PBE-D3	-1.42	1.26	2.07/2.09	137.3	-0.90
Mo_4N_3	PBE	-1.26	1.25/1.28	2.28	136.2	-0.87
	PBE-D3	-1.97	1.26	2.26	135.8	-0.89
			$C_bO_bO_b$			
Cr_4N_3	PBE	**-1.29**	1.29/1.39	2.10/1.96	121.3	-1.30
	PBE-D3	**-1.65**	1.30/1.39	2.08/1.98	121.7	-1.30
Mo_4N_3	PBE	-1.12	1.36/1.39	2.27/2.30	111.5	-1.43
	PBE-D3	-1.24	1.37/1.39	2.24/2.31	111.4	-1.44
			C_mO_b			
V_4N_3	PBE	-1.35	1.32/1.26	2.20/2.25	134.8	-1.30
	PBE-D3	-1.65	1.32/1.26	2.21/2.24	134.8	-1.29
Nb_4N_3	PBE	-1.95	1.34/1.25	2.30/2.40	132.7	-1.41
	PBE-D3	-2.24	1.34/1.27	2.30/2.40	132.7	-1.41
			$C_mO_nO_n$			
Ti_4N_3	PBE	**-3.07**	1.37	2.22	115.8	-1.82
	PBE-D3	**-3.38**	1.38	2.22	115.8	-1.82
Zr_4N_3	PBE	**-2.89**	1.37	2.34	115.4	-1.83
	PBE-D3	**-3.15**	1.37	2.34	115.5	-1.82
Hf_4N_3	PBE	**-3.42**	1.36/1.43	2.31/2.22	113.4	-2.11
	PBE-D3	**-3.68**	1.37/1.42	2.30	113.7	-2.10
			C_nO_b			
V_4N_3	PBE	-1.28	1.32/1.26	2.21	134.8	-1.28
	PBE-D3	-1.58	1.32/1.26	2.24/2.21	134.8	-1.29
Nb_4N_3	PBE	-2.07	1.32/1.29	2.37/2.22	131.9	-1.40
	PBE-D3	-2.38	1.32/1.29	2.37/2.23	131.8	-1.41
Cr_4N_3	PBE	-0.89	1.25/1.31	2.15/2.22	134.9	-1.13
	PBE-D3	-1.07	1.25/1.32	1.25/1.32	131.7	-1.17
			$C_nO_mO_m$			
Ti_4N_3	PBE	-2.74	1.34/1.46	2.29/2.11	114.2	-1.87
	PBE-D3	-3.05	1.34/1.46	2.29/2.14	114.1	-1.87
Ta_4N_3	PBE	**-2.37**	1.40	1.96	111.7	-1.75
	PBE-D3	**-2.62**	1.40	1.96	111.9	-1.73
			$C_mO_mO_b$			
W_4N_3	PBE	**-0.84**	1.24/1.41	2.26/2.34	125.7	-1.11

PBE-D3	**-1.09**	1.22/1.5	2.29/2.35	124.9	-1.11

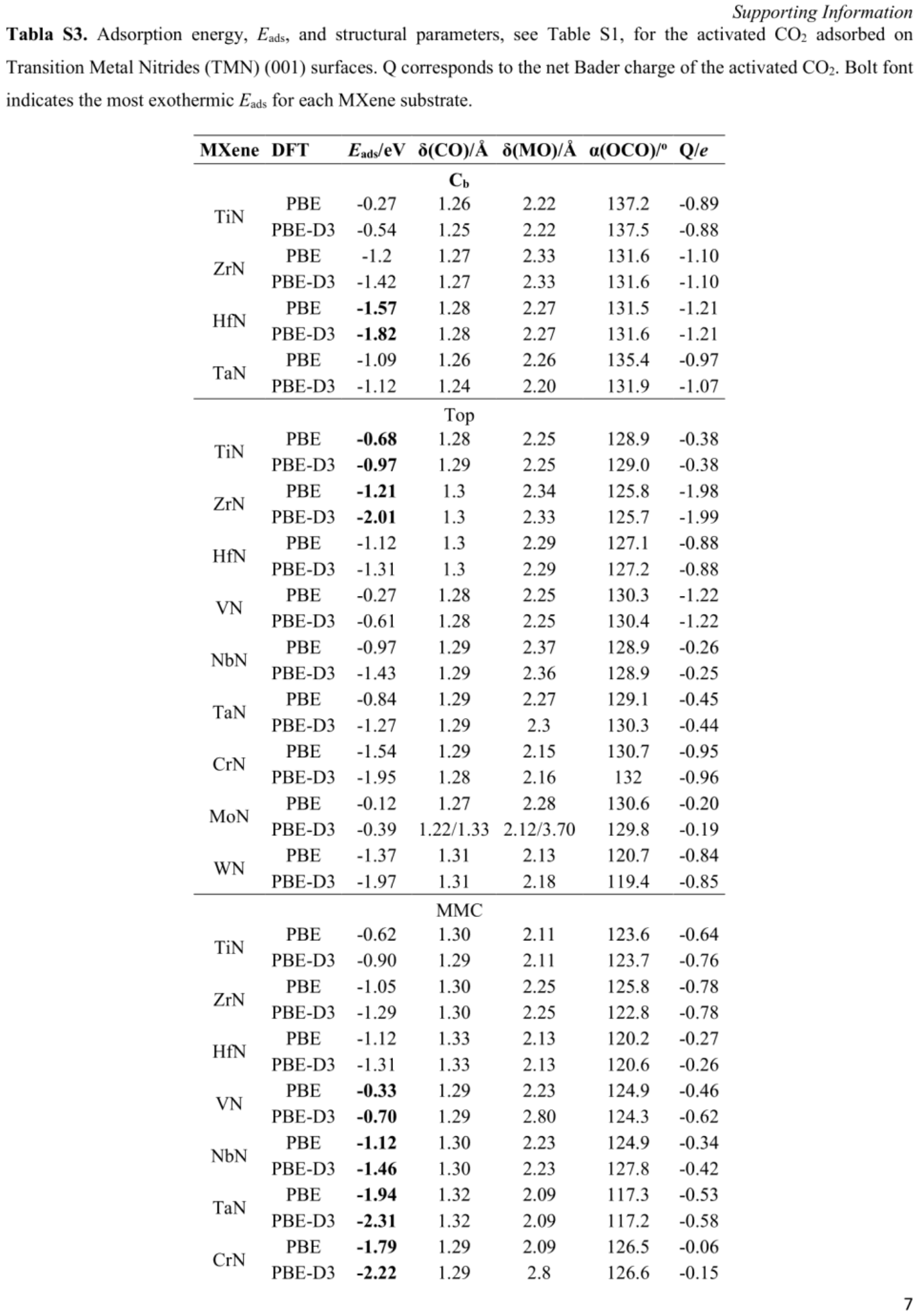

Tabla S3. Adsorption energy, E_{ads}, and structural parameters, see Table S1, for the activated CO_2 adsorbed on Transition Metal Nitrides (TMN) (001) surfaces. Q corresponds to the net Bader charge of the activated CO_2. Bolt font indicates the most exothermic E_{ads} for each MXene substrate.

MXene	DFT	E_{ads}/eV	δ(CO)/Å	δ(MO)/Å	α(OCO)/°	Q/*e*
			C$_b$			
TiN	PBE	-0.27	1.26	2.22	137.2	-0.89
	PBE-D3	-0.54	1.25	2.22	137.5	-0.88
ZrN	PBE	-1.2	1.27	2.33	131.6	-1.10
	PBE-D3	-1.42	1.27	2.33	131.6	-1.10
HfN	PBE	**-1.57**	1.28	2.27	131.5	-1.21
	PBE-D3	**-1.82**	1.28	2.27	131.6	-1.21
TaN	PBE	-1.09	1.26	2.26	135.4	-0.97
	PBE-D3	-1.12	1.24	2.20	131.9	-1.07
			Top			
TiN	PBE	**-0.68**	1.28	2.25	128.9	-0.38
	PBE-D3	**-0.97**	1.29	2.25	129.0	-0.38
ZrN	PBE	**-1.21**	1.3	2.34	125.8	-1.98
	PBE-D3	**-2.01**	1.3	2.33	125.7	-1.99
HfN	PBE	-1.12	1.3	2.29	127.1	-0.88
	PBE-D3	-1.31	1.3	2.29	127.2	-0.88
VN	PBE	-0.27	1.28	2.25	130.3	-1.22
	PBE-D3	-0.61	1.28	2.25	130.4	-1.22
NbN	PBE	-0.97	1.29	2.37	128.9	-0.26
	PBE-D3	-1.43	1.29	2.36	128.9	-0.25
TaN	PBE	-0.84	1.29	2.27	129.1	-0.45
	PBE-D3	-1.27	1.29	2.3	130.3	-0.44
CrN	PBE	-1.54	1.29	2.15	130.7	-0.95
	PBE-D3	-1.95	1.28	2.16	132	-0.96
MoN	PBE	-0.12	1.27	2.28	130.6	-0.20
	PBE-D3	-0.39	1.22/1.33	2.12/3.70	129.8	-0.19
WN	PBE	-1.37	1.31	2.13	120.7	-0.84
	PBE-D3	-1.97	1.31	2.18	119.4	-0.85
			MMC			
TiN	PBE	-0.62	1.30	2.11	123.6	-0.64
	PBE-D3	-0.90	1.29	2.11	123.7	-0.76
ZrN	PBE	-1.05	1.30	2.25	125.8	-0.78
	PBE-D3	-1.29	1.30	2.25	122.8	-0.78
HfN	PBE	-1.12	1.33	2.13	120.2	-0.27
	PBE-D3	-1.31	1.33	2.13	120.6	-0.26
VN	PBE	**-0.33**	1.29	2.23	124.9	-0.46
	PBE-D3	**-0.70**	1.29	2.80	124.3	-0.62
NbN	PBE	**-1.12**	1.30	2.23	124.9	-0.34
	PBE-D3	**-1.46**	1.30	2.23	127.8	-0.42
TaN	PBE	**-1.94**	1.32	2.09	117.3	-0.53
	PBE-D3	**-2.31**	1.32	2.09	117.2	-0.58
CrN	PBE	**-1.79**	1.29	2.09	126.5	-0.06
	PBE-D3	**-2.22**	1.29	2.8	126.6	-0.15

MoN	PBE	**-0.92**	1.32	2.13	120	-0.34
	PBE-D3	**-1.22**	1.32	2.13	119.9	-0.51
WN	PBE	**-1.38**	1.35	2.14	124.2	-0.66
	PBE-D3	**-1.98**	1.38	2.08	123.9	-0.73
			O_mO_m			
TiN	PBE	-0.01	1.29	2.05	121.3	-1.1
	PBE-D3	-0.35	1.28	2.06	122.9	-1.8
ZrN	PBE	-0.87	1.31	2.12	114.9	-1.29
	PBE-D3	-1.09	1.31	2.13	115.3	-1.3
HfN	PBE	-1.41	1.33	2.06	115.3	-1.4
	PBE-D3	-1.64	1.33	2.06	112.9	-1.4
TaN	PBE	-1.12	1.31	2.09	118.9	-1.17
	PBE-D3	-1.43	1.31	2.04	114.72	-1.17

Tabla S4. Adsorption energy, E_{ads}, and structural parameters, see Table S1, for the activated CO_2 adsorbed on TMN (111) surfaces. Q corresponds to the net Bader charge of the activated CO_2. Bolt font indicates the most exothermic E_{ads} for each MXene substrate.

MXene	Level	Eads/eV	δ(CO)/Å	δ(MO)/Å	α(OCO)/º	Q/e
C_b						
VN	PBE	-1.3	1.27	2.11	135.8	-1.04
	PBE-D3	-1.6	1.27	2.10	135.7	-1.04
NbN	PBE	**-1.86**	1.29	2.19	129.9	-1.16
	PBE-D3	**-2.14**	1.29	2.19	129.9	-1.17
TaN	PBE	-2.28	1.30	2.12	129.1	-1.37
	PBE-D3	-2.46	1.29	2.12	131.7	-1.37
CrN	PBE	-1.04	1.26	2.09/2.11	137.3	-0.87
	PBE-D3	-1.48	1.26	2.08/2.09	137.3	-0.88
MoN	PBE	**-3.27**	1.37	2.20	118.7	-1.49
	PBE-D3	**-3.44**	1.27	2.27	133.3	-0.89
$C_bO_bO_b$						
VN	PBE	-1.68	1.34	1.95	116.6	-1.39
	PBE-D3	-1.99	1.34	1.95	116.6	-1.4
TaN	PBE	-2.18	1.37/1.42	2.11/2.22	106.4	-1.72
	PBE-D3	-2.29	1.35/1.43	2.09/2.18	106.7	-1.66
CrN	PBE	-1.25	1.30/1.40	1.98/2.10/2.21	120.0	-1.33
	PBE-D3	-1.52	1.35	1.93	116.9	-1.29
C_mO_b						
VN	PBE	**-1.83**	1.35	1.95	115.1	-1.47
	PBE-D3	**-2.10**	1.35	1.95	115.1	-1.47
NbN	PBE	-1.47	1.35	2.05	116.5	-1.47
	PBE-D3	-2.06	1.34	2.06	116.5	-1.46
$C_mO_nO_n$						
TiN	PBE	**-3.35**	1.38	2.19/2.22	115.6	-1.83
	PBE-D3	**-3.67**	1.38	2.19/2.22	115.6	-1.84
ZrN	PBE	**-3.20**	1.38	2.34	115.2	-1.85
	PBE-D3	**-3.46**	1.38	2.34	115.1	-1.86
HfN	PBE	**-3.28**	1.39	2.29	113.9	-2.06
	PBE-D3	**-3.58**	1.40	2.29	113.9	-2.06
C_nO_b						
ZrN	PBE	-2.21	1.29/1.36	2.38	130.1	-1.63
	PBE-D3	-2.28	1.29/1.36	2.32/2.37	130.1	-1.6
HfN	PBE	-2.35	1.30/1.39	2.28/2.31	130.5	-1.83
	PBE-D3	-2.62	1.29/1.41	2.3	130.4	-1.85
VN	PBE	-1.2	1.26/1.32	2.19/2.28	134.6	-1.25
	PBE-D3	-1.5	1.26/1.32	2.19/2.24	134.7	-1.25
NbN	PBE	-1.71	1.28/1.33	2.27/2.40	131.5	-1.39
	PBE-D3	-1.97	1.30/1.33	2.26/2.39	129.3	-1.44
CrN	PBE	-0.88	1.26/1.31	2.19/2.23	134.9	-1.15
	PBE-D3	-1.04	1.28	2.0/2.13	125.1	-1.16
$C_nO_mO_m$						
TiN	PBE	-2.97	1.40	2.15/2.23	116.0	-1.85

	PBE-D3	-3.21	1.38	2.19/2.22	115.7	-1.83
ZrN	PBE	-2.64	1.33/1.42	2.29/2.41	115.9	-1.81
	PBE-D3	-2.89	1.33/1.42	2.29/2.40	115.9	-1.81
TaN	PBE	**-2.36**	1.40	1.96	111.8	-1.72
	PBE-D3	**-2.55**	1.40	1.97	111.9	-1.71
CrN	PBE	**-2.99**	1.33/1.36	1.85/1.97	119.4	-1.23
	PBE-D3	**-3.94**	1.33/1.37	2.06/2.17	120.9	-1.46
			$C_mO_mO_b$			
WN	PBE	**-0.25**	1.23/1.41	2.27/2.33	125.8	-1.00
	PBE-D3	**-0.39**	1.22/1.50	2.27/2.33	125.0	-1.11

Fig S1. Top and side views of the CO_2 adsorption sites on the studied TMN (001) surfaces as listed in Table S3.

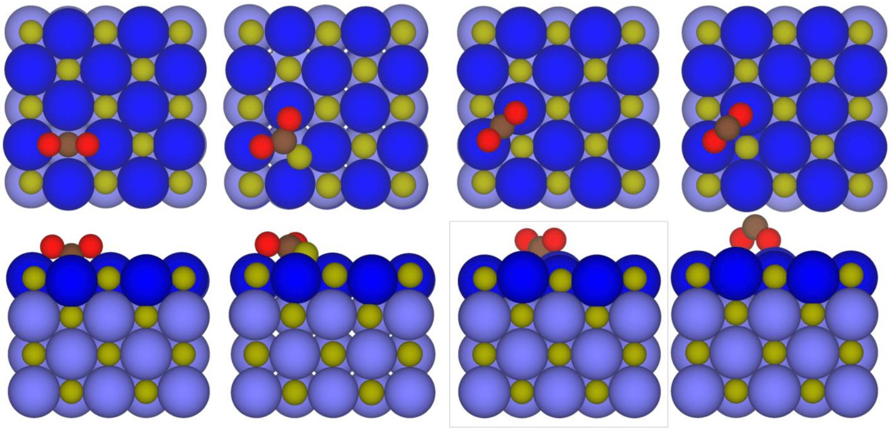

C_n $C_nO_mO_m$ C_b O_bO_b

Fig S2. Carbon Capture and Storage (CCS) kinetic phase diagrams of Ti-derived MXenes with stoichiometries Ti_2N, Ti_3N_2, and Ti_4N_3.

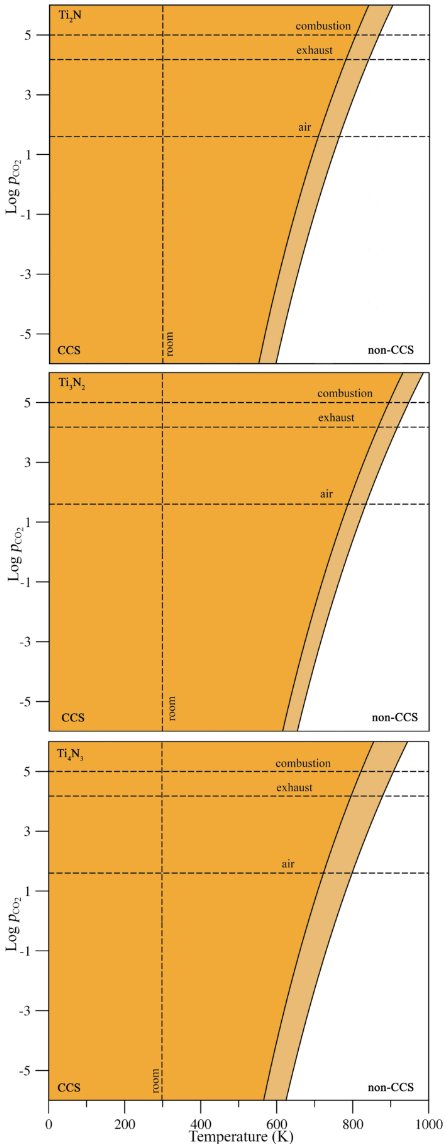

Fig S3. CCS kinetic phase diagrams of TiN (001) and (111) surfaces.

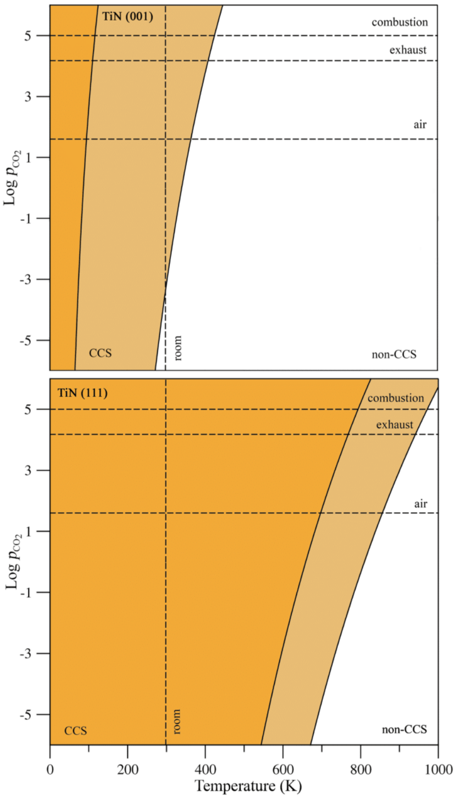

Fig S4. CCS kinetic phase diagrams of CCS) kinetic phase diagrams of Zr-derived MXenes with stoichiometries Zr_2N, Zr_3N_2, and Zr_4N_3.

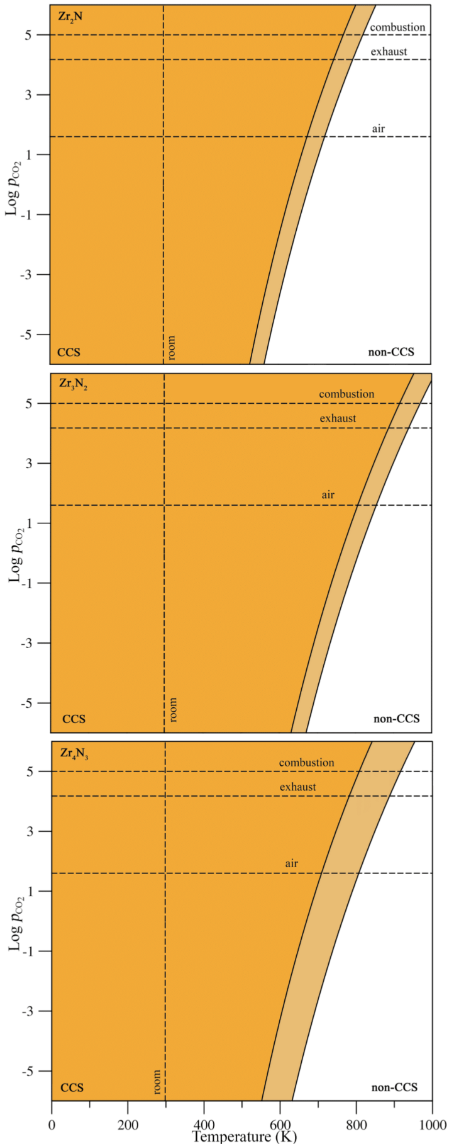

Fig S5. CCS kinetic phase diagrams of ZrN (001) and (111) surfaces.

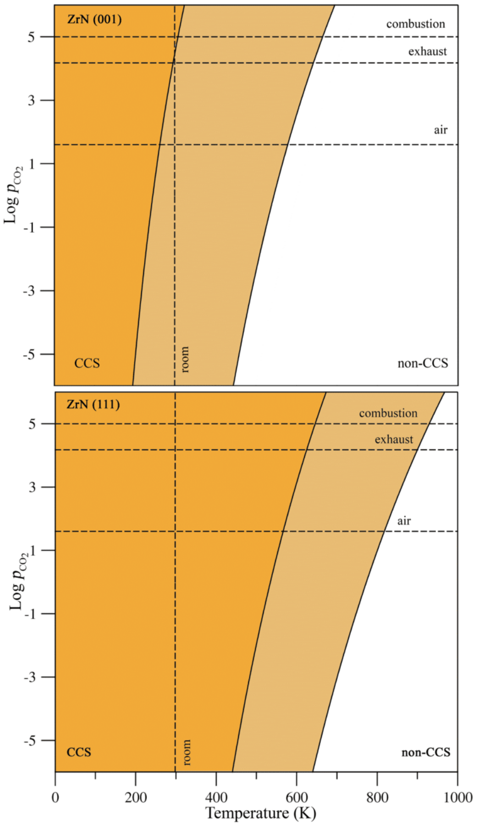

Fig S6. CCS kinetic phase diagrams of CCS) kinetic phase diagrams of Hf-derived MXenes with stoichiometries Hf_2N, Hf_3N_2, and Hf_4N_3.

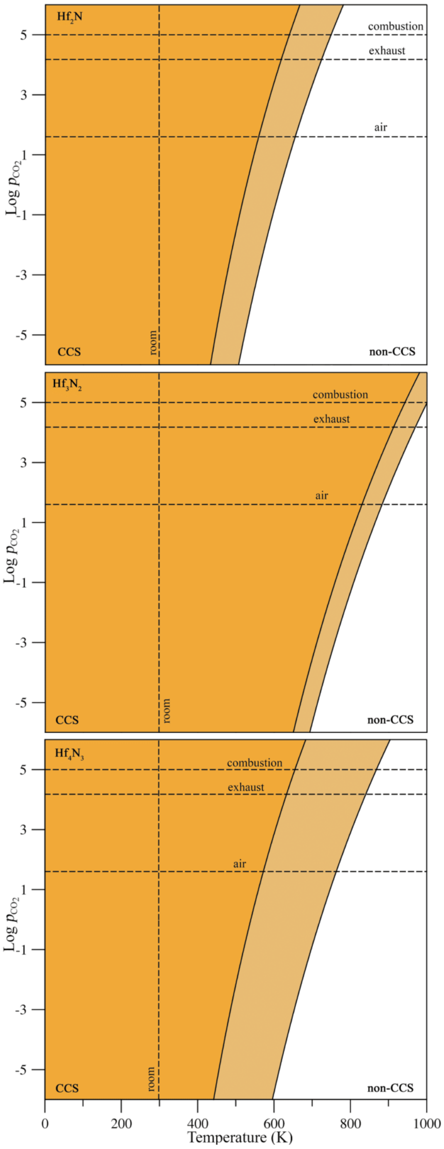

Fig S7. CCS kinetic phase diagrams of HfN (001) and (111) surfaces.

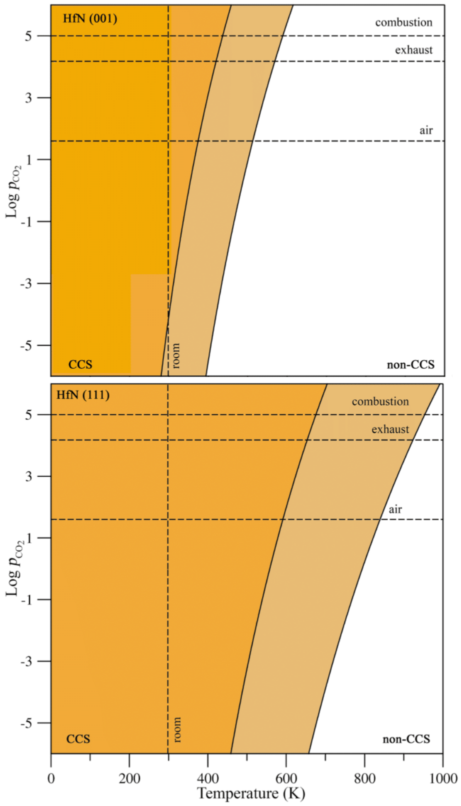

Fig S8. CCS kinetic phase diagrams of CCS) kinetic phase diagrams of V-derived MXenes with stoichiometries V_2N, V_3N_2, and V_4N_3.

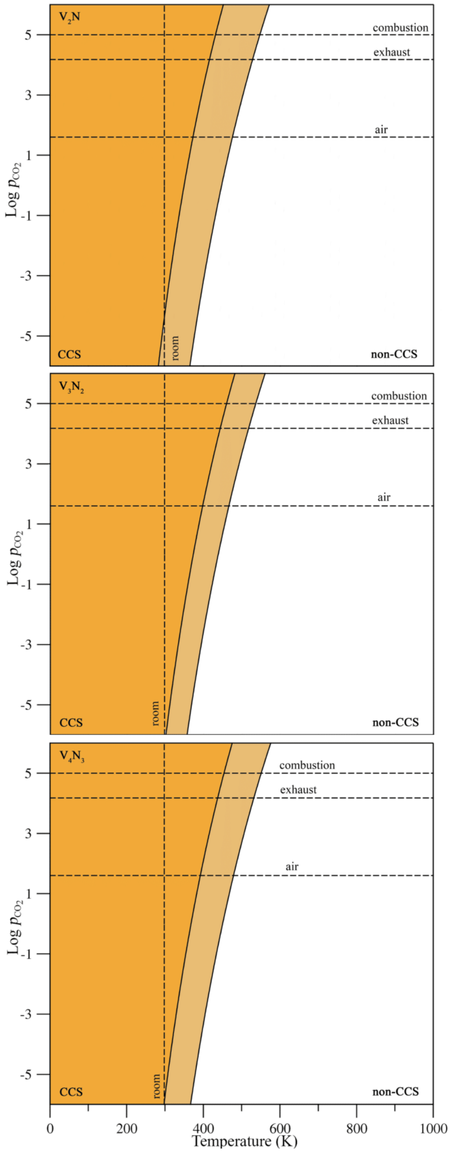

Fig S9. CCS kinetic phase diagrams of VN (001) and (111) surfaces.

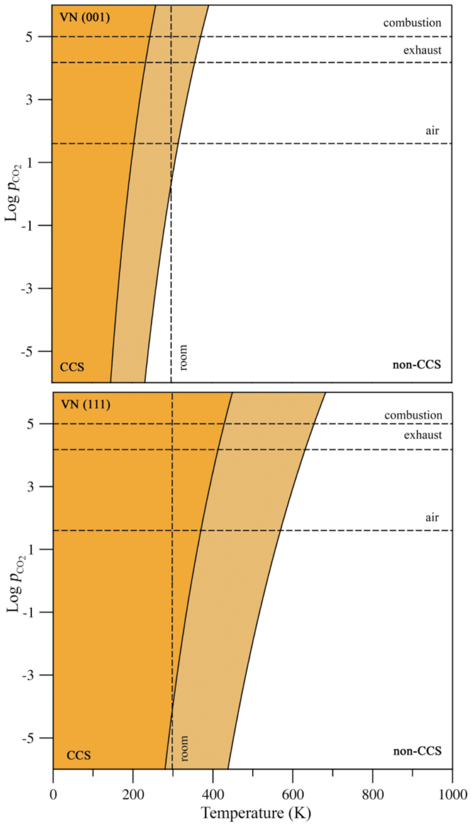

Fig S10. CCS kinetic phase diagrams of CCS) kinetic phase diagrams of Nb-derived MXenes with stoichiometries Nb_2N, Nb_3N_2, and Nb_4N_3.

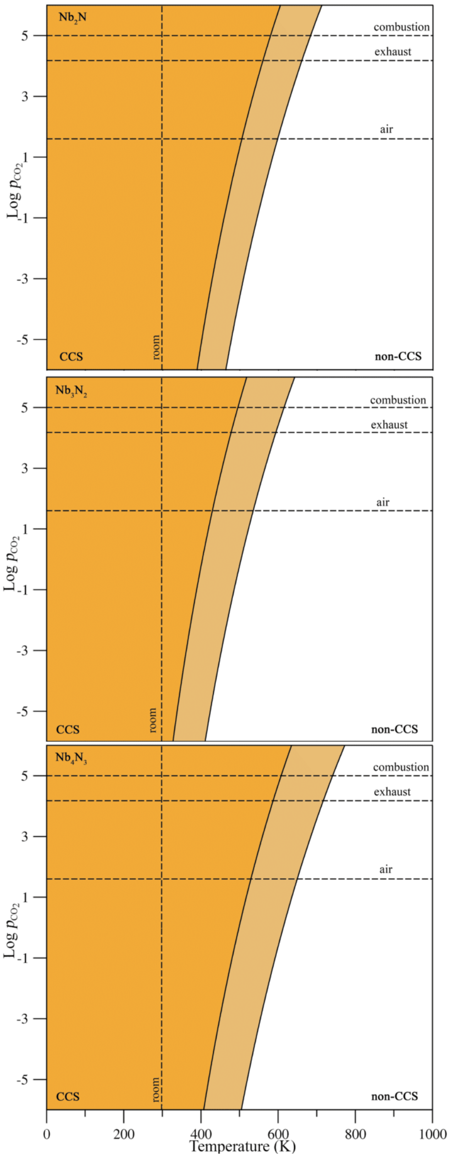

Fig S11. CCS kinetic phase diagrams of NbN (001) and (111) surfaces.

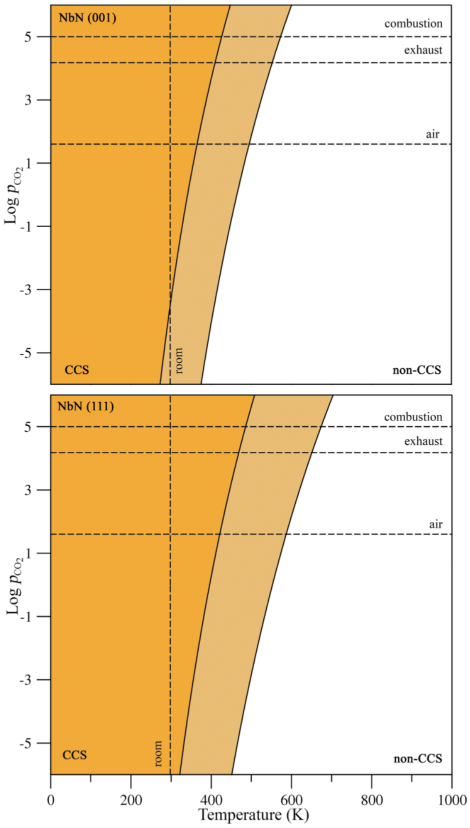

Fig S12. CCS kinetic phase diagrams of CCS) kinetic phase diagrams of Ta-derived MXenes with stoichiometries Ta_2N, Ta_3N_2, and Ta_4N_3.

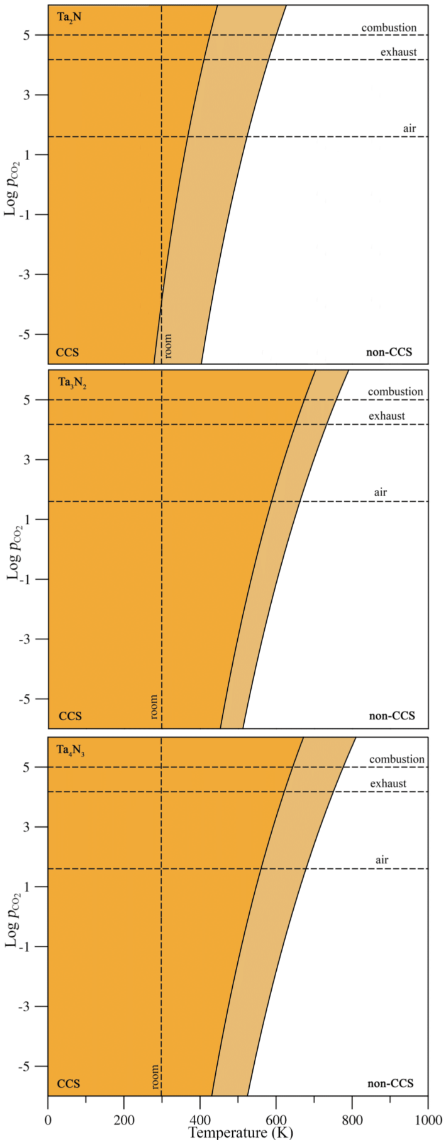

Fig S13. CCS kinetic phase diagrams of TaN (001) and (111) surfaces.

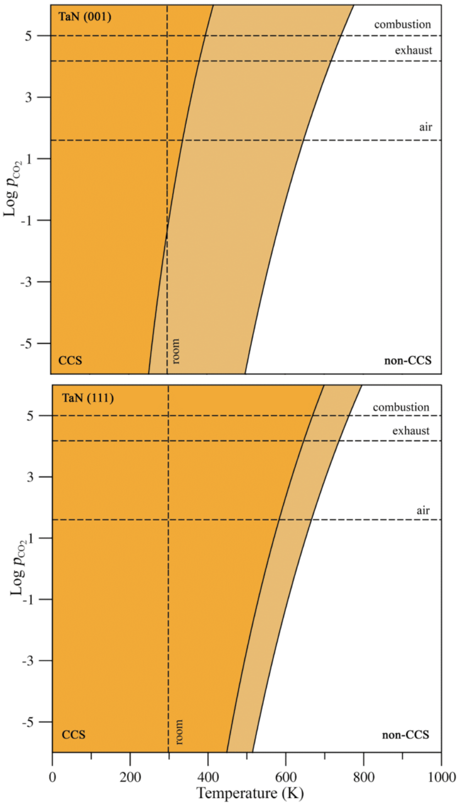

Fig S14. CCS kinetic phase diagrams of CCS) kinetic phase diagrams of Cr-derived MXenes with stoichiometries Cr_2N, Cr_3N_2, and Cr_4N_3.

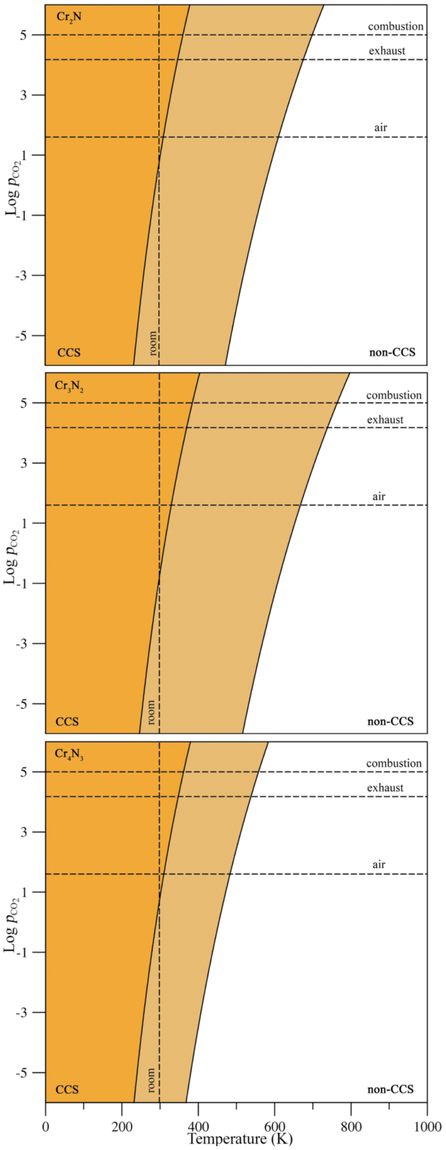

Fig S15. CCS kinetic phase diagrams of CrN (001) and (111) surfaces.

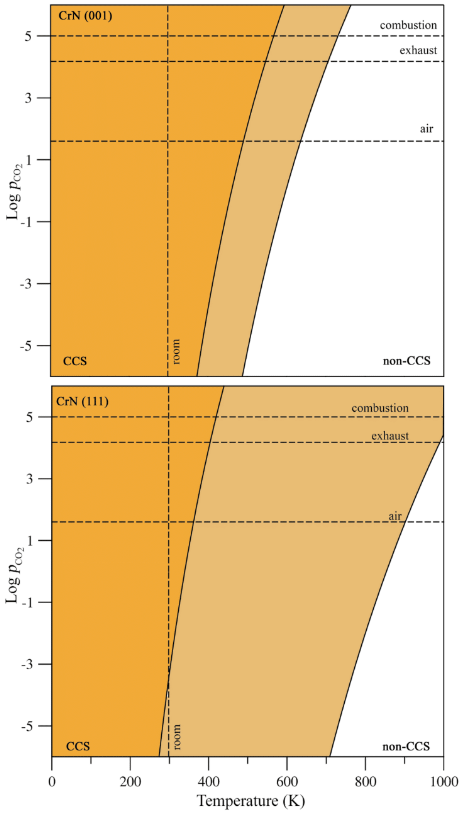

Fig S16. CCS kinetic phase diagrams of CCS) kinetic phase diagrams of Mo-derived MXenes with stoichiometries Mo_2N, Mo_3N_2, and Mo_4N_3.

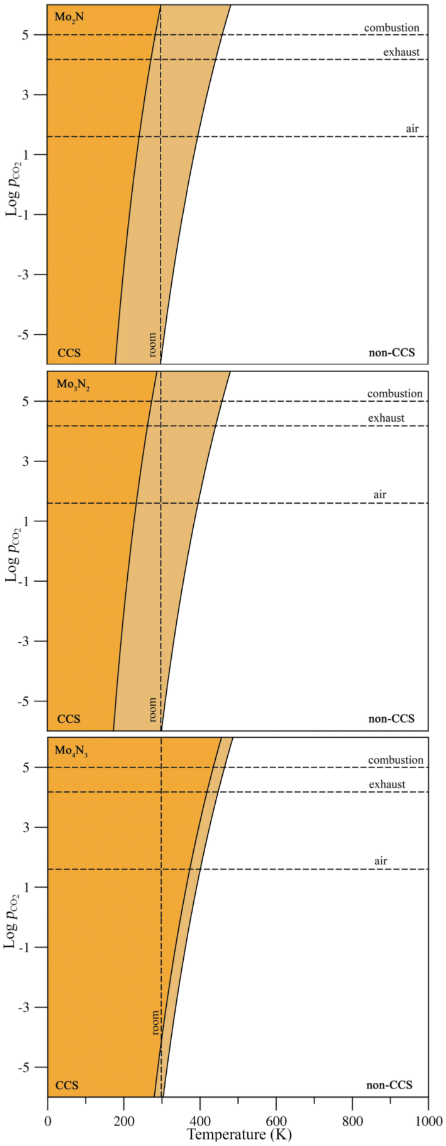

Fig S17. CCS kinetic phase diagrams of MoN (001) and (111) surfaces.

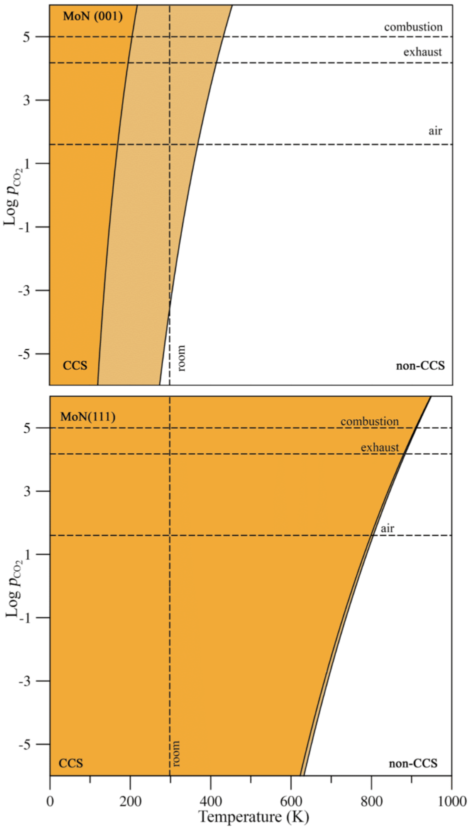

Fig S18. CCS kinetic phase diagrams of CCS) kinetic phase diagrams of W-derived MXenes with stoichiometries W_2N, W_3N_2, and W_4N_3.

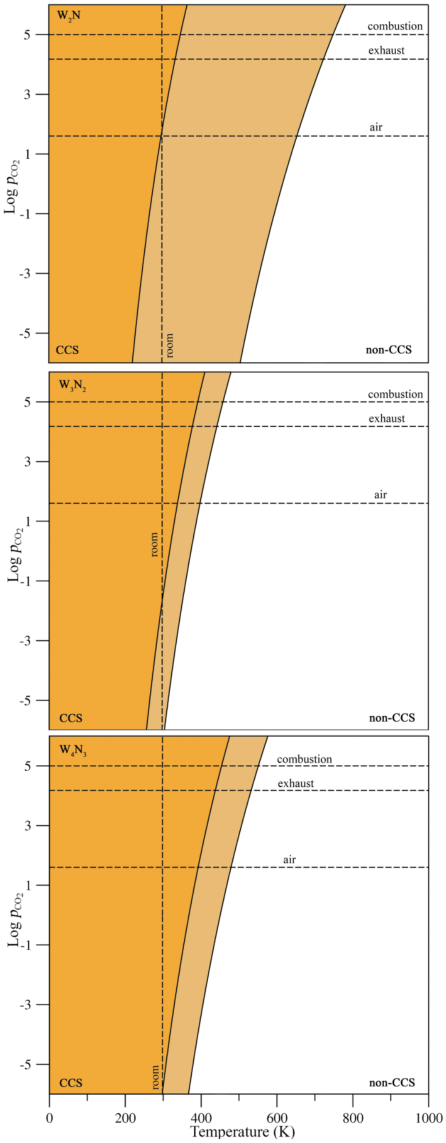

Fig S19. CCS kinetic phase diagrams of WN (001) and (111) surfaces.

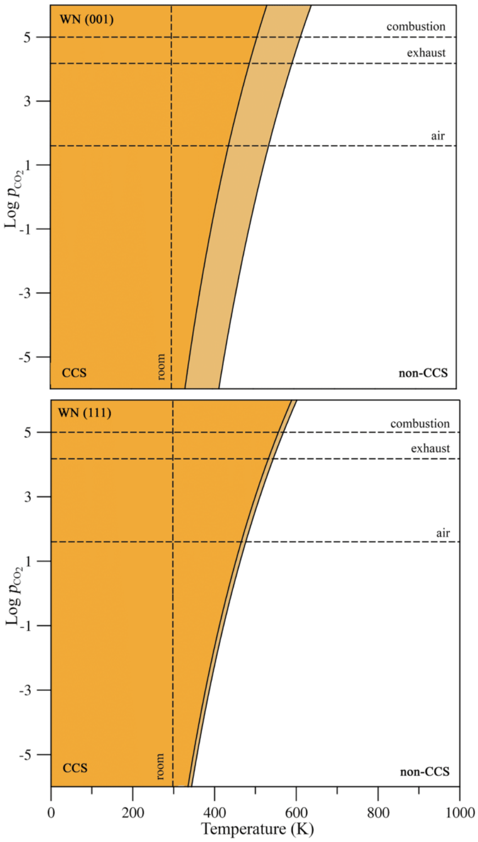

Appendix B

Supporting Information for

“Molecular Mechanism and Microkinetic Analysis of the Reverse Water Gas Shift Reaction Heterogeneously Catalyzed by the Mo_2C MXene”

Supporting Information

Molecular Mechanisms and Multiscale Analysis of the Reverse Water Gas Shift Reaction Heterogeneously Catalyzed by the Mo_2C MXene

Anabel Jurado, Ángel Morales-García,* Francesc Viñes, and Francesc Illas*

Departament de Ciència de Materials i Química Física & Institut de Química Teòrica i
Computacional (IQTCUB), Universitat de Barcelona,
c/ Martí i Franquès 1-11, 08028 Barcelona, Spain

e-mails: angel.morales@ub.edu; francesc.illas@ub.edu

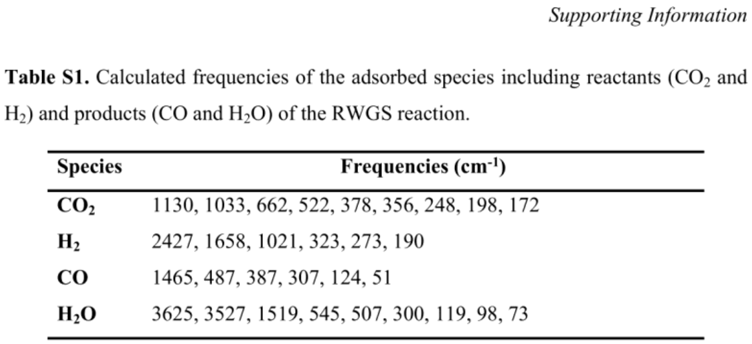

Supporting Information

Table S1. Calculated frequencies of the adsorbed species including reactants (CO_2 and H_2) and products (CO and H_2O) of the RWGS reaction.

Species	**Frequencies (cm^{-1})**
CO_2	1130, 1033, 662, 522, 378, 356, 248, 198, 172
H_2	2427, 1658, 1021, 323, 273, 190
CO	1465, 487, 387, 307, 124, 51
H_2O	3625, 3527, 1519, 545, 507, 300, 119, 98, 73

Figure S1. Total energy profile, Δ*E*, along the reaction path for the RWGS reaction over the (0001) Mo_2C MXene surface. Redox, COOH, and HCOO routes are depicted with black, red ,and green colours, respectively. The formation of HCOOH (blue route) is also included.

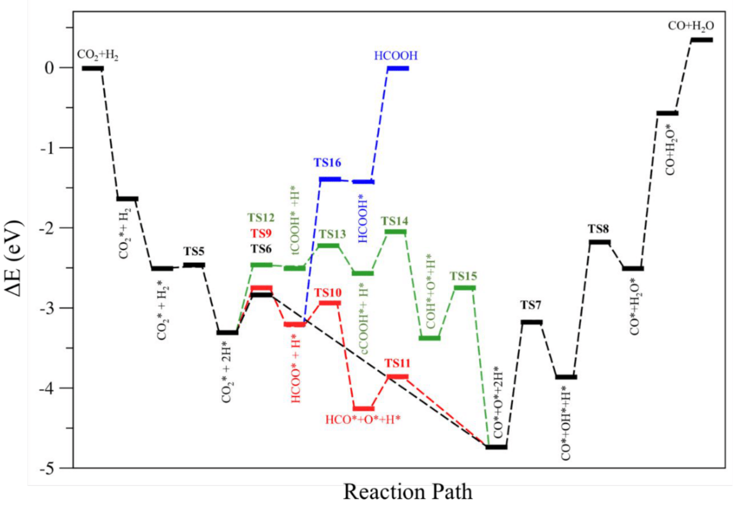

Figure S2. Transition states (TSs) of each elementary reaction investigated, see Table 1 of main text. Each TS is defined as a TS plus a digit (*e.g.*, TS6) easily to localize in the energy and Gibbs free energy profiles depicted in Table S1 and Table 4 of the main text, respectively.

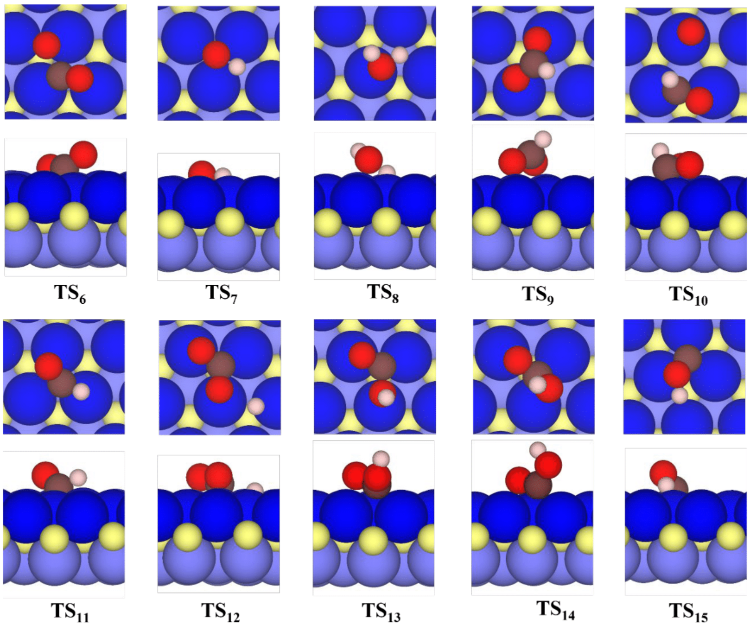

S1. Microkinetic Simulations

Microkinetic simulations on the (0001) Mo_2C MXene surface are carried out on a multi-step model concerning 15 elementary step —for details, see Table 1 of the main text—. This encompasses three different routes available for the RWGS: redox, COOH and HCOO. For every elementary step, two kinetic constants are required: forward and backward. For surface reactions, constants were estimated via transition state theory (TST),[1,2] following the equation;

$$k = \frac{k_B T}{h}\frac{Q^{TS}}{Q} e^{-\frac{E_a}{k_B T}} \qquad \text{(S1)},$$

where Q and Q^{TS} correspond to the partition functions of the initial state and TS, respectively. The former includes the vibrational modes including the translational and rotational modes of the gas phase molecule that become frustrated upon adsorption, and converted, *de facto*, into vibrations. The Q^{TS} includes also the vibrational modes with the exception of the imaginary mode characteristic of each TS. Finally, k_B is the Boltzmann constant, h the Planck constant, and E_a the activation energy.

The simulation involves the time-integration of the ordinary differential equations describing the kinetics of the system. We evaluate the reaction between 300 to 800 K in steps of 10 K. The simulation time for each of the simulations is set to 100 s. This simulation time is enough to reach the steady-state in each temperature.

The heating maps —see later Figure S3, and Figure 6 of the main text— are built performing simultaneous microkinetic simulations at different total pressures in the range of 1–10 bar with a step of 0.5 bar. These simulations are carried out at three CO_2:H_2 ratio: 1:2, 1:1, and 2:1. One can easily access to the conditions of pressure, temperature, and turnover frequency (TOF) at which the RWGS reaction runs. Precisely, these three variables are employed to plot the colormap using a (x, y, z) data grid.

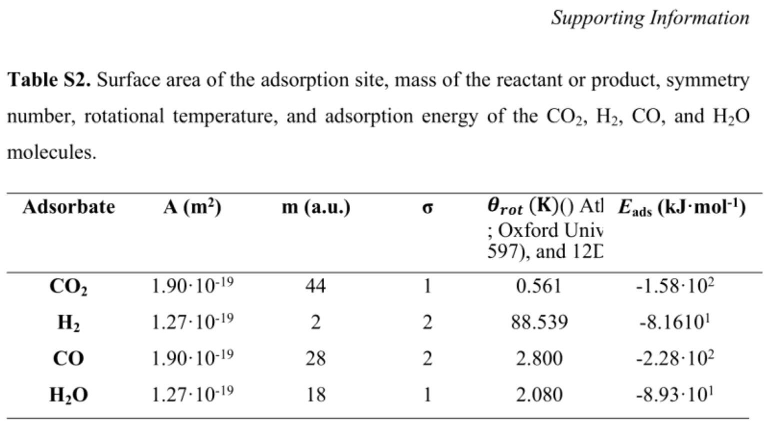

Supporting Information

Table S2. Surface area of the adsorption site, mass of the reactant or product, symmetry number, rotational temperature, and adsorption energy of the CO_2, H_2, CO, and H_2O molecules.

Adsorbate	A (m^2)	m (a.u.)	σ	$\boldsymbol{\theta_{rot}}$ (K)() Atl ; Oxford Univ 597), and 12D	E_{ads} (kJ·mol^{-1})
CO_2	$1.90 \cdot 10^{-19}$	44	1	0.561	$-1.58 \cdot 10^{2}$
H_2	$1.27 \cdot 10^{-19}$	2	2	88.539	-8.1610^{1}
CO	$1.90 \cdot 10^{-19}$	28	2	2.800	$-2.28 \cdot 10^{2}$
H_2O	$1.27 \cdot 10^{-19}$	18	1	2.080	$-8.93 \cdot 10^{1}$

Supporting Information

Figure S3. Heating map of TOF *vs.* the *p*/*T* working conditions space of the RWGS reaction on the (0001) Mo_2C MXene surface for H_2O production. Units for *p*, *T*, and TOF are bar, K, and molecules·site^{-1}·s^{-1}, respectively. The TOF scale corresponds to the common logarithm with base 10.

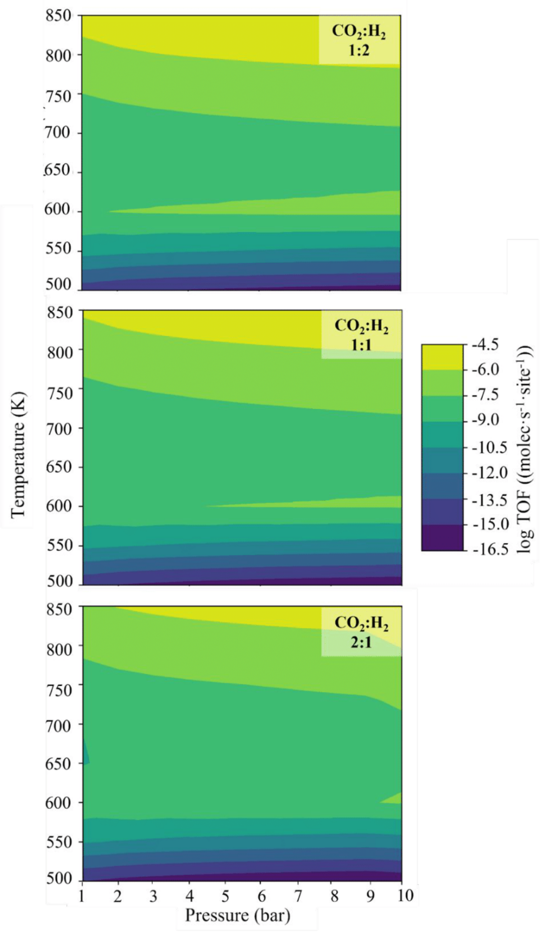

---

(1) Laldler, K. J.; King, M. C. The Development of Transition-State Theory. *J. Phys. Chem.* **1983**, *87*, 2657-2664.

(2) Truhlar, D. G.; Garrett, B. C.; Klippenstein, S. J. Current Status of Transition-State Theory. *J. Phys. Chem.* **1996**, *100*, 12771-12800.